120
8-26-81

①

Hr. 2976

LA-8891-T

Thesis

B6719

MASTER

The Positive-Pion Double-Charge-Exchange Reaction:

Experiments on the Isotopic Pairs Oxygen-16,18 and Magnesium-24,26

University of California

DISTRIBUTION OF THIS DOCUMENT IS UNLIMITED

LOS ALAMOS SCIENTIFIC LABORATORY
Post Office Box 1663 Los Alamos, New Mexico 87545

TABLE OF CONTENTS

LIST OF FIGURES

Figure Page

Figure Page

LIST OF TABLES

Table | Page

THE POSITIVE-PION DOUBLE-CHARGE-EXCHANGE REACTION: EXPERIMENTS ON THE ISOTOPIC PAIRS OXYGEN-16,18 AND MAGNESIUM-24,26

by

Steven Joseph Greene, Ph.D.
The University of Texas at Austin, 1981

Supervising Professor: C. Fred Moore

ABSTRACT

The (π^+,π^-) double-charge-exchange (DCX) reaction has been performed on targets of T=0,1 isospin (and isotopic) pairs $^{16,18}O$ and $^{24,26}Mg$. Energy excitation functions of $d\sigma/d\Omega$, across the (3,3) π-N resonance, are presented for transitions to double-isobaric analog state (DIAS) and non-DIAS ground-state residual nuclei. Angular distributions in the region of 5°-33° are presented for the DIAS from the T=1 nuclei. The similarities and differences of DIAS and non-DIAS distributions are discussed in relation to reaction-mechanism and nuclear-structure effects. Also, a simple, two-amplitude model for the ^{18}O excitation function, consistent with the data, is presented. The utility of DCX in nuclear mass measurements is discussed, with some examples.

I. INTRODUCTION

The pi meson is the lightest of the family of hadrons, those particles which interact via the strong nuclear force. Their existence was first postulated in a field-theoretic treatment of the strong force by Yukawa [Yu-35]. In that description, the force is mediated by the exchange of particles, named mesons, between the various nucleons of a nucleus. The lightest mass, and therefore longest range, component of these is the pi meson (pion or π). Much is known about the pion's physical properties, some of which are listed in Table 1-1. An important point to note is that pions are bosons ($J=0$) and have total isospin $T=1$. Having $J=0$ implies that there is no spin-spin coupling term in the force description when scattering pions from objects possessing spin. Total isospin $T=1$ means (in analogy with the quantum-mechanical spin) that there are three possible projections of the isospin vector, $T_z=\pm1,0$. These projections correspond to the three pion charge states π^+, π^-, π^0.

Though pions are unstable, they are relatively long-lived and may be used as scattering probes in the investigation of nuclei. The scattering of various particle probes (electrons, protons, ions, etc.) from nuclei is the principal experimental research technique of nuclear and particle physics. Pion beams can be formed and directed onto target nuclei, the scattering from which tells us about the

TABLE 1-1. Some physical properties of the π mesons.

Particle	T	T_z	J^π	Mass (MeV)	Mean Life (sec)	Decay	(%)
$\pi^\pm$	1	±1	0^-	139.57	2.6×10^{-8}	$\mu^\pm\nu$	~100
						$e^\pm\nu$	$\sim1.3\times10^{-2}$
						$\mu^\pm\nu\gamma$	$\sim1.2\times10^{-2}$
						$e^\pm\nu\gamma$	$\sim2.2\times10^{-6}$
						$e^\pm\nu\pi^0$	$\sim1.0\times10^{-6}$
π^0	1	0	0^-	134.96	8.3×10^{-17}	$\gamma\gamma$	~98.8
						γe^+e^-	~1.2
						$\gamma\gamma\gamma\gamma$	$<6\times10^{-3}$
						$e^+e^-e^+e^-$	$\sim3.3\times10^{-3}$
						$\gamma\gamma\gamma$	$<5\times10^{-4}$

structure and forces inside the nucleus. This, though, presupposes that the manner in which pions interact with the nucleus is known.

A nucleus is composed of nucleons (neutrons and protons). The interaction of pions with nucleons is thought to be fairly well understood [Ei-80]. Using the concept of charge independence of the strong nuclear force, it has been shown [Ke-38] that the interaction of a pion with a nucleon, in a state of definite total angular momentum and parity (J^π), depends only on the total isospin configuration of the π-N system. The isospin configurations $|T,T_z\rangle$ of the possible π-N systems are:

$$|p,\pi^+\rangle = |3/2,3/2\rangle$$

$$|p,\pi^0\rangle = \sqrt{2/3}\ |3/2,1/2\rangle - \sqrt{1/3}\ |1/2,1/2\rangle$$

$$|p,\pi^-\rangle = \sqrt{1/3}\ |3/2,-1/2\rangle - \sqrt{2/3}\ |1/2,-1/2\rangle$$

$$|n,\pi^+\rangle = \sqrt{1/3}\ |3/2,1/2\rangle + \sqrt{2/3}\ |1/2,1/2\rangle$$

$$|n,\pi^0\rangle = \sqrt{2/3}\ |3/2,-1/2\rangle + \sqrt{1/3}\ |1/2,-1/2\rangle$$

$$|n,\pi^-\rangle = |3/2,-3/2\rangle\ .$$

The scattering of pions from nucleons may then be described by a scattering matrix in isospin space. In particular, it can be shown that for π-N systems with $J=3/2$, the ratio of scattering cross sections is

$$\frac{\sigma(\pi^+ + p)}{\sigma(\pi^+ + n)} = \frac{\sigma(\pi^- + n)}{\sigma(\pi^- + p)} = \frac{9}{1} \qquad 1\text{-}1$$

The configuration here is (J=3/2,T=3/2); it is a resonance in the J=3/2, ℓ=1 partial wave and is commonly known as the (3,3) π-N resonance. This result indicates that a $\pi^+(\pi^-)$ will preferentially interact with a proton(neutron) at this resonance. The peak of the resonance corresponds to an incident pion kinetic energy of T_π=180 MeV. Figure 1-1 details this behavior for pions interacting with protons.

Nuclei might be thought of as a collection of nucleons bound together in a potential well. Pion scattering from a nucleus becomes much more complicated than from a free nucleon — it is not simply a series of free π-N interactions. The potential field of the nucleus acts to modify (distort) the parameters of the projectile as well as its subsequent interactions with the nucleons.

A useful way of modelling the scattering of pions from nuclei is in terms of an optical potential [Si-75]; the projectile is a complex wave which is propagated through a nuclear medium having some complex refractive index, described in certain quantum properties of the interacting particles. This is a method for understanding the complicated many-body scattering problem in terms of a one-body potential; it is a way of relating experimental data to theoretical calculation.

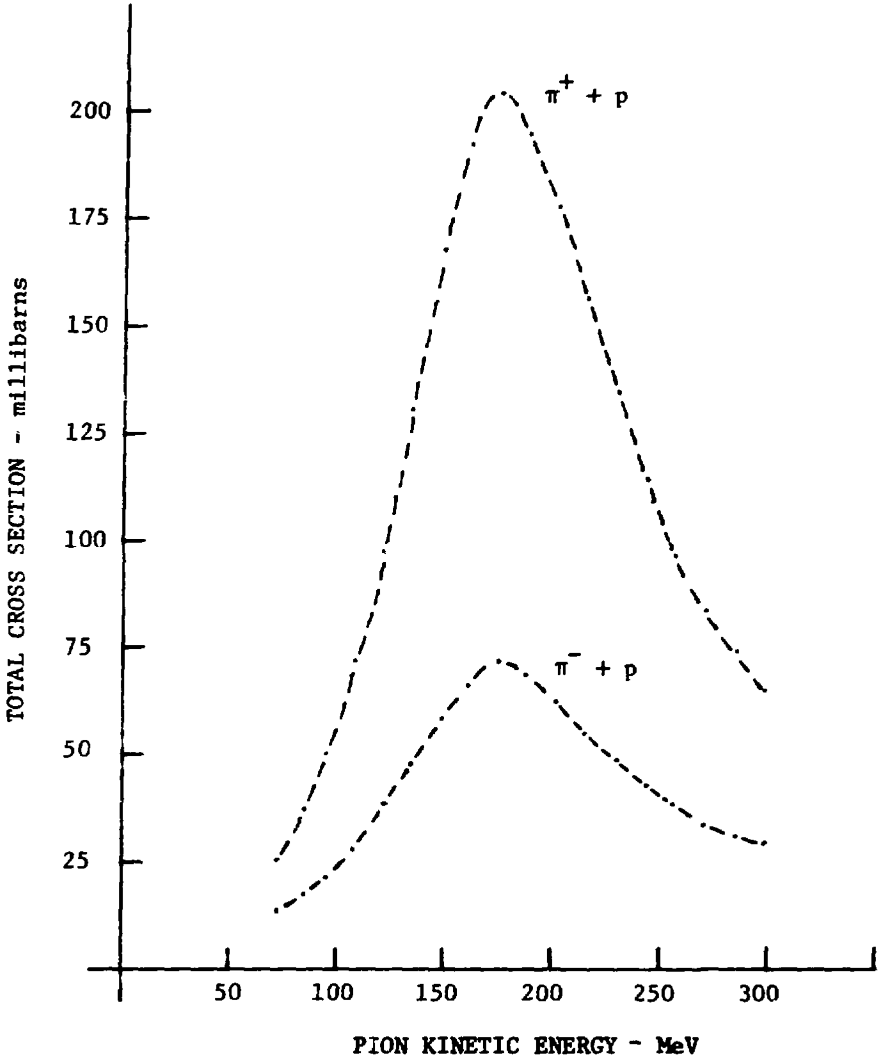

FIGURE 1-1. The $\pi^{\pm} + p$ total cross sections as a function of incident pion energy.

The scattering matrix amplitude (S) is related to the transition matrix amplitude (T) by the equation

$$S_{fi} = \delta_{fi} - 2\pi i\delta(E_f - E_i)\langle f|T|i\rangle, \qquad 1\text{-}2$$

where i and f represent the quantum numbers of the initial and final nuclear states. A form of the π-N t matrix [Ko-69], explicit in the spin and isospin dependence, is

$$t_{\pi N} = (b_0 + b_1\vec{t}_\pi \cdot \vec{T}_N) + (c_0 + c_1\vec{t}_\pi \cdot \vec{T}_N)\vec{\sigma}_N \cdot (\vec{k} \times \vec{k}'), \qquad 1\text{-}3$$

where $\vec{t}_\pi$ and $\vec{T}_N$ are pion and nucleon isospin operators, $\vec{k}$ and $\vec{k}'$ are pion initial and final momenta, $\vec{\sigma}_N$ is the nucleon spin operator, and (b_0, b_1, c_0, c_1) are energy-dependent parameters for the isospin dependent π-N phase shifts. The t matrix is constrained to obey the relation:

$$T = V + VGT, \qquad 1\text{-}4$$

where V is the optical potential and G is the propagator (Green's function) associated with the projectile.

For π-nucleus scattering the t matrix must be extrapolated off-shell. This is needed to describe cases in the intermediate scattering states of the pion in the nucleus in which the energy and momentum are no longer related. An example of this could be a π plus a nucleon forming a Δ-resonance within the nucleus; the Δ then propagates through the nucleus, decaying back to the final-state pion plus a nucleon still within the nucleus. The exact nature of these off-shell processes is unknown, so various approximations to them are made. The resulting calculations are very sensitive to the form of the off-shell extrapolation.

These considerations, and others, lead to various formulations of the optical potential. Miller and Spencer [Mi-76] obtain a potential in terms of the Kisslinger model [Ki-55]:

$$\begin{aligned} 2\omega V_{\alpha\beta}(r) = {} & \delta_{\alpha\beta}(N+Z)(2\pi)^3[(k/k_c)A\rho_o(r)-(k_c/k)C\vec{\nabla}\rho_o(\vec{r})\vec{\nabla}] \\ & + (2\pi)^3(\alpha|\vec{t}_\pi\cdot\vec{T}_N|\beta)[(k/k_c)B\rho_1(r)-(k_c/k)D\vec{\nabla}\rho_1(\vec{r})\vec{\nabla}]. \end{aligned} \qquad 1\text{-}5$$

N and Z are neutron and proton numbers, k and k_c are intermediate and initial pion momenta, $\vec{T}_N$ is the nucleus isospin operator, $\rho_o(r)$ is the nuclear density, and $\rho_1(r)$ is the difference between neutron and proton density distributions inside the nucleus. The subscripts α,β refer to elastic and charge-exchange reaction channels. This is a first-order optical potential — it is linear in the density terms.

Multiple-scattering theory develops the π-nucleus t matrix as a series, summed over individual nucleons:

$$T = \sum_i t_i + \sum_{i\neq j} t_i g t_j + \cdots. \qquad 1\text{-}6$$

This leads to the development of a second-order optical potential having terms proportional to $\rho^2(r)$. A second-order potential, along the lines developed for Eq. 1-5 [Mi-76] is:

$$\begin{aligned} V_{\alpha\beta}(\vec{k},\vec{k}') = \int d\vec{k}'' \{ & (N+Z)^2 t_0(\vec{k},\vec{k}'') t_0(\vec{k}'',\vec{k}') \\ & + (\alpha|(\vec{t}_\pi \cdot \vec{T}_N)^2|\beta) t_1(\vec{k},\vec{k}'') t_1(\vec{k}'',\vec{k}') + (\alpha|\vec{t}_\pi \cdot \vec{T}_N|\beta) \\ & \times (t_0(\vec{k},\vec{k}'') t_1(\vec{k}'',\vec{k}') + t_1(\vec{k},\vec{k}'') t_0(\vec{k}'',\vec{k}'))\} \\ & \times C(\vec{q}_1,\vec{q}_2) \langle k''|(E-\bar{\varepsilon}-k-\bar{V})^{-1}|k''\rangle. \end{aligned} \qquad 1\text{-}7$$

The momenta k, k′, and k″ are initial, final, and intermediate pion momenta, $q_1 = k''-k'$ and $q_2 = k'-k''$. The denominator is the off-shell propagator.

The general pion scattering reactions we try to model using such optical potentials are:

1) $(\pi^\pm,\pi^\pm)$ elastic scattering,

2) $(\pi^\pm,\pi^{\pm\prime})$ inelastic scattering,

3) $(\pi^\pm,\pi^0)$ single charge exchange,

and

4) $(\pi^\pm,\pi^\mp)$ double charge exchange,

In the t matrix form of Eq. 1-3, the (b_0,b_1,c_0,c_1) parameters all contribute to the elastic scattering reaction. Only parameters b_1 and c_1 contribute to charge exchange. The complete t matrix series of Eq. 1-6 is useful in the description of the processes of reactions

1 to 3. The pion double-charge-exchange (DCX) reaction, however, has as its first-order term of the reaction the second term on the right of Eq. 1-6.

Pion double charge exchange, in terms of the multiple-scattering series, seems to lead naturally to a second-order description of the optical potential. With such a potential description, it may then be possible to probe for correlations between nucleons in a nucleus. Fitting charge-exchange data with a second-order potential could determine the strengths of the various ρ^2 coefficients. Theoretical efforts to explain the observed strengths might show the need to invoke two-nucleon correlations, of a new form, in the picture of nuclear structure.

The above depends on being able to separate reaction-mechanism effects in the data from those caused by the structure of the target nuclei. The DCX reaction mechanism might be described, for instance, as one or a combination of two processes: two sequential single charge exchanges with the propagation of some intermediate particle between the two, or some type of π-NN interaction with two nucleons simultaneously. The first process might be less affected by certain aspects of nuclear structure (such as level structure) than the second.

Consider the total isospin T=0,1 isotopic pair $^{16,18}O$. The single-particle shell-model description of these nuclei is shown in Figure 1-2. The ^{16}O nucleus has N=Z; and the ^{18}O nucleus, which has N=Z+2, resembles ^{16}O plus two valence neutrons. In ^{16}O the

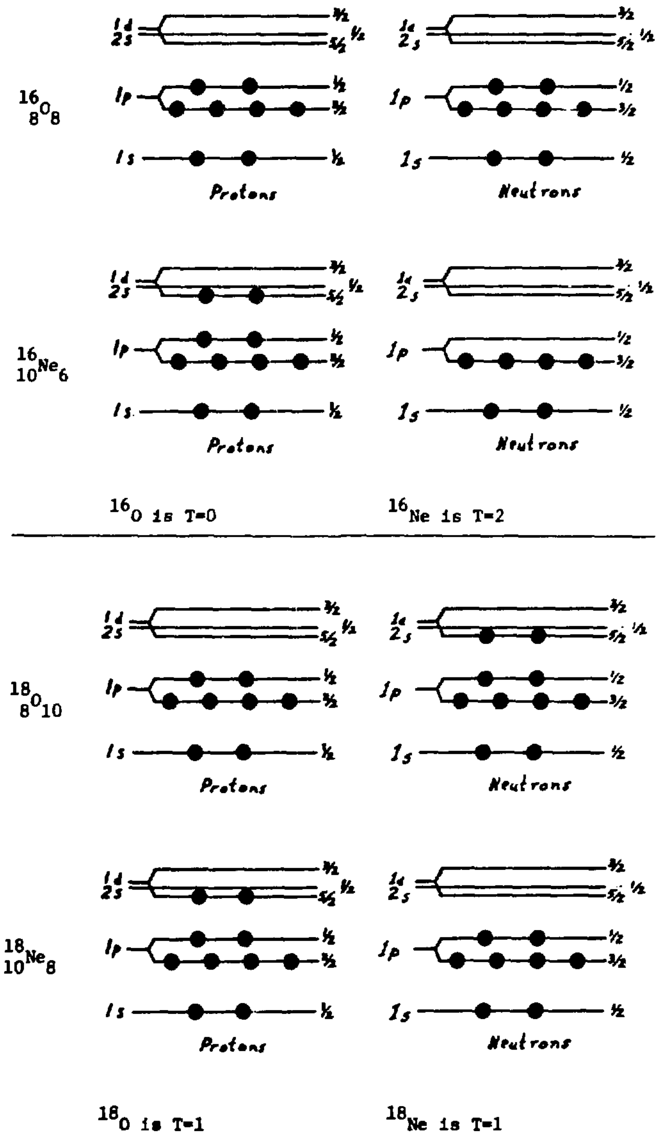

FIGURE 1-2. Simple single-particle shell model of the ^{16}O, ^{16}Ne and ^{18}O, ^{18}Ne nuclear ground states.

neutron-proton levels are 1p shells, filled with both protons and neutrons, resulting in a doubly magic nucleus, while in ^{18}O the two valence neutrons in the $1d_{5/2}$ level are opposite a vacant proton level. The (π^+,π^-) DCX reaction (hereafter DCX will refer to (π^+,π^-) unless otherwise specified) on the oxygen isotopes is characterized by the following changes in isospin assignment, from the initial to the final-state nucleus:

$$^{16}O(\pi^+,\pi^-)^{16}Ne\ (g.s.) \quad \text{--} \quad (\Delta T=2, \Delta T_z=-2)$$

and

$$^{18}O(\pi^+,\pi^-)^{18}Ne\ (g.s.) \quad \text{--} \quad (\Delta T=0, \Delta T_z=-2)\ .$$

Transitions involving a change in T_z, and not the total isospin T, lead to isobaric-analog states. A $\Delta T_z=-1$ leads to the single-isobaric-analog state (IAS)[An-62], and those of $\Delta T_z=-2$ lead to double-isobaric-analog states (DIAS). The transitions themselves may be more precisely characterized: transitions connecting initial and analog states directly are properly called isobaric-analog transitions (IAT or DIAT), while those passing through non-analog intermediate states are non-(D)IAT. At the simplest level, analog-state wave functions differ from those of the initial state in only the isospin component — there is unity overlap in the remaining parts.

The ground state of ^{18}Ne is the DIAS of the ^{18}O ground state. Referring to Figure 1-2 it is possible to identify the principal process of the DCX reaction to the DIAS as simply changing the two $1d_{5/2}$ neutrons into $1d_{5/2}$ protons. Identifying the two nucleons involved in the reaction makes it possible to look for correlations between them. Comparisons between ^{18}O and ^{16}O may determine the relative strengths of DIAT and non-DIAT transition routes, which would bear on the reaction mechanism. Comparisons of DCX reactions on several T=0,1 pairs, of differing nuclear structure, would help separate reaction-mechanism from nuclear-structure effects in the data.

Prior to the experiments reported here, there had been few or no reliable experimental constraints to the development of theory pertaining to DCX reactions, as demonstrated in Figure 1-3. Previously, the experiments have been very difficult to perform (poor resolution, low counting rates, etc.) and have resulted in very little data [Co-68] [Gi-64], or have produced ambiguous results [Gi-64] [Bo-68]. Early high-resolution experiments also provided too little data [Ma-77] [Co-79] [Se-79] to resolve the various issues discussed above.

Accurate DCX measurements would have a variety of uses. High-quality data could be used to help pin down the optical-model description of the π-nucleus interaction; discriminating between various formulations of the potential in first or second order. The presence of correlations would bear directly on such a description. Since the reaction involves a double isospin flip of the pion, it should be sensitive to the isospin structure of the nucleus. DCX

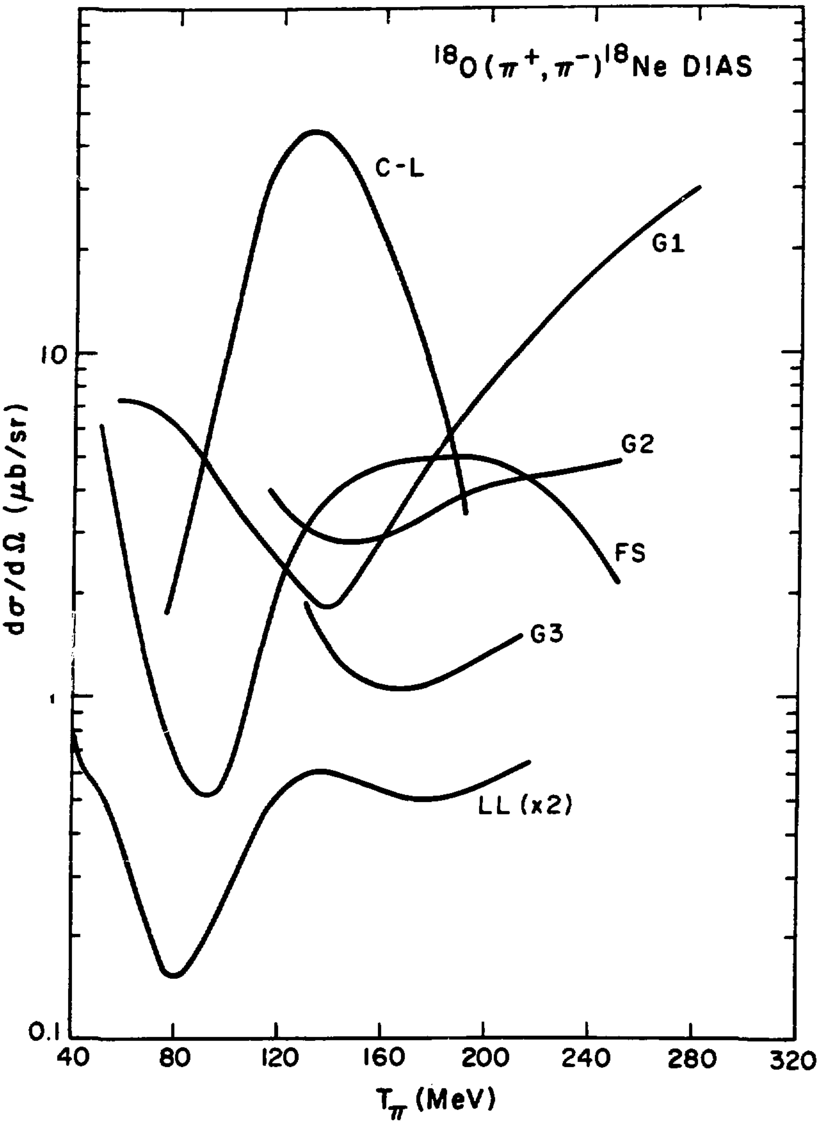

FIGURE 1-3. Theoretical predictions of the $^{18}O(\pi^+,\pi^-)^{18}Ne$ DIAS energy excitation function before the appearance of data. C-L, Chew-Low model of [Pa-65]; G1, G2, and G3, Glauber calculations of [Li-75], [Os-78], and [Li-80]; FS, fixed scatterer of [Ka-74]; LL, local Laplacian of [Mi-76].

reactions may also be used as a tool for the creation and study of proton-rich nuclei far from the line of nuclide stability (masses, structure, etc.).

The experiments reported here constitute the first step in a program of systematic investigation into DCX reactions. A collaboration [Gr-79] comprising physicists from the University of Texas at Austin, New Mexico State University, and Los Alamos National Laboratory utilized a high-resolution pion spectrometer facility to make these (π^+,π^-) measurements. The measurements include angular distributions and energy excitation functions of the differential cross section $d\sigma/d\Omega$. Measurements were made for the two $T=0,1$ isotopic pairs $^{16,18}O$ and $^{24,26}Mg$, providing a basis for comparison of DIAS and non-DIAS processes with various nuclear structure. Cross sections were also determined for targets of ^{9}Be, $^{12,13}C$, and ^{32}S in the course of using DCX as a means for measuring the ground-state masses of various proton-rich nuclei, for the purpose of testing the mass formula of Wigner [Wi-57]. Also, evidence was obtained for the observation of the DIAS in the reaction $^{209}Bi(\pi^+,\pi^-)^{209}At$.

Chapter II of this work details the experimental facility and the modifications to it developed for this set of measurements. Chapter III presents the data measured during all parts of the experiment. Chapter IV discusses the data, in terms of the observed systematics and comparisons of the $T=0,1$ pairs, and examines the A-dependence of the data. Appendices I and II are brief descriptions of theoretical and experimental DCX history. Appendix III reproduces the report of the mass measurement work incorporated into these experiments. Appendix IV is a description of a simple two-amplitude model of the ^{18}O excitation function, which is consistent with the observed systematics. The measurement of $^{209}Bi(\pi^+,\pi^-)^{209}At$ (DIAS) is discussed in Appendix V. Appendix VI is a tabulation of the DCX cross sections measured here.

II. EXPERIMENTAL SETUP

The (π^+,π^-) double-charge-exchange experiments reported here were performed on the Energetic Pion Channel and Spectrometer (EPICS) at the Clinton P. Anderson Meson Physics Facility (LAMPF) of the Los Alamos National Laboratory. Research at LAMPF centers about an 800-MeV proton linear accelerator (Figure 2-1). The primary proton beam currents are ~550 μA of H^+ and ~10 μA of H^-, both beams being accelerated simultaneously in alternating bunches. This translates to a proton flux for H^+ of $\sim 3.4\times 10^{15}$ p/s. After acceleration, the H^- is stripped of both electrons and the resulting protons are generally used for nucleon-nucleon and nucleon-nucleus interaction experiments. A polarized-spin H^- beam may also be accelerated, with currents in the nA range.

The H^+ beam is used primarily for the production of secondary pion beams. This proton beam (the world's most intense medium-energy beam) passes through several pion production targets which feed secondary beam channels with fluxes on the order of 10^8–10^9 π/s. This is the principal justification of the LAMPF facility, earning it the sobriquet "meson factory". The current extent of the meson experimental area is diagrammed in Figure 2-2.

The primary goal of the DCX program is to determine the DCX reaction mechanism and its uses as a probe of nuclear structure. As outlined in Appendix II it is known that the differential cross section, $d\sigma/d\Omega$, is extremely small for this reaction — on the order

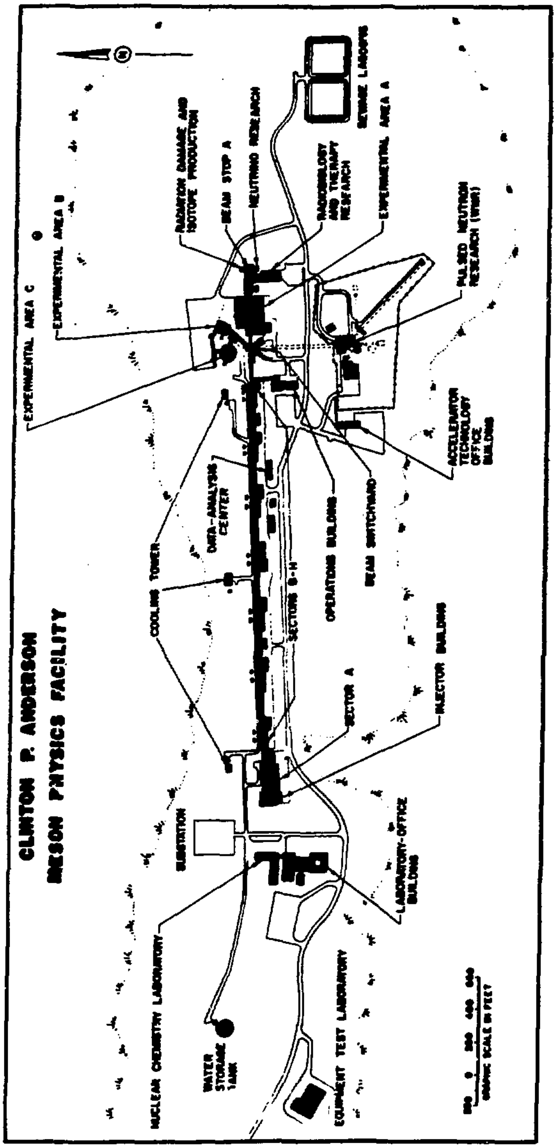

FIGURE 2-1. Plan view of the LAMPF site.

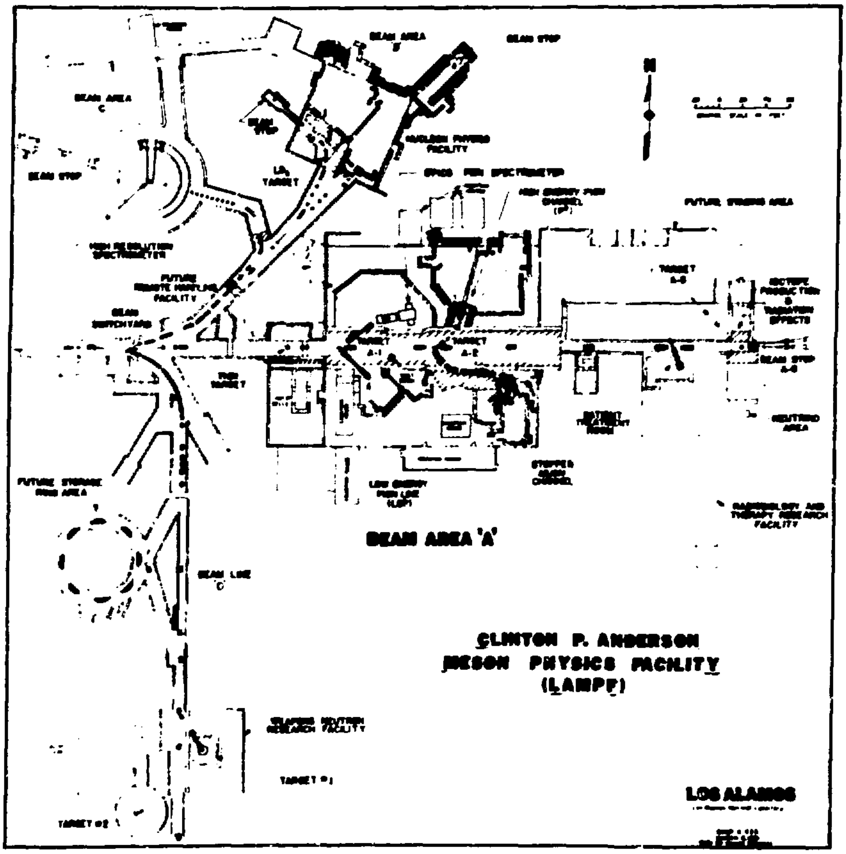

FIGURE 2-2. Plan view of the LAMPF experimental areas.

of 1 μb/sr. Several types of accurate measurements are necessary to understand what DCX reactions can tell us; its behavior as a function of incident and final pion kinematics, and the dependence of the reaction on the number and type of target nucleons. Reaction-mechanism effects are separated from nuclear-structure effects by comparisons of the data of similar experiments involving targets of differing nuclear structure.

The above requires high-resolution spectroscopy of the levels excited by the reaction, so that contributions from differing processes may be unambiguously resolved. The count rate needs to be high enough to allow systematic experimentation in a reasonable time, since any such high-resolution facility is bound to be in great demand. Fortunately, one such facility exists — the EPICS facility at LAMPF. Knowing that the angular distribution for the reaction $^{18}O(\pi^+,\pi^-)^{18}Ne$ DIAS seemed to peak at the forward direction, in the microbarn range, it was determined that (with a reasonable fraction of the heavily-subscribed EPICS beam time) these experiments could be successfully pursued.

The goals of the proposed experiments were several; to examine the forward-angle energy dependence of the DCX reaction across the (3,3) resonance for the two T=0,1 pairs $^{16,18}O$ and $^{24,26}Mg$; to study the angular behavior of the DIAS transitions, especially in light of the report of anomalous behavior observed in the $^{18}O \rightarrow ^{18}Ne$ DIAS [Se-79]; to start investigating the A- (or N and Z)

TABLE 2-1.

a) EPICS pion beam parameters.

CHANNEL		SPECTROMETER	
Solid angle	3.4 msr	Solid angle	~10 msr
$\Delta p/p$	2%	$\Delta p/p$	14%
Beam size (horizontal)	8 cm	Momentum range	100-750 MeV/c
Beam size (vertical)	20 cm	Flight path	~12.5 m
Beam divergence (horizontal)	<10 mrad	Dispersion	4 cm/%
Beam divergence (vertical)	100 mrad		
Energy range	50-300 MeV		

b) EPICS pion flux at various energies.*

T_π (MeV)	($\times 10^7\ \pi^+/s$)	($\times 10^7\ \pi^-/s$)
70	3.1 ± 0.2	1.0 ± 0.02
100	6.7 ± 1.0	1.8 ± 0.1
145	14.0 ± 3.0	3.4 ± 0.2
193	22.0 ± 4.0	4.7 ± 0.2
245	25.0 ± 4.0	5.5 ± 0.1
292	26.0 ± 4.0	4.5 ± 0.2

---

*Normalized to 1mA primary proton beam current

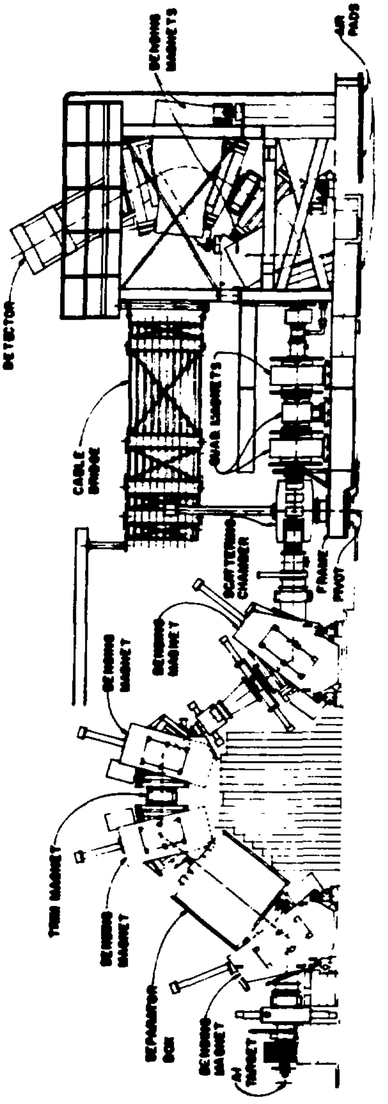

FIGURE 2-3. Elevation view of the EPICS system. The channel is left of the scattering chamber and the spectrometer is right.

dependence of DCX reactions; and, to further investigate the utility of DCX in mass measurements.

1. The EPICS Facility

The EPICS facility consists of a pion beam channel, scattering chamber, and high-resolution spectrometer [Th-70]. Together they form a VHV configuration: Vertical analysis/Horizontal scattering/Vertical analysis. The relevant system parameters are listed in Table 2-1a, and an elevation view of the facility is shown in Figure 2-3.

A. Pion Production Target

The macroscopic duty factor of the proton beam for these experiments was ~6.0%, which at a 120-Hz repetition rate gave a pulse length of 500 μs. The H^+ beam in Line A is focussed to a 2-mm (vertical) by 2-cm (horizontal) spot on the A-1 pion production target. A-1 is an ATJ-graphite wheel target [Ag-79]. The proton beam passes through the 3-cm thick wheel rim, parallel to the wheel axis. The target rotates at 58 rpm to safely distribute the ~8-kW heat load along the rim, giving an operating temperature of ~850°C. The EPICS channel views this target at 35° off the forward direction.

B. Pion Channel

The EPICS channel momentum analyzes scattered particles through four vertical bending dipole magnets of 52.5°, providing a momentum-dispersed beam to the pion scattering target [Th-77]. The basic channel design and optics are shown in Figure 2-4. In addition to the dipoles (BM01-4), there are a variety of adjustable slits (FJ's) and multipole trim magnets (FM's) to assist in defining the parameters (size, dispersion, Δp) of the (mostly) pion beam. The momentum dispersion technique correlates each particle's momentum with its vertical position in the beam, with respect to the central momentum axis. Momentum dispersion has the advantage of allowing increased pion flux, by a factor of ~100, over an equivalent monochromatic channel. The dispersion in the channel is $\delta p/p = \pm 1\%$, where p is the central momentum. The pion flux is related to the proton flux at A-1 which is accurately monitored. The pion flux, as a function of kinetic energy, is listed in Table 2-1b. The pion kinetic energy is tunable over the range of ~70 up to ~300 MeV.

C. Targets

Pion scattering targets are positioned in a scattering chamber at the focal plane of the channel. The maximum target area (full-size beam spot) is 20-cm vertical by 8-cm horizontal. The momentum dispersion is in the vertical plane, forming a dispersion across the target of 10 cm/percent. Target thickness (areal density) to be used is determined by the resolution and count-rate requirements of the individual experiments. The optimum thickness for highest resolution in mass measurements occurs at a point where the resolution loss through the target (caused by straggling) equals the intrinsic resolution of the system. Less stringent resolution requirements, for cross section measurements, allow thicker targets

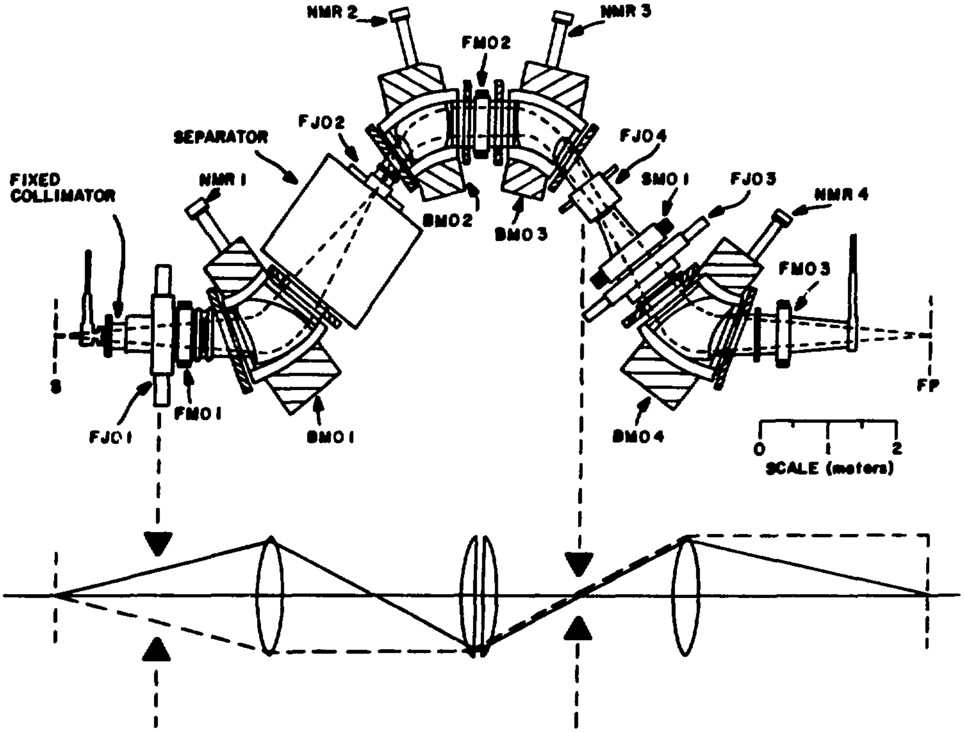

FIGURE 2-4. Elevation view of the EPICS pion channel, detailing the beam optics (dashed=horizontal, solid=vertical). S is the pion source, FP is the focal plane where scattering targets are placed.

and therefore higher count rates. Typical EPICS target thicknesses range from 100 up to 1000 mg/cm^2.

D. Spectrometer

The vertical axis of the target plane is the pivot point of the spectrometer. As seen in Figure 2-5, the magnetic elements consist of a quadrupole triplet focussing element and two momentum-analyzing dipoles. The spectrometer views the target with a 10 msr solid angle, effectively subtending 3° of scattering angle. The symmetric quadrupole triplet focusses the scattered particles to form a target image at the front focus of the analyzing dipoles. Particle trajectories are projected; from the front focus back to the target to determine the incident momenta, and from the front focus through the 120° bending dipoles to the rear focal plane to determine the scattered momenta.

E. Detectors

A set of delay-line-readout, multi-wire drift chambers (F1-4) is positioned at the front focus of the spectrometer. Two sets of x and y planes determine the particle trajectories at this point, which are projected back to the scattering target, defining the scattering coordinates (x,y,θ,ϕ), x being determined to $\pm\sim1$ mm. This determines the incident momentum and scattering angles.

Scintillator S1 is located directly before these chambers. It is generally used for time-of-flight (TOF) discrimination of particle identity (PID). This discrimination may be accomplished

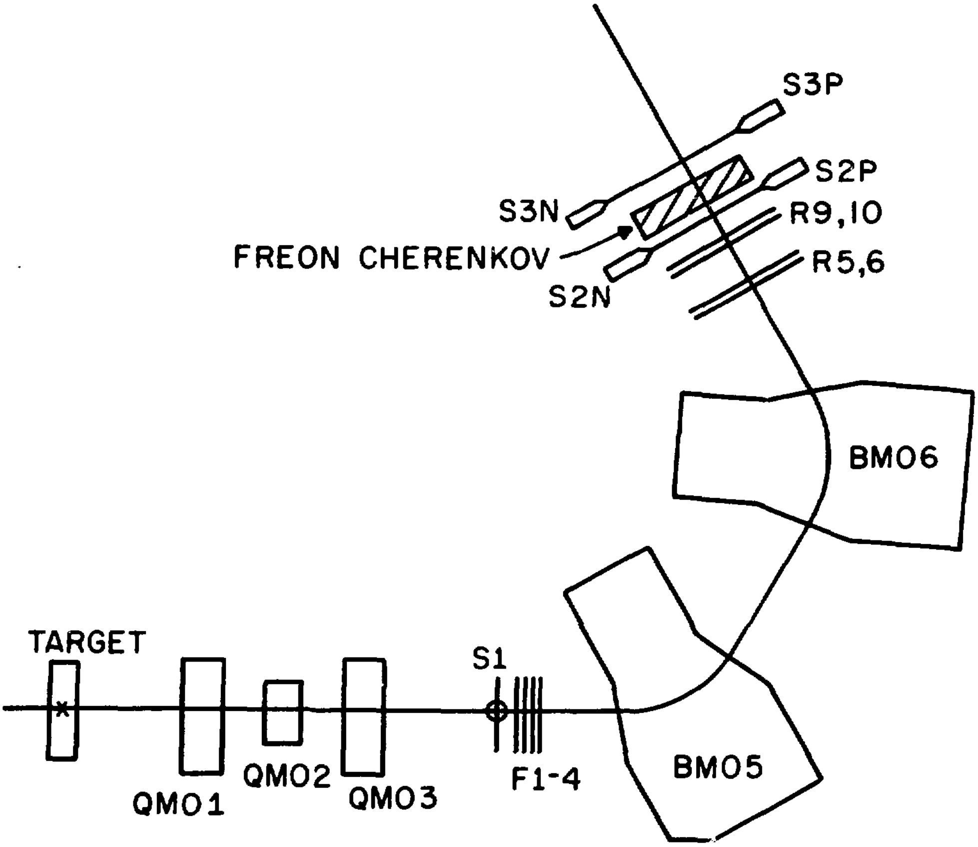

FIGURE 2-5. Schematic elevation of the EPICS spectrometer showing relative magnet and detector placements about the central momentum line.

with respect to either the radio-frequency time structure of the beam or in relation to scintillators further along the spectrometer.

After being momentum analyzed the particles are dispersed across ~90 cm at the rear focal plane. his focal plane is largely a software construct, not a physical plane. The first elements of the detector stack are another pair of wire chambers (R5,6) and (R9,10). The x and y coordinates here are used to ray trace the particle trajectories, through the dipoles from the front focus, determining the momenta of the scattered particles. Scintillator S2, following the rear chambers, is again used for timing. This is followed by a freon-12 gas (atmospheric pressure) Cherenkov counter, used as an electron-veto counter. In the momentum range of the spectrometer (<750 MeV/c), only electrons have a sufficiently large β (v/c) to produce Cherenkov radiation in this gas. Tests conducted of S1-S2 TOF versus Cherenkov pulse showed that electron-rejection efficiencies were >99.5% at all but the lowest energy (80 MeV). Except at that energy we were able to run without S1 in the beam, eliminating it as a source of multiple scattering, which contributes to worsening the resolution and decreasing the spectrometer acceptance. Finally, S3 may be used for TOF in conjunction with S1 and/or S2, or as part of a muon-ranging veto counter to discriminate against muons.

F. Data Acquisition

The configuration of the EPICS electronic and software logic for signal processing is relatively stable. Figure 2-6 details the

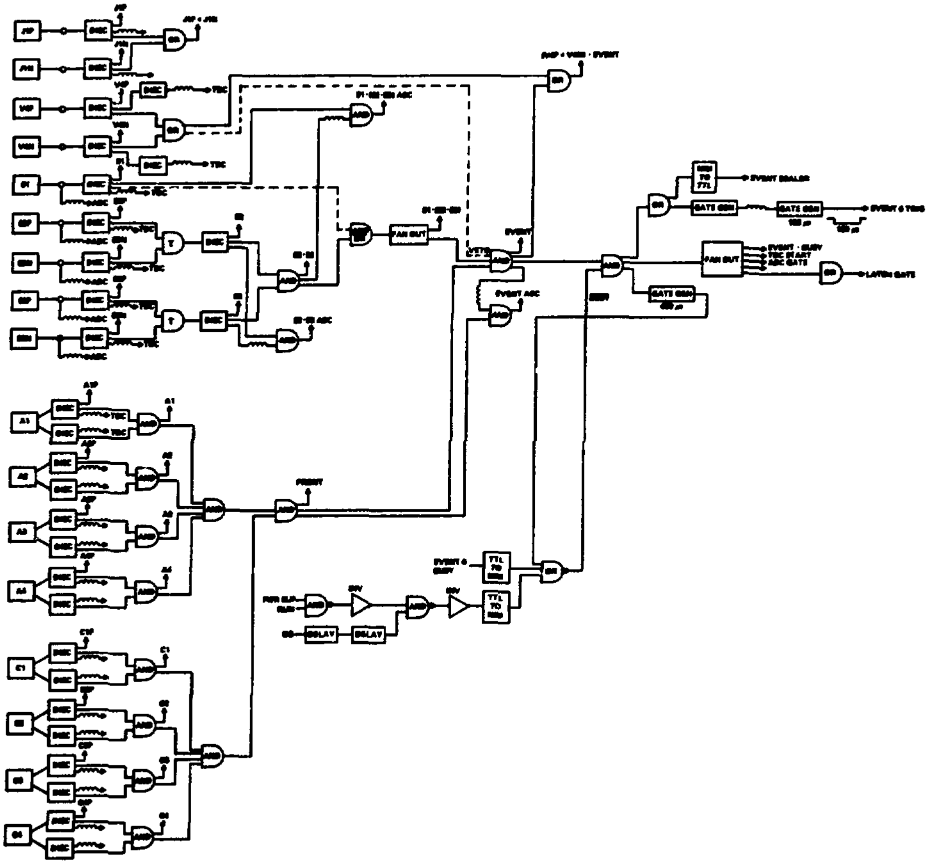

FIGURE 2-6. Diagrammatic layout of the EPICS fast electronic logic.

electronic logic system used here. The "raw" detector signals entering the counting house are amplified and/or discriminated to provide appropriate amplitude or timing signals for logical analysis. The figure shows how various combinations of signals and relative times are used to classify events in terms of good scatters. Fast NIM [US-78] electronics perform this initial processing. The record of events (number, amplitude, timing), as determined in the electronics, is recorded in digital form in CAMAC [Eu-69] (scalers, ADC's, TDC's, etc.).

Good scattering events (EVENT 6) generate a trigger signal to a PDP 11/45 computer, causing it to read the CAMAC registers. The record of CAMAC is written directly to magnetic tape for subsequent off-line analysis. If the computer is not otherwise busy, it analyzes the record of events, classifying them in relation to a prescribed series of tests.

The data-acquisition and analysis software is broken down into three subgroups: the calculational ANALYZER programs, the data-testing ALLTEST routine, and the histogramming DISPLAY package. All data-taking activities are interfaced to the hardware through this set of software [Am-79] [Bo-79].

The ANALYZER, using the position and timing information, calculates the trajectories and scattering coordinates of the particles — thus determining their momenta. After this a data-testing package, ALLTEST, processes each event through a series of micro and macro tests; in which micro tests check each data word and calculation with respect to prescribed limits, and macro tests logically combine various micro tests. A sample of the ALLTEST file, where each test is executed sequentially, appears in Table 2-2. The classification of events is determined here (PID, accidentals, etc.). The results of these calculations and tests may be displayed in the form of histograms and scatter plots, at an on-line CRT terminal. These displays are easily created and manipulated through the DISPLAY routines, allowing the data to be examined with respect to the calculated quantities of ANALYZER and the various tests of ALLTEST. This on-line analysis occurs only if time between events is available, reading events from CAMAC and writing them to tape having higher priority. The same software package may be used off line to process records from the magnetic tape, without time constraints.

G. Beam Monitoring and Normalization

The relative intensity of the incident pion beam is monitored by placing two ion chambers directly in the unscattered beam downstream of the target. The pion flux is also directly related to the intensity of the proton beam at A-1, which is continuously monitored and recorded.

Normalization to the absolute number of incident pions is made by the comparison of experimental cross sections for π^{+}-^{1}H with those predicted from free π^{+}-p phase shifts [Ro-78] [Do-79]. This measurement was performed at all energies where data were taken, and is estimated to be good to the 10% level.

TABLE 2-2. Sample of the data testing file ALLTEST.

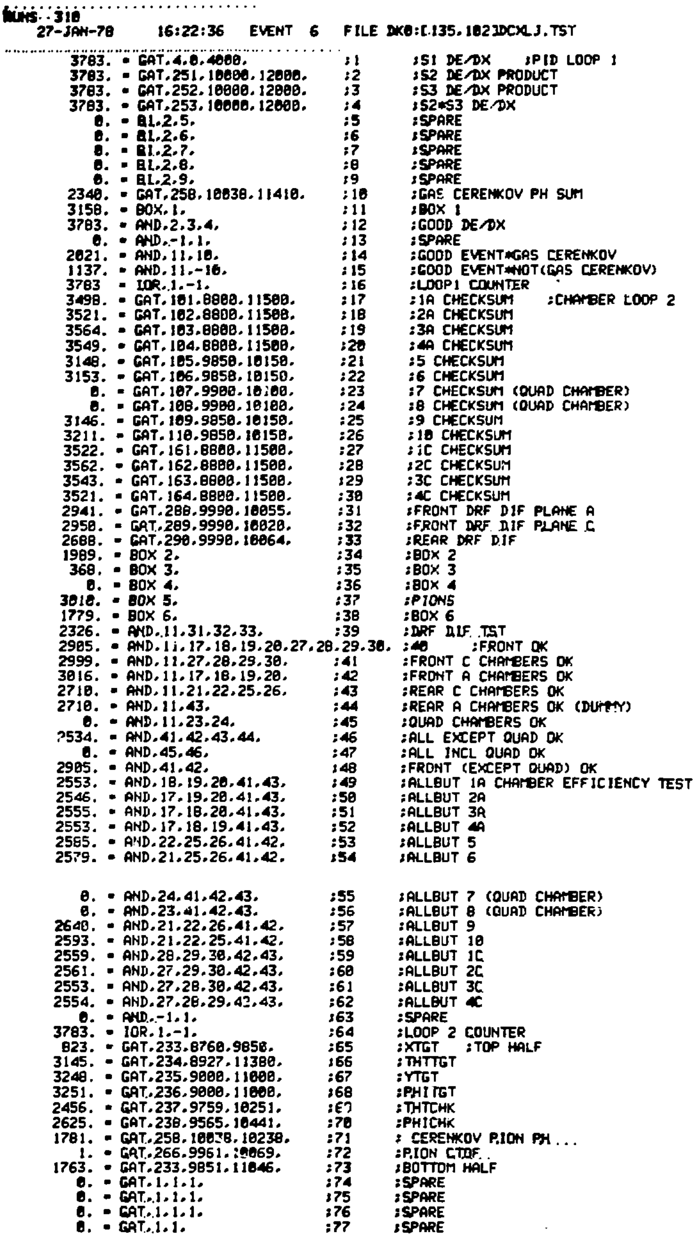

```
NUMS..310
   27-JAN-78     16:22:36   EVENT  6   FILE DK0:[135,102]DCXLJ.TST

       3783. = GAT,4,0,4000,              ;1       ;S1 DE/DX    ;PID LOOP 1
       3783. = GAT,251,10000,12000,       ;2       ;S2 DE/DX PRODUCT
       3783. = GAT,252,10000,12000,       ;3       ;S3 DE/DX PRODUCT
       3783. = GAT,253,10000,12000,       ;4       ;S2*S3 DE/DX
          0. = BL,2,5,                    ;5       ;SPARE
          0. = BL,2,6,                    ;6       ;SPARE
          0. = BL,2,7,                    ;7       ;SPARE
          0. = BL,2,8,                    ;8       ;SPARE
          0. = BL,2,9,                    ;9       ;SPARE
       2340. = GAT,258,10030,11410,       ;10      ;GAS CERENKOV PH SUM
       3150. = BOX,1,                     ;11      ;BOX 1
       3783. = AND,2,3,4,                 ;12      ;GOOD DE/DX
          0. = AND,-1,1,                  ;13      ;SPARE
       2021. = AND,11,10,                 ;14      ;GOOD EVENT*GAS CERENKOV
       1137. = AND,11,-10,                ;15      ;GOOD EVENT*NOT(GAS CERENKOV)
       3783  = IOR,1,-1,                  ;16      ;LOOP1 COUNTER
       3490. = GAT,101,8800,11500,        ;17      ;1A CHECKSUM     ;CHAMBER LOOP 2
       3521. = GAT,102,8800,11500,        ;18      ;2A CHECKSUM
       3564. = GAT,103,8800,11500,        ;19      ;3A CHECKSUM
       3549. = GAT,104,8800,11500,        ;20      ;4A CHECKSUM
       3140. = GAT,105,9850,10150,        ;21      ;5 CHECKSUM
       3153. = GAT,106,9850,10150,        ;22      ;6 CHECKSUM
          0. = GAT,107,9900,10100,        ;23      ;7 CHECKSUM (QUAD CHAMBER)
          0. = GAT,108,9900,10100,        ;24      ;8 CHECKSUM (QUAD CHAMBER)
       3146. = GAT,109,9850,10150,        ;25      ;9 CHECKSUM
       3211. = GAT,110,9850,10150,        ;26      ;10 CHECKSUM
       3522. = GAT,161,8800,11500,        ;27      ;1C CHECKSUM
       3562. = GAT,162,8800,11500,        ;28      ;2C CHECKSUM
       3543. = GAT,163,8800,11500,        ;29      ;3C CHECKSUM
       3521. = GAT,164,8800,11500,        ;30      ;4C CHECKSUM
       2941. = GAT,288,9990,10055,        ;31      ;FRONT DRF DIF PLANE A
       2950. = GAT,289,9990,10020,        ;32      ;FRONT DRF DIF PLANE C
       2688. = GAT,290,9990,10064,        ;33      ;REAR DRF DIF
       1989. = BOX 2,                     ;34      ;BOX 2
        368. = BOX 3,                     ;35      ;BOX 3
          0. = BOX 4,                     ;36      ;BOX 4
       3010. = BOX 5,                     ;37      ;PIONS
       1779. = BOX 6,                     ;38      ;BOX 6
       2326. = AND,11,31,32,33,           ;39      ;DRF DIF TST
       2905. = AND,11,17,18,19,20,27,28,29,30, ;40     ;FRONT OK
       2999. = AND,11,27,28,29,30,        ;41      ;FRONT C CHAMBERS OK
       3016. = AND,11,17,18,19,20,        ;42      ;FRONT A CHAMBERS OK
       2710. = AND,11,21,22,25,26,        ;43      ;REAR C CHAMBERS OK
       2710. = AND,11,43,                 ;44      ;REAR A CHAMBERS OK (DUMMY)
          0. = AND,11,23,24,              ;45      ;QUAD CHAMBERS OK
       2534. = AND,41,42,43,44,           ;46      ;ALL EXCEPT QUAD OK
          0. = AND,45,46,                 ;47      ;ALL INCL QUAD OK
       2905. = AND,41,42,                 ;48      ;FRONT (EXCEPT QUAD) OK
       2553. = AND,18,19,20,41,43,        ;49      ;ALLBUT 1A CHAMBER EFFICIENCY TEST
       2546. = AND,17,19,20,41,43,        ;50      ;ALLBUT 2A
       2555. = AND,17,18,20,41,43,        ;51      ;ALLBUT 3A
       2553. = AND,17,18,19,41,43,        ;52      ;ALLBUT 4A
       2585. = AND,22,25,26,41,42,        ;53      ;ALLBUT 5
       2579. = AND,21,25,26,41,42,        ;54      ;ALLBUT 6

          0. = AND,24,41,42,43,           ;55      ;ALLBUT 7 (QUAD CHAMBER)
          0. = AND,23,41,42,43,           ;56      ;ALLBUT 8 (QUAD CHAMBER)
       2640. = AND,21,22,26,41,42,        ;57      ;ALLBUT 9
       2593. = AND,21,22,25,41,42,        ;58      ;ALLBUT 10
       2559. = AND,28,29,30,42,43,        ;59      ;ALLBUT 1C
       2561. = AND,27,29,30,42,43,        ;60      ;ALLBUT 2C
       2553. = AND,27,28,30,42,43,        ;61      ;ALLBUT 3C
       2554. = AND,27,28,29,42,43,        ;62      ;ALLBUT 4C
          0. = AND,-1,1,                  ;63      ;SPARE
       3783. = IOR,1,-1,                  ;64      ;LOOP 2 COUNTER
        823. = GAT,233,8760,9850,         ;65      ;XTGT    ;TOP HALF
       3145. = GAT,234,8927,11380,        ;66      ;THTTGT
       3240. = GAT,235,9000,11000,        ;67      ;YTGT
       3251. = GAT,236,9000,11000,        ;68      ;PHITGT
       2456. = GAT,237,9759,10251,        ;69      ;THTCHK
       2625. = GAT,238,9565,10441,        ;70      ;PHICHK
       1781. = GAT,258,10030,10230,       ;71      ; CERENKOV PION PH ...
          1. = GAT,266,9961,10069,        ;72      ;PION CTOF..
       1763. = GAT,233,9851,11046,        ;73      ;BOTTOM HALF
          0. = GAT,1,1,1,                 ;74      ;SPARE
          0. = GAT,1,1,1,                 ;75      ;SPARE
          0. = GAT,1,1,1,                 ;76      ;SPARE
          0. = GAT,1,1,                   ;77      ;SPARE
```

TABLE 2-2. continued

```
      0. = GAT.1.1.1.              :78        :E
      0. = IGAT.1.                 :79       ;Q GATE 1
      0. = IGAT.2.                 :80       ;QGATE 2
     97. = GAT.233.9000.9297.      :81       ;ROD 1
    353. = GAT.233.9492.9600.      :82       ;ROD 2
    459. = GAT.233.9869.10008.     :83       ;ROD 3
    420. = GAT.233.10302.10402.    :84       ;ROD 4
    124. = GAT.233.10696.10907.    :85       ;ROD 5
      0. = AND.-1.1.               :86       ;SPARE
      0. = AND.47.65.66.67.68.     :87       ;TARGET TESTS WITH QUADS
      0. = AND.69.70.87.39.        :88       ;GOOD EVENT WITH QUADS
   2506. = IOR.65.73.              :89       ;XTARG
   1970. = AND.46.89.66.67.68.     :90       ;TARGET TESTS
   2008. = AND.46.69.70.           :91       ;THTCHK AND PHICHK
   2204. = AND.39.46.              :92       ;GOOD CHMBRS ==> DRF=CHKSUM
   1666. = AND.90.91.39.           :93       ;GOOD EVENT
   1352. = AND.93.37.              :94       ;GOOD EVENT (PION)
    314. = AND.93.-37.             :95       ;GOOD EVENT (ELECTRON)
      0. = AND.93.86.              :96       ;XTARG GATE AND DELTA
    640. = GAT.236.9739.9913.      :97       ;PHITGT -1 DEG.
    701. = GAT.236.9913.10087.     :98       ;PHITGT 0 DEG
    772. = GAT.236.10087.10261.    :99       ;PHITGT +1 DEG
   3251. = GAT.236.9000.11000.     :100      ;PHITGT FULL ACCEPTANCE
    441. = GAT.233.8760.9519.      :101      ;XTARG  #1 (TOP)
   1552. = GAT.233.9519.10256.     :102      ;XTARG #2 (CENTER)
   1110. = GAT.233.10256.11046     :103      ;XTARG #3 (BOTTOM)
      0. = GAT.1.1.1.              :104      ;SPARE
      0. = GAT.1.1.1.              :105      ;SPARE
    816. = AND.71.93.              :106      ;GOOD EVENT.PION PH
      0. = AND.72.93.              :107      ;GOOD EVENT.PION CTOF
      0. = AND.79.94.              :108      ;PION IN QGATE 1
      0. = AND.80.106.107.         :109      ;PION IN QGATE 2
    283. = AND 94.97.              :110      ;FULL TGT -1 DEG. .PIONS
    332. = AND 94.98.              :111      ;FULL TGT 0 DEG. .PIONS.
    356. = AND 94.99.              :112      ;FULL TGT +1 DEG.  .PIONS.
   1352. = AND 94.100.             :113      ;FULL TGT FULL ACCEPT .PIONS.

    971. = IOR 110.111.112.        :114      ;CENTER 3 DEG BINS SUM
     65. = AND.95.97.              :115      ;-1DEG. ELECTRONS
     80. = AND.95.98.              :116      ; 0DEG. ELECTRONS
     77. = AND.95.99.              :117      ;+1DEG. ELECTRONS
    314. = AND.95.100.             :118      ;FULL ACCEP. ELECTRONS
    222. = IOR.115.116.117.        :119      ;3DEG SUM. ELECTRONS
   1524. = AND.93.34.              :120      ;GOOD EVENT*BOX 2
      0. = AND.93.35.              :121      ;GOOD EVENT*BOX 3
      0. = AND.93.36.              :122      ;GOOD EVENT*BOX 4
   1352. = AND.93.37.              :123      GOOD EVENT*BOX 5
    213. = AND.113.101.            :124      ;FULL ACCEP. PIONS. TOP TGT
    546. = AND.113.102.            :125      ;FULL ACCEP. PIONS. MID TGT
    593. = AND.113.103.            :126      ;FULL ACCEP. PIONS. BOT TGT
   3783. = IOR.1.-1.               :127      ;LOOP 4 COUNTER (WHOOPEE WERE DONE)

BOX CUTS FOR EVENT  6

BOX 1. X VAR=253. Y VAR=260  10116<X<10769  10374<Y<11199
BOX 2. X VAR=237. Y VAR=238   9857<X<10118   9746<Y<10262
BOX 3. X VAR=233. Y VAR=235   9770<X< 9930   9500<Y<10500
BOX 4. X VAR=266. Y VAR=222  10072<X<10228   8925<Y<11137
BOX 5. X VAR=266. Y VAR=258   5000<X<15000  10000<Y<10055
BOX 6. X VAR=279. Y VAR=280   8923<X<10956   9669<Y<10559
BOX 7. X VAR=279. Y VAR=280   8923<X<10956   9669<Y<10559
BOX 8. X VAR=279. Y VAR=280   8923<X<10956   9669<Y<10559
BOX 9. X VAR=279. Y VAR=280   8923<X<10956   9669<Y<10559
BOX10. X VAR=279. Y VAR=280   8923<X<10956   9669<Y<10559

INDIRECT GATES FOR EVENT  6
GATE  1. INDEX=  1:       0-      0
GATE  2. INDEX=  1:       0-      0
GATE  3. INDEX=  1:       0-      0
GATE  4. INDEX=  1:       0-      0
GATE  5. INDEX=  1:       0-      0
GATE  6. INDEX=  1:       0-      0
GATE  7. INDEX=  1:       0-      0
GATE  8. INDEX=  1:       0-      0
GATE  9. INDEX=  1:       0-      0
GATE 10. INDEX=  1:       0-      0
GATE 11. INDEX=  1:       0-      0
GATE 12. INDEX=  1:       0-      0
GATE 13. INDEX=  1:       0-      0
```

The spectrometer acceptance and detector efficiencies were accurately mapped by positioning the peaks for π^+ elastic scattering from ^1H and ^{12}C at various points across the focal plane. Corrections corresponding to these effects were automatically applied to all the data. Spectrometer resolution was determined by measuring the width (fwhm) of the π^+ elastic-scattering peak from a 110-mg/cm^2 ^{12}C target. This measure of the "intrinsic" resolution yielded a value of 120 keV (fwhm), as shown in the histogram of Figure 2-7.

2. EPICS-DCX Modifications

Some modifications to the basic EPICS system were necessary for these DCX experiments. These were caused by the requirement to perform certain of the measurements at near-forward angles where the cross sections were largest. EPICS has the problem that at angles forward of ~18° the spectrometer starts to see an appreciable fraction of particles from the incident beam. Chambers F1-4 have a count-rate limit of ~1 MHz which can be significantly exceeded in this forward region. Higher rates degrade the ability of the system to unambiguously identify each particle, with a subsequent loss in detector efficiency and resolution. Yet the highest possible π^+ incident flux was needed to maximize the count rate for the states of interest. A method for running in the forward-angle region was needed whereby the (relatively) few π^- signals from F1-4 would not be drowned out by the large π^+ induced background.

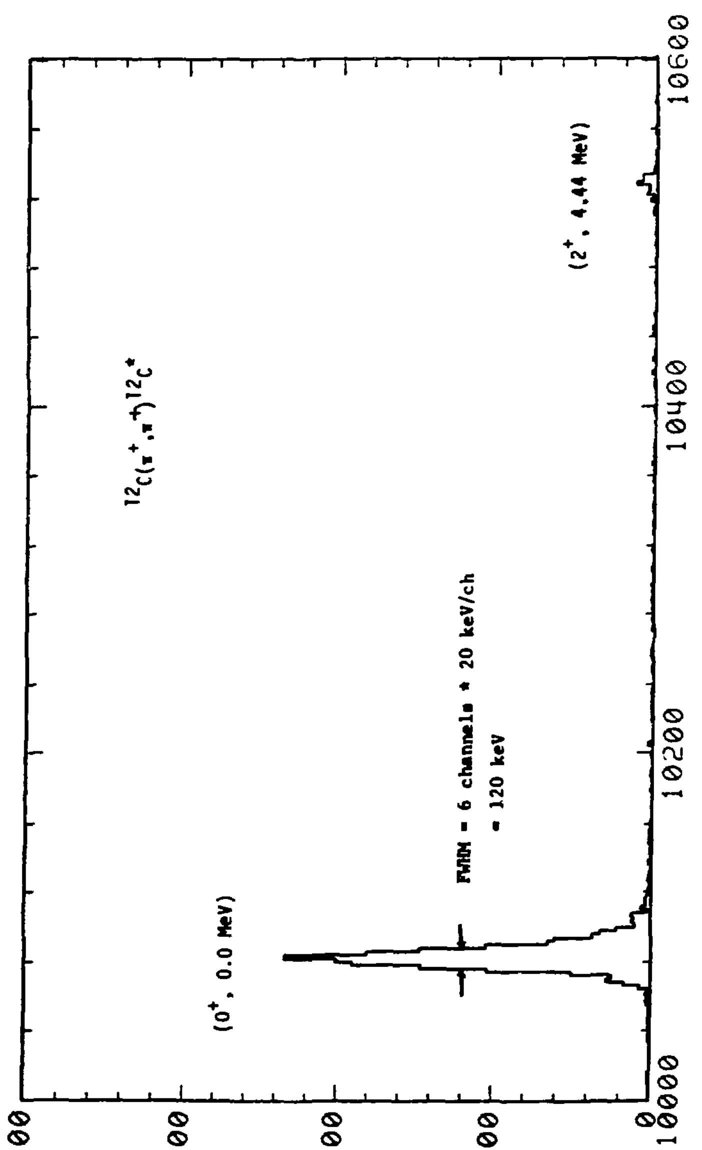

FIGURE 2-7. Excitation spectrum from $^{12}C(\pi^+,\pi^{+\prime})^{12}C$ using a 110 mg/cm^2 target. The resolution of the ground state is ~120 keV (fwhm).

A. Sweep Magnet

The technique of magnetically separating the charge-exchanged π^- beam and deflecting away the π^+ beam was investigated. It would be necessary to develop a system which would perturb the critical EPICS ray-tracing abilities as little as possible. The simple picture was to place a magnetic field after the target, before the spectrometer entrance, which would cause the oppositely charged pions to separate, as shown in Figure 2-8.

Ideally, a uniform dipole field which could be adjusted to allow the π^-'s of a given scattering angle and energy to normally enter the field boundary and normally exit toward the spectrometer, while deflecting the π^+'s away, was desired. The simple graphical analysis of Figure 2-8 indicated that this might be achieved with a circular dipole field between the target and the focussing triplet entrance.

The charged-particle beam-transport code TRANSPORT [Br-77] was used to model this concept. This computer program monitors the propagation of a beam phase space through interactions with magnetic transport elements (dipoles, quadrupoles, sextupoles, drifts, etc.). A beam of given initial condition (extents, divergences, momentum) is propagated through easily prescribed magnetic elements of various multipolarity and physical dimension. Maxwell's equations governing the motion of charged particles in external fields are solved, and a transport matrix acting on the beam parameters is calculated. This matrix is modified by each type of element as the beam is propagated

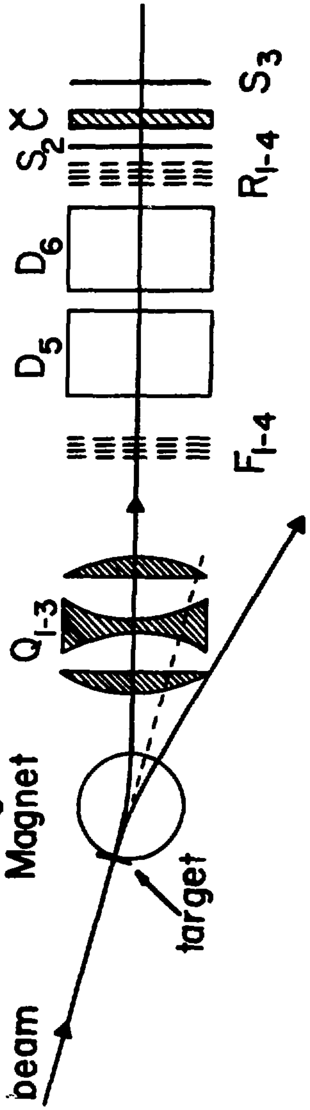

FIGURE 2-8. Schematic plan view of magnetic pion separation using a circular dipole magnet between the EPICS target and the spectrometer triplet entrance.

through the system. The calculation assumes ideal field structure inside each element of a given order, though it can also treat second-order effects associated with entrance and exit fringe fields of the elements. The code has features which allow it to search on element field strengths in efforts to optimize various focussing constraints.

The standard EPICS spectrometer was modelled, calculating the beam profile through the system, with a required target image at the front focus. This calculation agreed well with the measured transport matrix for both the front focus and at the rear focal plane. A circular dipole was then added to the calculation between the target and first quadrupole. The field strength of this magnet was set to induce a 10°-15° bend in the π^{-} beam, creating an opening angle of 20°-30° between the π^{-} and π^{+}. The π^{-} beam entered and exited normal to the field boundary. The quadrupole field strengths were allowed to vary either independently or as a symmetric triplet, being constrained to reproduce the target image at the front focus.

In this way, it was found that a 20° opening between π^{-} and π^{+} could be induced while maintaining the front focus with symmetric triplet fields and not seriously perturbing the ray-tracing capabilities of the spectrometer. A 20° opening angle would be sufficient to deflect the π^{+} beam enough to greatly reduce the F1-4 count rate at angles near 0°. This result rests on the assumption of relatively simple field shapes for the central and fringe regions of the circular dipole over the large extent of the EPICS beam, though experience has shown TRANSPORT to be a fairly reliable approximation tool. More accurate treatment would require replacing the standard TRANSPORT field models with actual field maps of the magnetic elements. This was deemed unnecessary for the existing EPICS magnets, and the field mapping of a real circular dipole would determine the acceptability of the TRANSPORT results.

A small, circular-pole C-magnet, borrowed from the University of Chicago, was acquired to implement this scheme. Known as the "Chicago-C", the pole-tip diameter was 53.34 cm (21 in), with the poles separated by a gap of 40.64 cm (16 in); this configuration is cataloged in the LAMPF magnet pool as C21(XVI)-21DIAM. The magnet was extensively field mapped to determine the field shape through the region the particles would traverse, from the target to the triplet entrance aperture. Three maps, parallel to the pole faces, were made; one map 2.54 cm (1 in) from each pole face, and one in the midplane corresponding to the central scattering plane. Each map was compiled from thousands of flip-coil measurements, forming a grid referenced to the magnetic pole axis. This shape was compared with the TRANSPORT model to determine how much confidence could be placed in the model predictions. Hand calculations of the integral $\int B \cdot d\ell$ indicated that the magnet would suffice.

The 10° deflection of the π^- beam directed it off the spectrometer optical axis. To correct for this the spectrometer frame was cut apart directly before the triplet entrance aperture and rejoined with a 10.16-cm (4 in) offset. This realigned the spectrometer to normal acceptance of the deflected beam, as shown in Figure 2-9. Provision was also made for larger offsets in the eventuality of using magnetic deflection techniques for the study of large, backward-angle scattering reactions.

A vacuum scattering chamber was constructed to be inserted between the C-magnet poles (Figure 2-10). Since the C-magnet was rigidly attached to the rotating spectrometer arm, the scattering chamber was directly coupled to the spectrometer vacuum line. In the interest of maximizing the resolution (hence visibility) of the weakly-excited DCX states, the scattering chamber was also vacuum coupled to the channel, eliminating all air gaps and windows in the pion flight path. This coupling was achieved through an experimental set of large-convolution, flexible bellows. This was the first attempt at complete vacuum coupling in the EPICS system, and so was treated as a test of the technique for eventual vacuum coupling of the standard EPICS scattering chamber which had been removed to accomodate the C-magnet. The bellows had been designed to allow an angular range of ±20° about the centerline, making the vacuum coupled range of scattering angles 0°-40°. However, at large deflections (near 0° and 40°) it was found that the large convolutions were too stiff to safely withstand the strain. Consequently the experimental angular range was limited to 5°-35° laboratory angle.

Since the new scattering chamber was less than the 40.64-cm gap width it was not possible to use the in-beam ion chambers to monitor the beam current. This was remedied by placing a

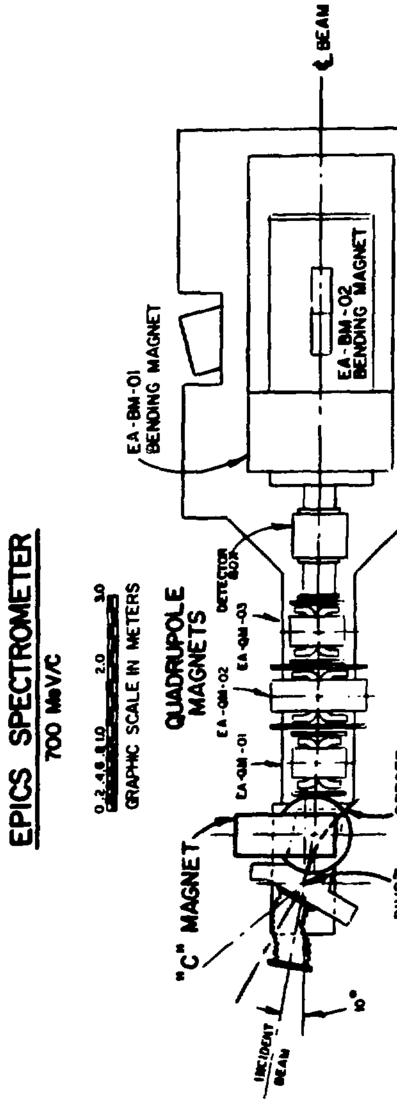

FIGURE 2-9. Plan view of the EPICS spectrometer with the C-magnet in place.

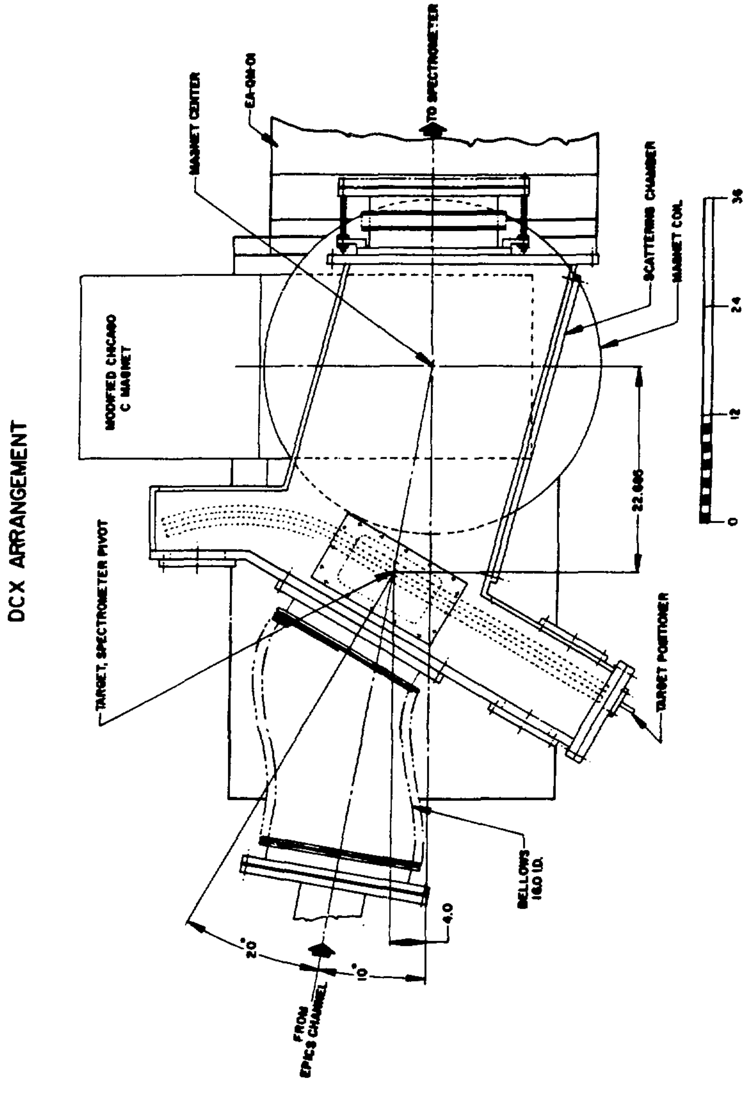

FIGURE 2-10. The C-magnet scattering chamber.

three-scintillator telescope directly above the target to monitor the 90° scattering and secondary-emission particles. This was an adequate substitute for the chambers in that all that was needed was a relative monitor of the beam intensity in relation to the proton current at A-1. Normalization to the absolute number of incident pions was accomplished as previously described.

B. DCX Targets

The isotopic targets used in the experiment were ^{9}Be, ^{12}C, ^{13}C, ^{16}O, ^{18}O, ^{24}Mg, ^{26}Mg, ^{32}S, and ^{209}Bi; their thickness, isotopic purity, and composition are listed in Table 2-3. The oxygen targets were in the form of water ice, highly enriched in the appropriate oxygen isotope. The ice was sandwiched between two thin copper foils (0.0025 cm) and surrounded by a heavy copper frame at the edges which provided the coupling to a refrigerator [Pa-79]. The ice temperature was held at ~-60°C. The Q value for DCX on copper (-7.8 MeV) was sufficiently different from DCX on oxygen (^{18}O: -5.1 MeV and ^{16}O: -28.4 MeV) that any DCX transitions from the copper were removed in energy from the states of interest. DCX from copper is also believed to be several orders of magnitude weaker than for oxygen. The ^{24}Mg was molecular MgO, with a Q-value difference between the two of 4.7 MeV.

TABLE 2-3. Targets, parameters, and differential cross sections for (π^+,π^-) at 5°_{lab} at 180 and 292 MeV.

Target	(mg/cm^2)	Chemical composition	Isotopic purity(%)	----$d\sigma/d\Omega$ ($\mu b/sr$)--- 180-MeV	292-MeV
^9Be	296	Be	100	0.15±0.03	
^{12}C	227	C	99	0.40±0.05	
^{13}C	356	C	90	0.10±0.03	
^{16}O	880	H_2O	100	0.34±0.04	0.12±0.02
^{18}O	1040	H_2O	95	0.88±0.10	2.40±0.19
^{24}Mg	235	MgO	100	0.11±0.03	0.014±0.005
^{26}Mg	409	Mg	100		1.00±0.14
^{32}S	250	S	95	0.084±0.025	
^{209}Bi	534	Bi	100		0.46±0.15

3. Data Analysis

Since data were taken with scintillator S1 both in and out of the beam, the focal-plane mapping (acceptance scan) was done for each case, and found to differ. Also, the pion flux varies as a function of energy, so the normalization to absolute pion number was done at each energy.

The pion scattering data were histogrammed as functions of the scattering coordinates (x,y,θ,ϕ), and as functions of the x position at the rear chambers, and in 1° and 3° bins each for pions and electrons. In the ALLTEST routine, limits (gates) may be placed on any of the scattering coordinates, along with logical AND's and OR's, to classify particles as acceptable or unacceptable, pions or electrons. Figure 2-11 shows a spectrum of the x distribution of particles across the target (vertical). Notice in the ALLTEST file of Table 2-2 that the XTARG gates (top and bottom) seem to cut out of the acceptance a small section across the middle of the target. This gates out particles scattering from a thin copper bar which passes through the target for cooling purposes. To separate pions from electrons, particles must pass gates requiring low Cherenkov pulse and a TOF range between S2 and S3.

The pions (electron rejected) are also histogrammed as a function of the calculated missing mass of the reaction, equivalently as an excitation-energy spectrum of the residual nucleus, as shown in Figure 2-12. The number of counts is summed over the central scattering angle $\pm 1^\circ$ on either side, with excitation energy

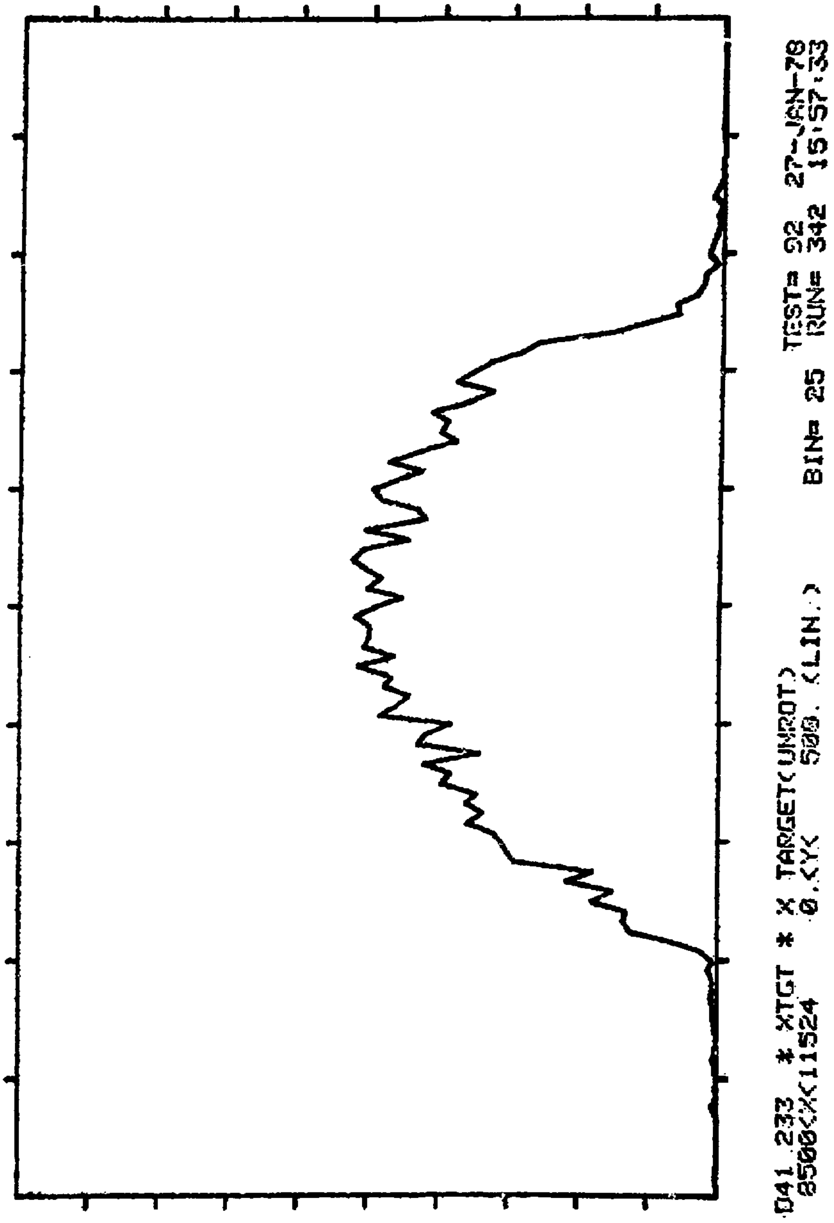

FIGURE 2-11. Distribution of particles across the target in the vertical (dispersion) direction.

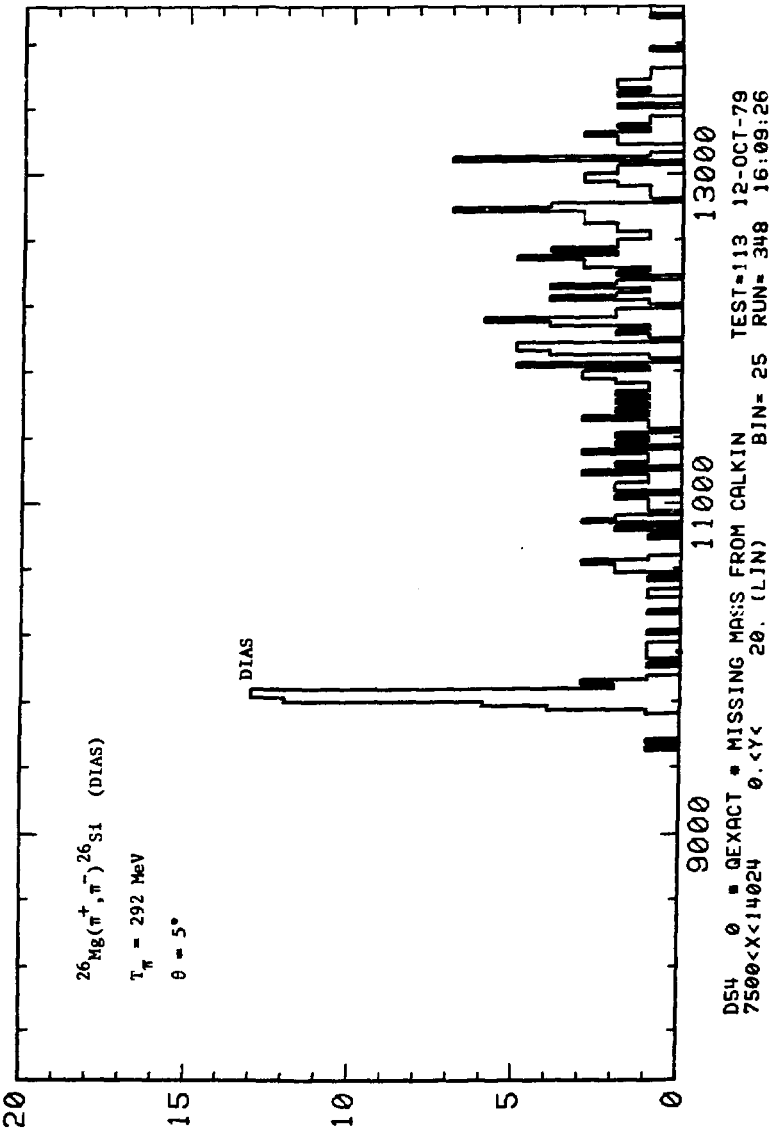

FIGURE 2-12. Energy excitation spectrum of the residual nucleus from the reaction ^{26}Mg(π^+,π^-)^{26}Si (g.s.,DIAS).

increasing toward the right. The width (fwhm) of the largest peak (the ground state) is ~600 keV.

The number of counts (area) in the excitation-spectrum peaks are extracted using two different peak-fitting routines. The first, PEKFIT [Sl-76], fits the peak to a Gaussian line shape, the accuracy being determined by the χ^2 of the fit. The second routine, LOAF [Sm-79], has the ability to fit to a specified line shape, including the shape of some reference peak. A majority of the data acquired here is in peaks of small area — on the order of 30 counts. Background under the peaks generally presented no problems and was easily determined by considering the apparent continuum of counts in the vicinity of the peaks. A typical PEKFIT fit is shown in Figure 2-13. The areas extracted by the separate routines were uniformly similar and mostly identical.

Cross sections were determined from the fitted areas using the following prescription:

$$\frac{d\sigma_{DCX}}{d\Omega} = \frac{Y_H}{\sigma_H \times G} \times Y_{DCX} \times \frac{CH_2(\mathrm{mg/cm^2})}{DCX(\mathrm{mg/cm^2})} \times \frac{1}{7} \times \frac{1}{\varepsilon} \ .$$

Normalization to the absolute number of incident pions is explicitly included through the factors Y_H (fitted π^+ scattering yield from hydrogen), σ_H (predicted scattering yield from phase shifts), and G (converting center-of-mass σ to lab frame of Y). The difference in the number of scattering centers between the normalization CH_2

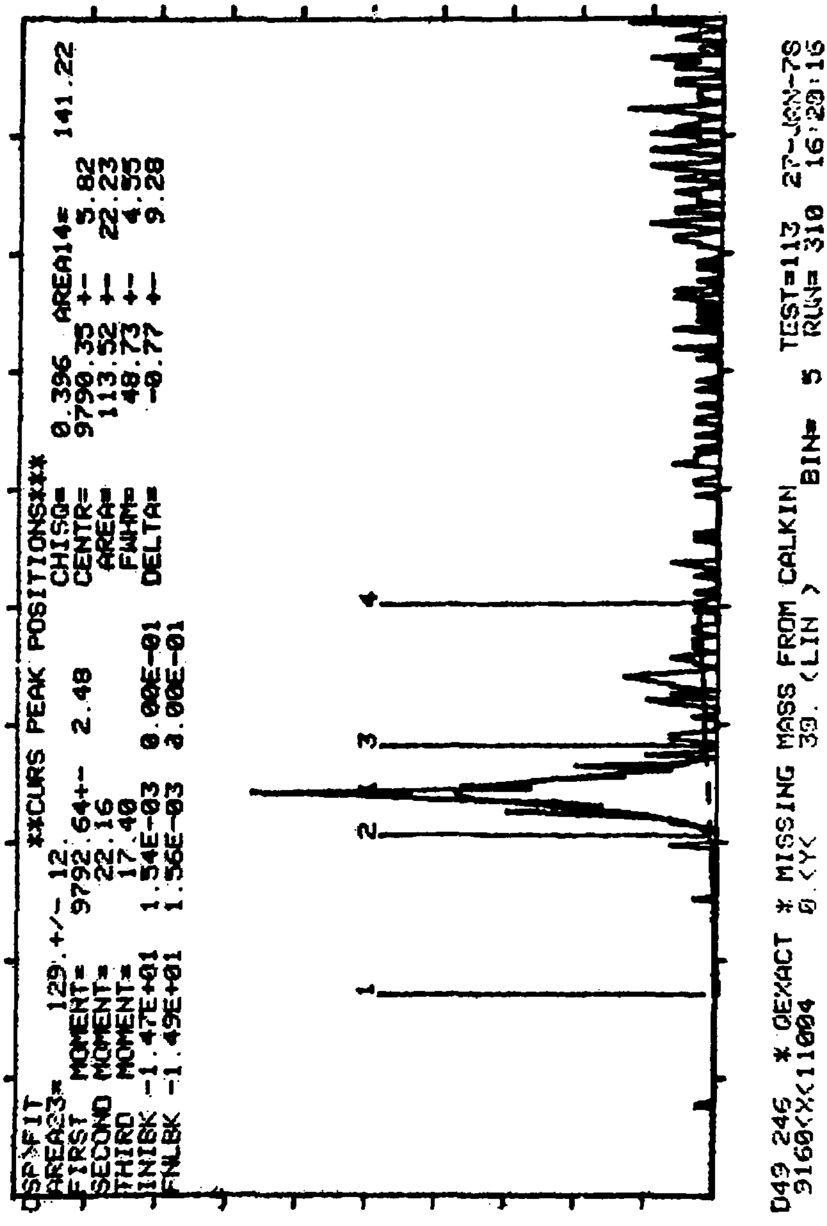

```
DSPKFIT            **CURS PEAK POSITIONS**
AREA23=     129. +/- 12.          CHISQ=  0.396  AREA14=   141.22
FIRST  MOMENT=  9792.64+-  2.48   CENTR= 9790.35 +-   5.82
SECOND MOMENT=    22.16             AREA=  113.52 +-  22.23
THIRD  MOMENT=    17.40             FWHM=   48.73 +-   4.55
INIBK -1.47E+01  1.54E-03  0.00E-01 DELTA=  -0.77 +-   9.28
FNLBK -1.49E+01  1.56E-03  0.00E-01
D49 246  * QEXACT * MISSING MASS FROM CALKIN        TEST=113  27-JAN-78
9160<X<11004    0.<Y<    39. (LIN )    BIN=  5  RUN= 310  16:20:16
```

FIGURE 2-13. Typical fit to a DCX spectrum using PEKFIT.

hydrogen target and the DCX target is accounted for by the relation of areal densities (the bracketed quantity) and the fractional weight of the H and DCX nuclei in the target molecular structure; $1/7=2/14$ which is the fractional weight of H in CH_2, and ε is the fraction of DCX nuclei. The cross-section data appear in the following chapter.

III. EXPERIMENTAL RESULTS

The cross-section data of the various measurements (angular distributions, energy excitation functions, A-dependence) are presented here with a preliminary discussion of the relevant features. The error bars of each point represent only the counting statistics of the DCX peak fitting. The uncertainties arising from counting statistics of the hydrogen normalizations are <1% and are therefore negligible in comparison to the much larger statistical errors in the DCX measurements. The relative error in the phase-shift-predicted cross sections is at the few percent level, also negligible in relation to the DCX statistics. There are also errors associated with variations in target thickness across the beam area; micrometer measurements across the ice targets (most subject to variation) revealed effects of ±5/1000 in thickness. All error sources, excepting the DCX statistics, are estimated to be small and have at most a combined 10% effect on the measurements reported below.

1. Energy Excitation Functions

The variation of cross section as a function of incident pion energy is a necessary piece of information for understanding the reaction mechanism. These measurements were made for the DIAS transitions from the $T=1$ nuclei ^{18}O and ^{26}Mg, and for the non-DIAS transitions from the $T=0$ nuclei ^{16}O and ^{24}Mg. The final states are all ground states of the residual nuclei, e.g.

$$^{16,18}O\ ^{24,26}Mg(\pi^+,\pi^-)^{16,18}Ne\ ^{24,26}Si\ (g.s.)\quad .$$

Also, the excitation of the 2_1^+ (1.89 MeV) first-excited state in ^{18}Ne was observed, though with poor statistics. The energy step size was chosen to adequately exhibit the gross features of the excitation functions. The varying completeness of the ^{16}O, ^{24,26}Mg data, compared to ^{18}O, show the need to determine the gross behaviors in relation to the limited EPICS beam time allocated for these experiments. All excitation functions were measured at 5° laboratory angle for maximum yield.

A. DIAS Excitation Functions

The $^{18}O(\pi^+,\pi^-)^{18}Ne$ (g.s., DIAS) transition has been the most widely investigated, both experimentally (Appendix II) and theoretically (Appendix I), of the DCX reactions. The excitation function of the reaction is shown in Figure 3-1. Three important features are apparent in the 80 to 310-MeV excitation range: there is a maximum in the cross section near 120 MeV, the cross section falls into a wide dip across the peak of the (3,3) resonance centered at 180 MeV, and there is a continuous smooth rise in cross section above the resonance region. The cross section is ~1.8 μb/sr at 120 MeV, down to ~0.9 μb/sr at 180 MeV, and up again to ~2.4 μb/sr at 292 MeV. This behavior was not anticipated by the scant amount of previous data, nor by any preceeding theory as shown in Figure 1-3.

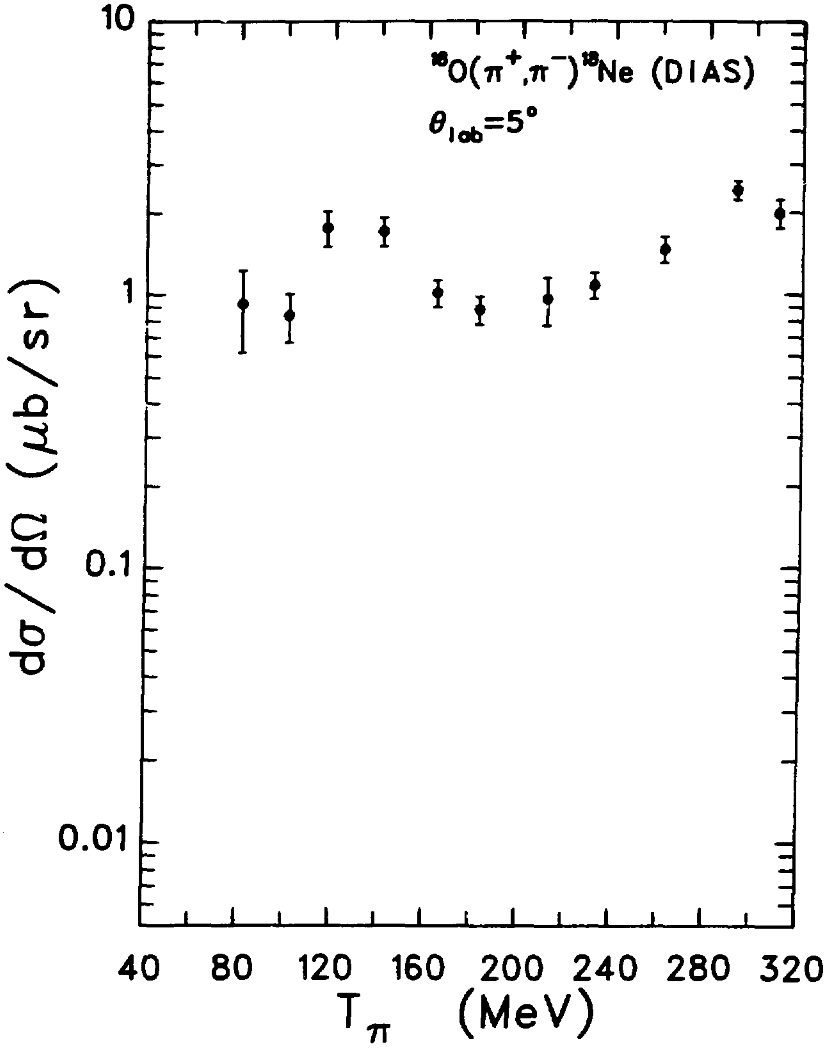

FIGURE 3-1. Energy excitation function of the differential cross section for the reaction $^{18}O(\pi^+,\pi^-)^{18}Ne$ (g.s., DIAS) at a laboratory scattering angle of 5°.

The corresponding DIAS excitation function for the $^{26}Mg \to {}^{26}Si$ reaction is given in Figure 3-2. While less complete than that for $^{18}O \to {}^{18}Ne$, it is very similar. The cross section is in a minimum at 180 MeV, climbing toward both lower and higher energies. Within the limit of error, the two DIAS excitation functions are nearly identical, differing only by an energy independent scale factor.

B. Non-DIAS Excitation Functions

With the idea that the T=1 nuclei above might be described as T=0 structures plus two valence neutrons, excitation functions for the T=0 isotopic members were also examined. Figure 3-3 shows the $^{16}O \to {}^{16}Ne$ (g.s.) excitation function. In contrast to the ^{18}O function, that for ^{16}O has a maximum near 140 MeV which then falls across the resonance region, only levelling off at higher energies. The ratio of $\sigma(^{18}O)/\sigma(^{16}O)$ is ~3 at 164 MeV, and nearly 20 at 292 MeV.

The behavior of the excitation of the transition $^{24}Mg \to {}^{24}Si$ (g.s.), shown in Figure 3-4, is similar to that for $^{16}O \to {}^{16}Ne$. The maximum is again below the resonance, though the fall off is more extreme than for ^{16}O; the ratio $\sigma(^{26}Mg)/(^{24}Mg)$ is nearly 1 at 140 MeV and 70 at 292 MeV.

The 2_1^+ (1.89-MeV) first excited state of ^{18}Ne was poorly discerned because in most cases the runs were run-time limited to the observation of the DIAS. Figure 3-5 shows the clearest such observation. The data (Figure 3-6) seem to show a deep minimum centered about 180 MeV with cross sections on the order of 20 nb/sr,

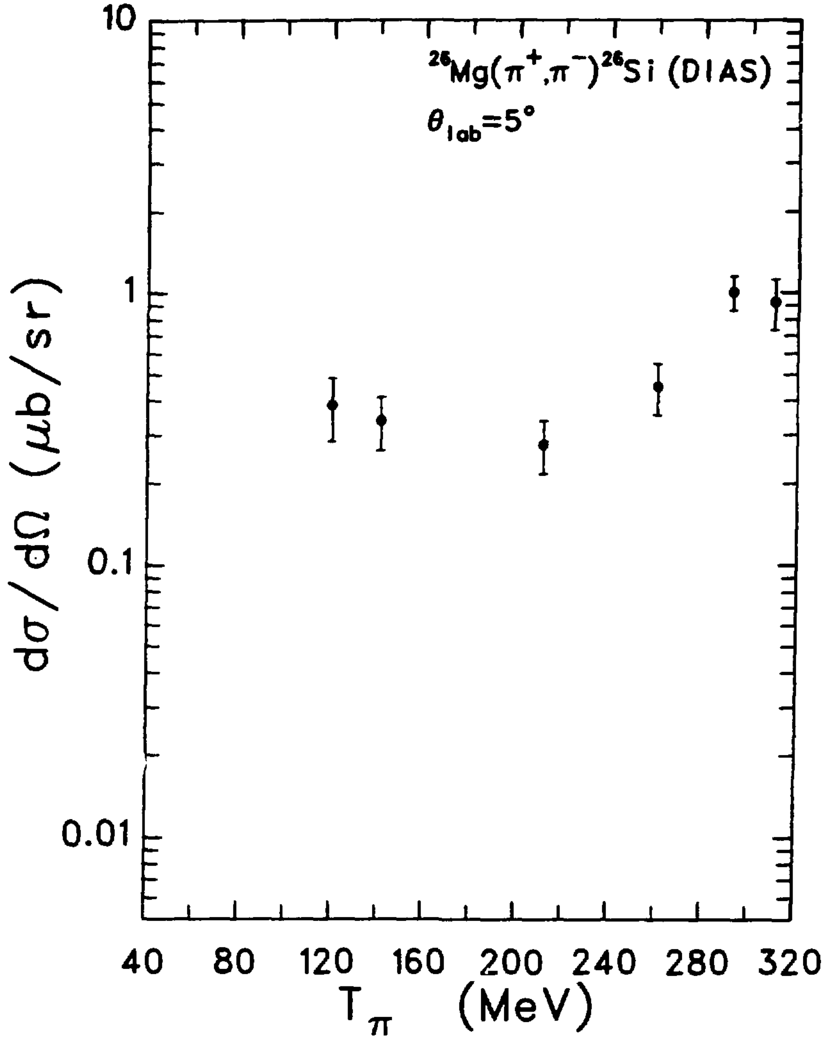

FIGURE 3-2. Energy excitation function of the differential cross section for the reaction ^{26}Mg(π^+,π^-)^{26}Si (g.s., DIAS) at a laboratory scattering angle of 5°.

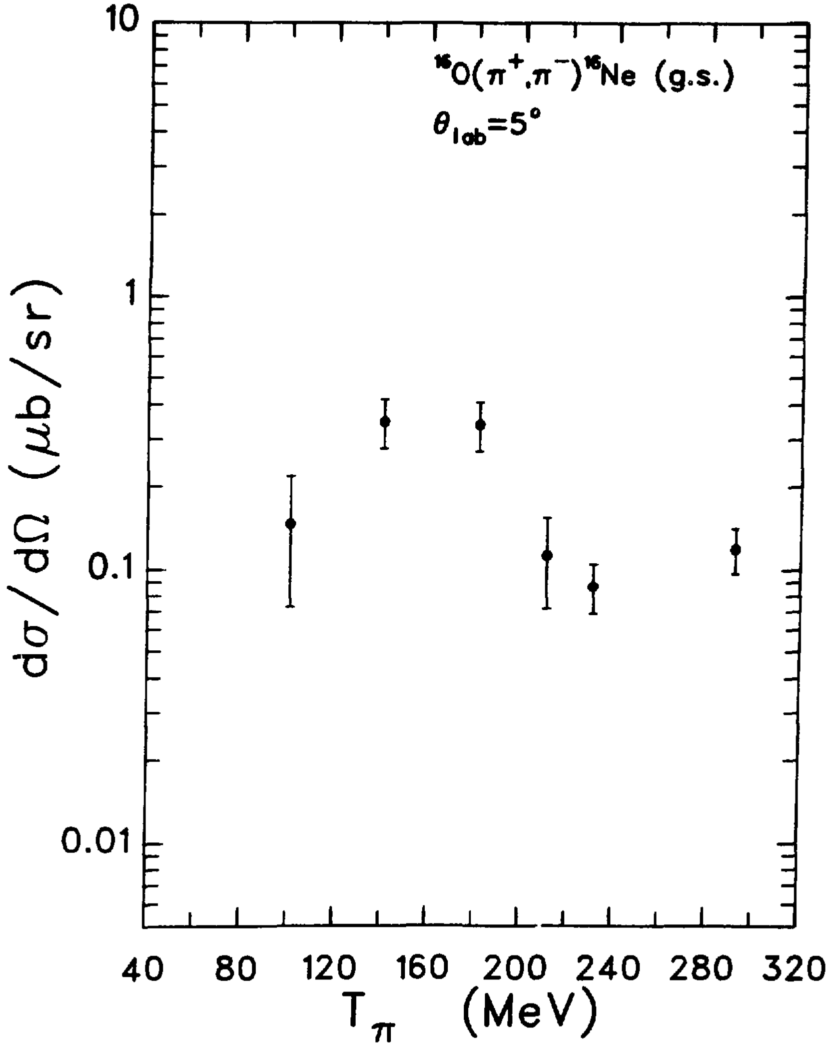

FIGURE 3-3. Energy excitation function of the differential cross section for the reaction $^{16}O(\pi^+,\pi^-)^{16}Ne$ (g.s.) at a laboratory scattering angle of 5°.

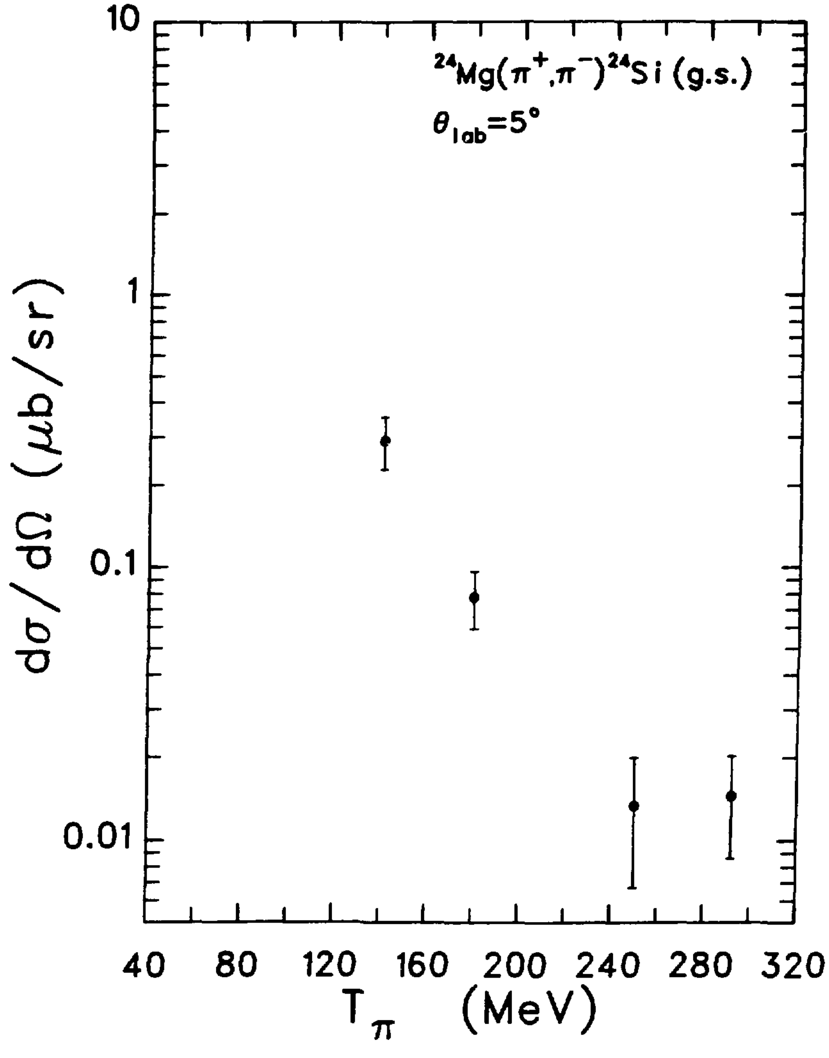

FIGURE 3-4. Energy excitation function of the differential cross section for the reaction $^{24}Mg(\pi^+,\pi^-)^{24}Si$ (g.s.) at a laboratory scattering angle of 5°.

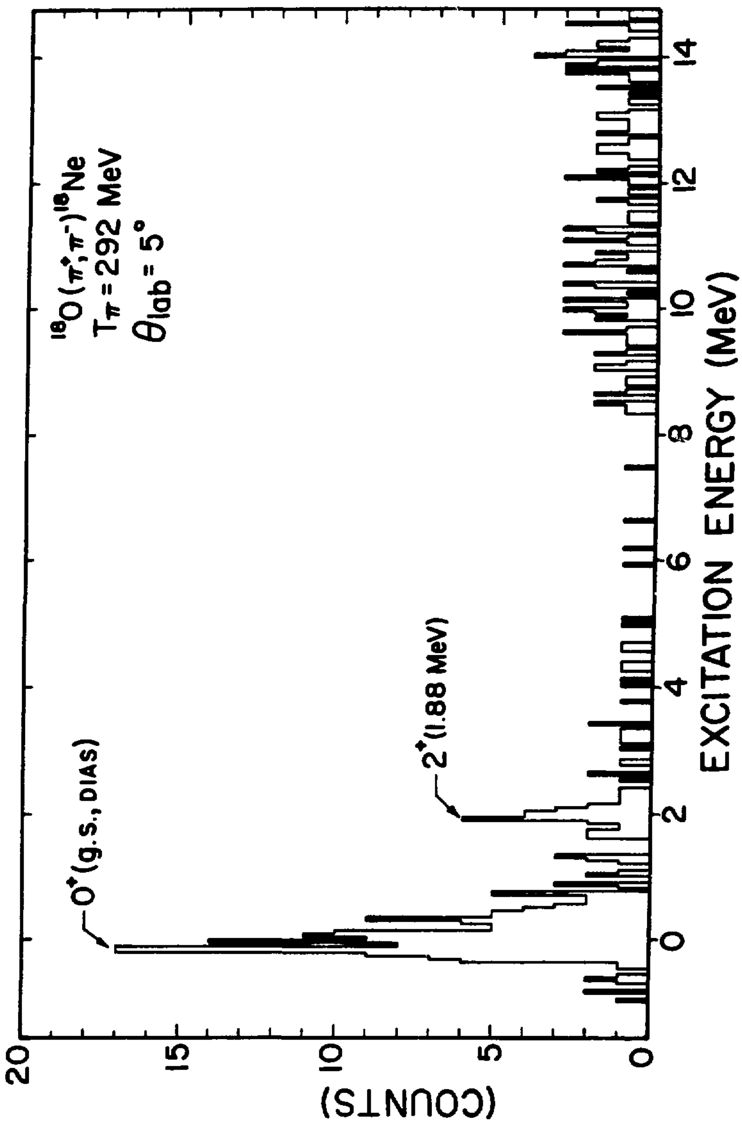

FIGURE 3-5. Excitation spectrum of the ^{18}Ne residual nucleus from the reaction $^{18}O(\pi^+,\pi^-)^{18}Ne$ at 292 MeV.

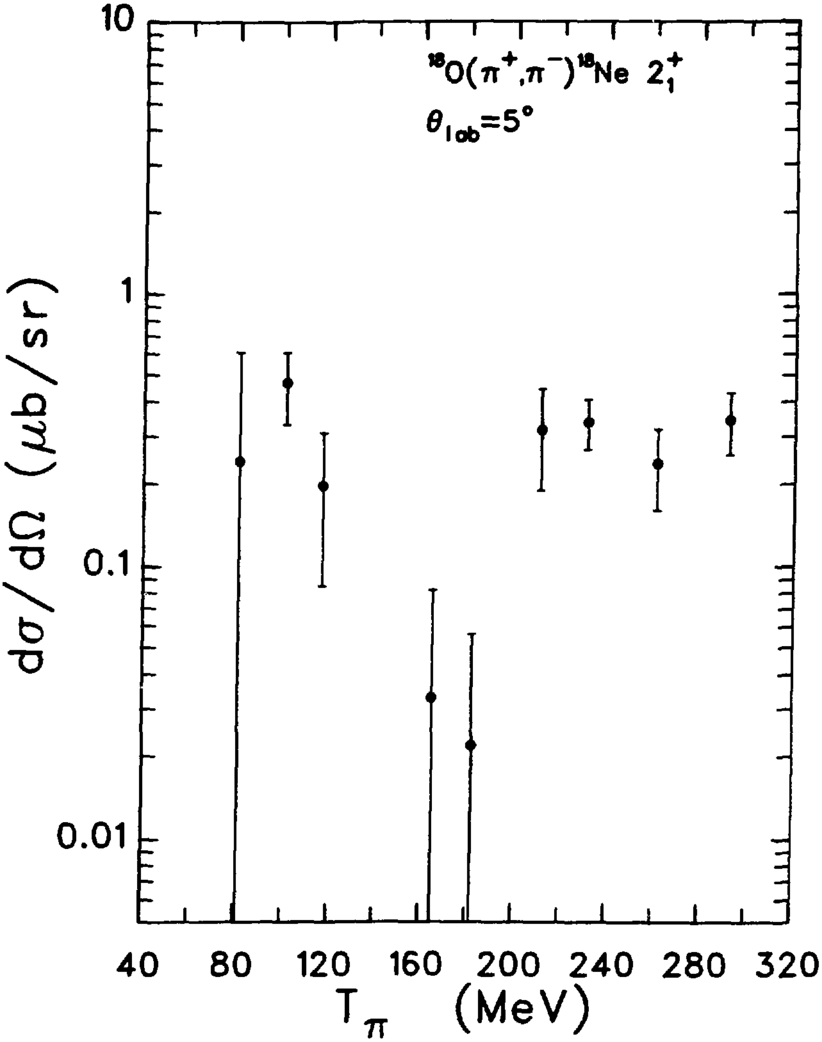

FIGURE 3-6. Energy excitation function of the differential cross section for the reaction $^{18}O(\pi^+,\pi^-)^{18}Ne$ (2_1^+, 1.89 MeV) at a laboratory scattering angle of 5°.

climbing sharply toward lower and higher energies with cross sections in the ~300 nb/sr range. This behavior, while not resembling in detail either the DIAS or non-DIAS functions above, is reminiscent of the DIAS in having a minimum across the energy peak of the (3,3) resonance.

2. Angular Distributions

Two angular distributions for DCX reactions were known prior to these experiments, from targets of ^{18}O and ^{9}Be, both at 164 MeV (Appendix II). Neither distribution could be explained in terms of the diffractive scattering of a strongly-absorbed probe; the minima of the distributions were at too small an angle. The ^{9}Be distribution might be explainable as an interference of $\ell=0$ and $\ell=2$ transitions between the initial and final states. The ^{18}O distribution cannot be so explained.

It has been found that elastic pion scattering near this energy region may be well described as the diffractive scattering of the strongly absorbed pion from the 1/10 nuclear density point of a nucleus, where the density $\rho=\rho(r)$ and $r=R$ is the strong-absorption radius. The semiclassical model of Johnson [Jo-79] for DCX reactions yields a prescription for the angular scattering pattern, based on a strong-absorption nuclear radius:

$$\sigma_{DCX} \propto (N-Z)(N-Z-1)A^{-10/3}\left[J_0(qR)-\frac{a}{R}[J_0(qR)-qRJ_1(qR)]\right]^2 \quad . \qquad 3\text{-}1$$

Here, N and Z are the neutron and proton numbers, A=N+Z is the nucleon number, R is the characteristic strong-absorption radius, and q is the momentum transfer.

The value of R in this expression which places the minimum at the correct location (~21°) is ~5.7 fm, whereas it is known from electron scattering [Si-70] that the 1/10 density point of ^{18}O is about 3.7 fm. The electron scattering value of ~3.7 fm in the above expression yields a minimum near 34° which is clearly in disagreement with the data.

The ^{18}O 164-MeV angular distribution had been puzzling, so the present experiment verified the observation. The relatively large 5° cross sections observed at 292 MeV for both ^{18}O and ^{26}Mg led us to examine the angular distribution of each at this energy well above the resonance region.

A. $^{18}O \rightarrow ^{18}Ne$ Angular Distributions

Three angular distributions for transitions from ^{18}O are presented: distributions of the DIAS transitions at 164 and 292 MeV, and a 164-MeV distribution of the 2_1^+ state.

The 164-MeV distribution of the DIAS, shown in Figure 3-7, covers the range 5°-33° in the laboratory frame. There is a pronounced minimum near 21°, in what initially appears to be a strongly-diffractive pattern. The small-angle peak of the cross section is about 1 μb/sr, falling to ~40 nb/sr near 21°, and then rising to ~250 nb/sr at 33°.

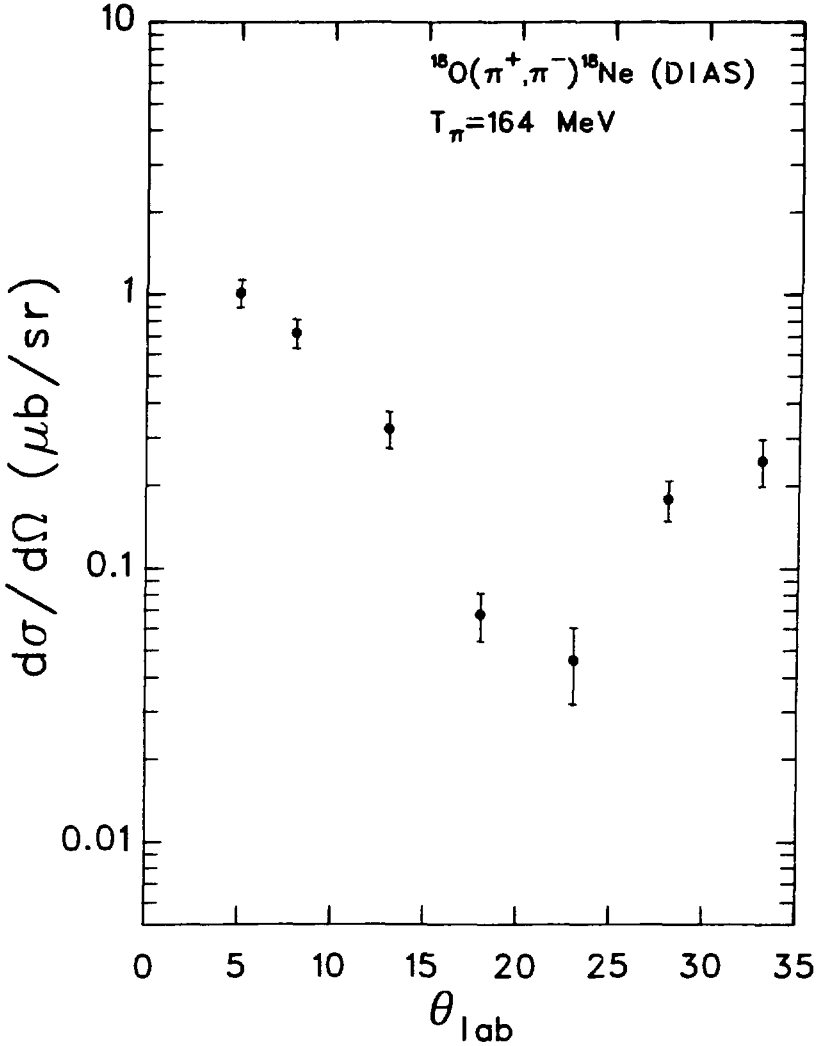

FIGURE 3-7. Angular distribution of the differential cross section for the reaction $^{18}O(\pi^+,\pi^-)^{18}Ne$ (g.s., DIAS) at an incident laboratory pion energy of 164 MeV.

Figure 3-8 shows the corresponding 292-MeV distribution from ^{18}O. The angle of the minimum, while less distinct, appears to be at nearly the same or slightly larger (~25°) value. Its small-angle peak cross section is ~2 μb/sr at 5°, falling to ~60 nb/sr near 25°, climbing back to ~100 nb/sr at 33°.

Again, the 2_1^+ state was sufficiently visible, at times larger than the ground state, to determine its 164-MeV angular distribution. As shown in Figure 3-9, it seems to peak near 25°. It has been claimed that the shape resembles that expected for an ℓ=2 transition [Se-79].

B. $^{26}Mg \rightarrow ^{26}Si$ DIAS Angular Distribution

Only a 292-MeV angular distribution was obtained for the $^{26}Mg \rightarrow ^{26}Si$ transition, due to time constraints. The distribution of this DIAS transition appears in Figure 3-10. The location of the minimum is indistinct but appears to be in the range of 25°-27°. At small angles the peak cross section is ~1 μb/sr, falling off to ~10 nb/sr at the minimum, and rising to ~100 nb/sr at 33°. Within the limit of the errors, this 292-MeV distribution is of identical shape to the corresponding ^{18}O 292-MeV distribution, differing only in scale.

3. A-Dependence

Cross sections at 5° from targets of ^{9}Be, $^{12,13}C$, $^{16,18}O$, $^{24,26}Mg$, ^{32}S, and ^{209}Bi have been determined at either 180 MeV or 292 MeV. The transitions from ^{18}O, ^{26}Mg, and ^{209}Bi are to the DIAS,

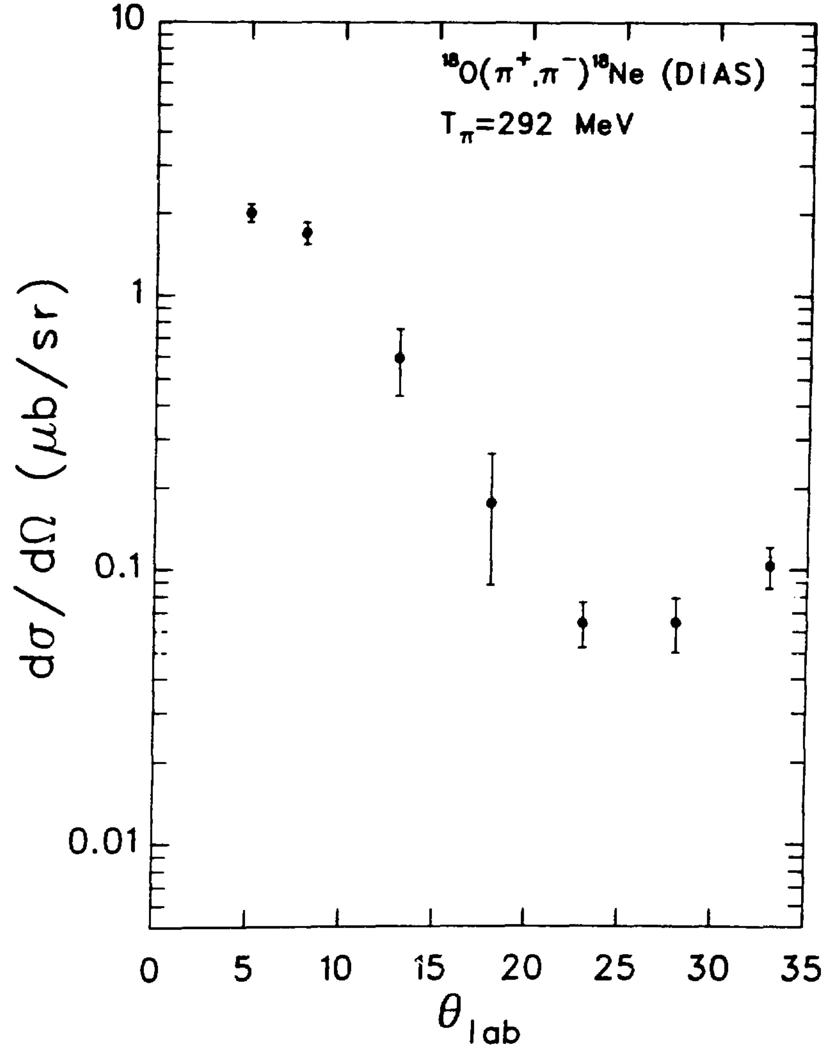

FIGURE 3-8. Angular distribution of the differential cross section for the reaction $^{18}O(\pi^+,\pi^-)^{18}Ne$ (g.s., DIAS) at an incident laboratory pion energy of 292 meV.

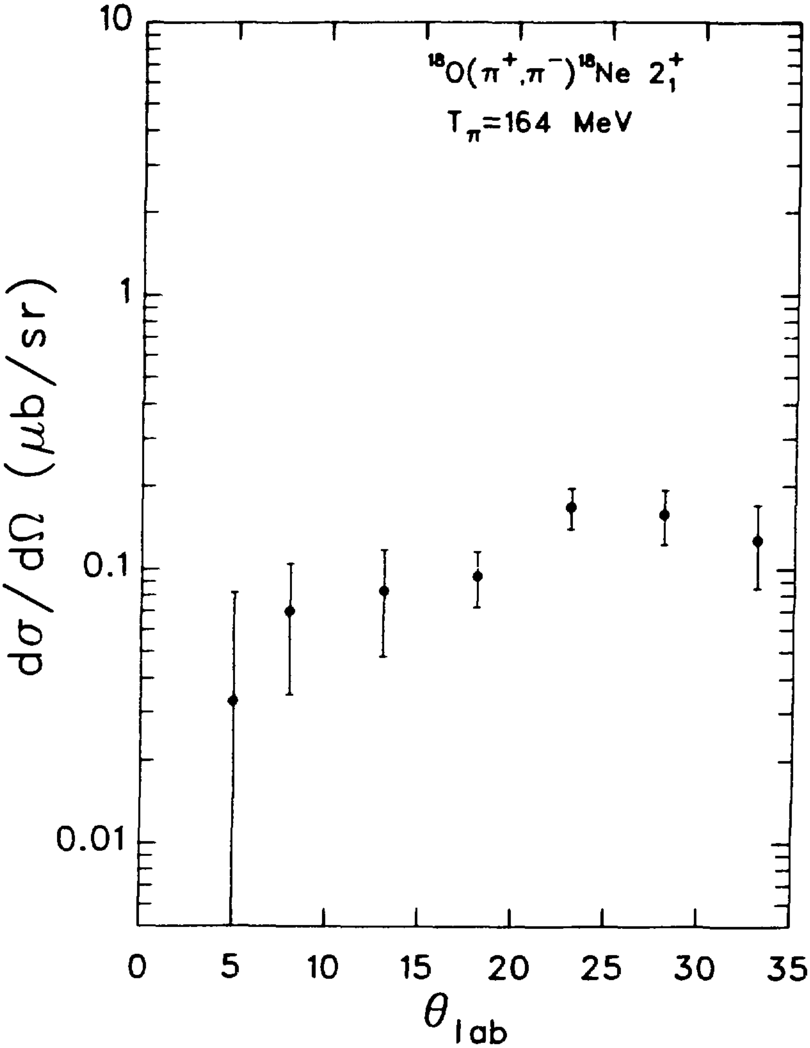

FIGURE 3-9. Angular distribution of the differential cross section for the reaction $^{18}O(\pi^+,\pi^-)^{18}Ne$ (2_1^+, 1.89 MeV) at an incident laboratory pion energy of 164 MeV.

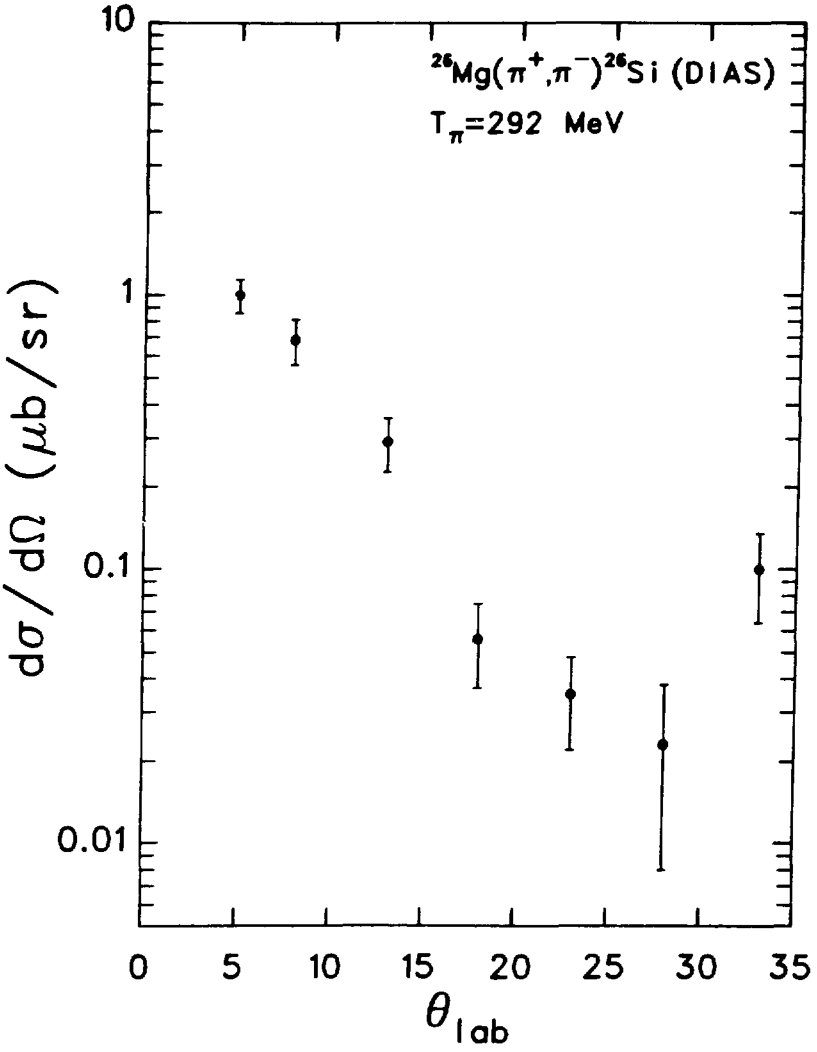

FIGURE 3-10. Angular distribution of the differential cross section for the reaction $^{26}Mg(\pi^+,\pi^-)^{26}Si$ (g.s., DIAS) at an incident laboratory pion energy of 292 MeV.

the others are non-DIAS ground-state transitions. The cross sections are tabulated in Table 2-3 (see p.43).

A plot of the 180-MeV cross sections is shown in Figure 3-11. Preliminary indications over this limited A-range seem to separate the data into three classes, identified as N=Z+2 (DIAS), N=Z, and N=Z+1. The solid line through the DIAS points is the $A^{-10/3}$ scaling of Eq. 3-1, normalized to the ^{18}O point. The other curves are roughly parallel to the solid curve and lower in magnitude.

Only DIAS data exist at 292 MeV, from targets of ^{18}O, ^{26}Mg, and ^{209}Bi. The log-log plot of Figure 3-12 shows that it is possible to make a fair fit to the data with an $A^{-10/3}$ function, again normalizing to the ^{18}O point. This is, of course, insufficient data from which to draw compelling conclusions; there is a notable gap in the data set, consisting of the entire medium-mass section of nuclei.

A discussion of the $^{209}Bi(\pi^+,\pi^-)^{209}At$ (DIAS) cross section is given in Appendix V.

4. Mass Measurements

The DCX reaction was used during the course of these experiments to measure the ground-state masses of ^{12}O, ^{16}Ne, ^{24}Si, and ^{32}Ar. The ^{12}O and ^{16}Ne data were re-measurements, improving the error limit of previous work [Ke-78]. The masses of ^{24}Si and ^{32}Ar are the first reported measurements of these nuclei. These measurements are discussed in detail in Appendix III.

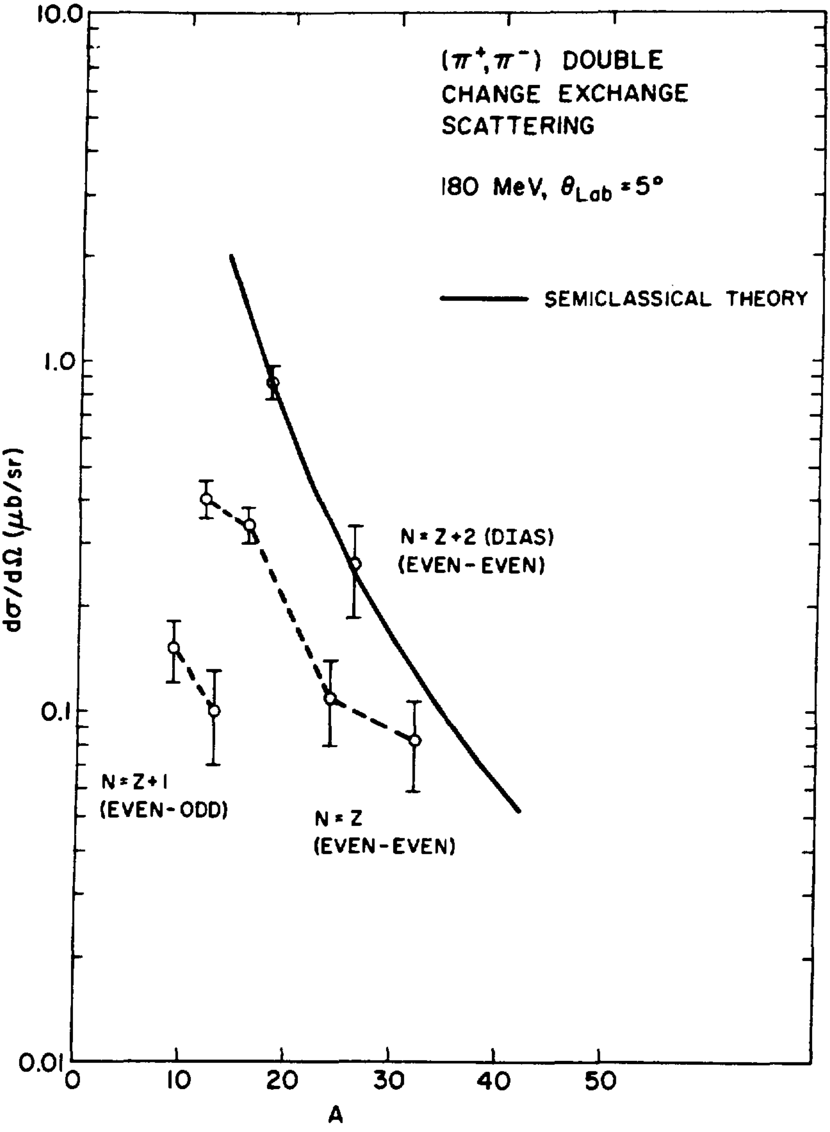

FIGURE 3-11. Differential cross sections at 5° and 180 MeV from (π^+,π^-) reactions on targets of ^{9}Be, ^{12,13}C, ^{16,18}O, ^{24,26}Mg, and ^{32}S. The solid curve is a function of $A^{-10/3}$, normalized to the ^{18}O point.

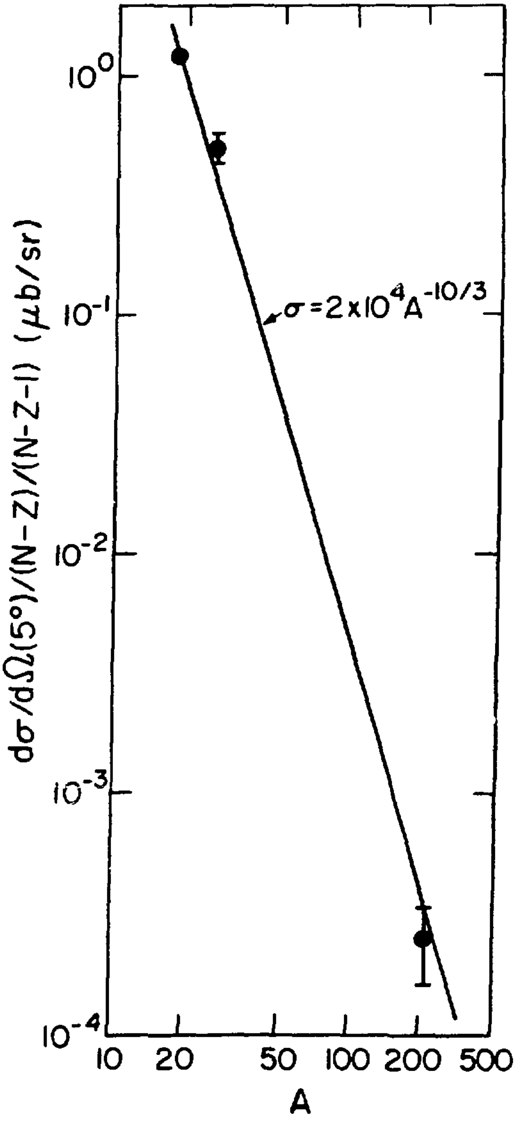

FIGURE 3-12. Differential cross sections at 5° and 292 MeV from (π^+,π^-) reactions on targets of ^{18}O, ^{26}Mg, and ^{209}Bi. The solid line is an $A^{-10/3}$ function, normalized to ^{18}O.

IV. DISCUSSION

We now have a small basis for the discussion of DCX reactions. We know something of their energy dependence, angular behavior, and A-dependence. It is possible to draw some general, simple conclusions from the patterns observed in the data. The need for detailed calculations is also apparent; explanations of the data must be related to the π-nucleus interaction with its dependence on the π-N interaction and nuclear structure. For instance, any model or description seeking to explain the DCX data should also be capable of explaining the elastic-scattering data as well. Current optical-model-type calculations [Co-80] are capable of dealing very well with a wide range of elastic-scattering data, yet are either inappropriate for, or unsuccessful in, explaining the features of DCX.

The following is a discussion of the basic features exhibited in the data. At this point it is a qualitative interpretation of the data, providing more questions than answers. The solutions to these questions are not readily apparent. Part of the solution is in the acquisition and comparison of additional data. Another part is in the development of a phenomenology capable of dealing with a large body of DCX data, simultaneously encompassing a description of other pion-scattering reactions. Additional data needed to complement the existing data set will be pointed out in this chapter.

1. General Observations

A. Energy Excitation Functions

The excitation functions of the two T=0,1 isospin (and isotopic) pairs present a definite pattern. The DIAS and non-DIAS functions of each pair are nearly equal in magnitude at some point below the resonance, and the DIAS rapidly becomes greater than the non-DIAS with increasing energy above the resonance. Figures 4-1 and 4-2 show the paired functions for ^{16,18}O and ^{24,26}Mg, respectively.

Besides this similarity of difference between the two pairs, there is the high degree of similarity between the two DIAS excitation functions, and the somewhat lesser degree of similarity between the two non-DIAS, ground-state excitation functions. This similarity is in the shape of the functions. Regardless of magnitude, the DIAS excitation functions, within the limit of the error bars, are very similar across the range of energy for both T=1 nuclei (Figure 4-3). The non-DIAS excitations, while showing generally similar behavior, exhibit a greater difference in detail between the two; that for ^{24}Mg has a greater fall than the one for ^{16}O (Figure 4-4).

The similarity of the DIAS excitations from these different nuclei indicates that the reaction mechanism effects dominate, through the interaction with the valence neutrons, over nuclear structure effects. The lack of valence neutrons, as in the case of ^{16}O and ^{24}Mg, allows a greater degree of variability between the two

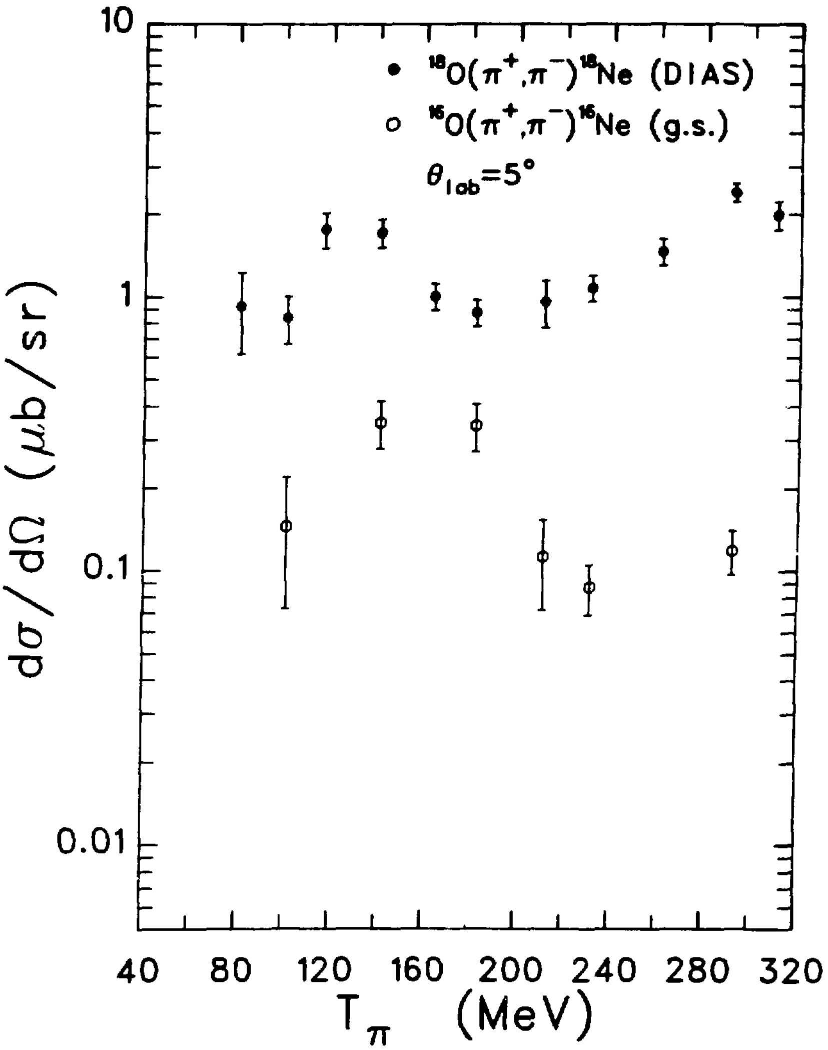

FIGURE 4-1. Comparison of energy excitation functions of the differential cross section for the reactions $^{16,18}O(\pi^+,\pi^-)^{16,18}Ne$ (g.s.) at a laboratory scattering angle of 5°.

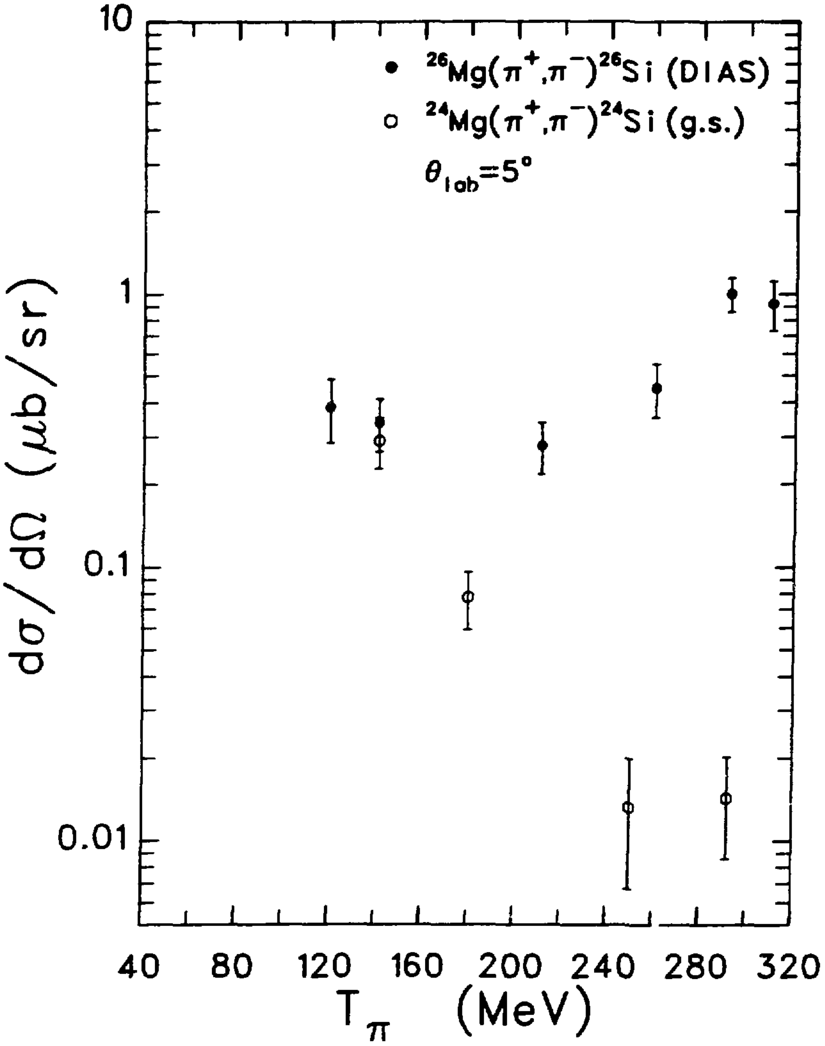

FIGURE 4-2. Comparison of energy excitation functions of the differential cross section for the reactions ^{24,26}Mg(π^+,π^-)^{24,26}Si (g.s.) at a laboratory scattering angle of 5°.

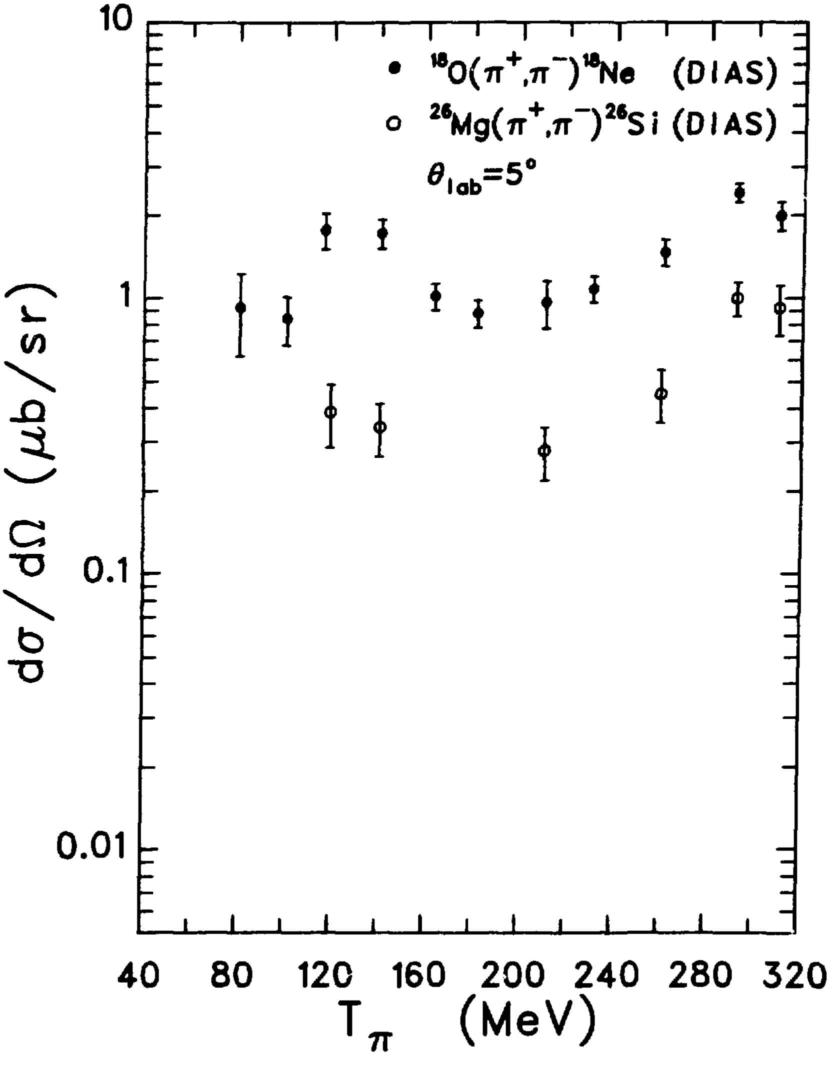

FIGURE 4-3. Comparison of energy excitation functions for the DIAS from (π^+,π^-) on ^{18}O and ^{26}Mg.

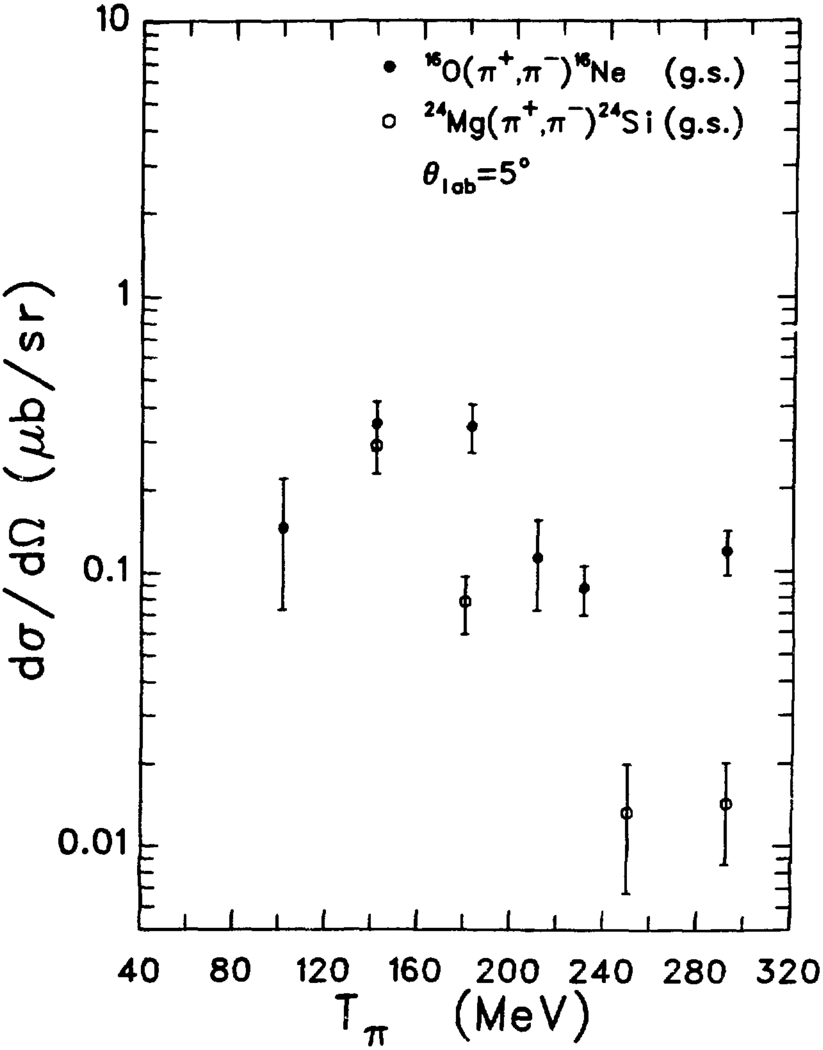

FIGURE 4-4. Comparison of energy excitation functions for the (g.s.) non-DIAS from (π^+,π^-) on ^{16}O and ^{24}Mg.

functions, perhaps indicating an increased role for nuclear structure.

B. Angular Distributions

The angular distributions present an interesting puzzle. At 292 MeV, the minima of the two DIAS distributions appear to be at nearly the same angle — an angle which is larger than that of the ^{18}O minimum at 164 MeV. At 292 MeV, both of the DIAS angular distributions exhibit shallow, indistinct minima. The form of Eq. 3-1 (page 59) was not designed to be valid in this energy region [Jo-80], but it predicts the first minima of the diffractive pattern to be near the observed angles, when given appropriate nuclear radii R.

Diffractive patterns for the scattering of strongly-absorbed probes are characterized by a strong-absorption radius which is dependent on the kinetic energy of the incident particle [Jo-78]. A preliminary analysis of π^+ elastic scattering from calcium isotopes [Mo-81] has shown that this radius near 164 MeV corresponds roughly to the 1/10 nuclear density point, and at 292 MeV is nearly the 3/10 nuclear density point. The 3/10 density-point radii of ^{18}O and ^{26}Mg, determined by electron scattering [Si-70], are about 3.2 f and 3.5 f, respectively. Placing the ^{18}O minimum near 25°, and the ^{26}Mg minimum near 27°, requires R-values in Eq. 3-1 of 3.1 f and 3.3 f, respectively, which are in good agreement with the above values.

C. ^{18}Ne (2^+_1, 1.89 MeV) Excited State

It is interesting to note that the excitation function of the ^{18}Ne 2^+_1 state more closely resembles the pattern of a DIAS than that of a non-DIAS. The ^{18}Ne 2^+_1 is the double analog of the ^{18}O 2^+_1, but, using the concepts developed in Appendix IV, it is a non-DIAT because it is not the initial and final states which are analogs, rather they are intermediate and final states.

The angular distribution may have the basic shape of an ℓ=2 transition, though the data are not sufficiently precise to be sure. This angular distribution is at the same energy (164 MeV) as the DIAS from ^{18}O which was found to have an anomalous minimum. Possible interference effects, as discussed in Appendix IV, may also be contributing to the shape of this distribution.

D. A-Dependence

The scant amount of data collected at two energies for 5° scattering from various nuclei allow us to draw only tentative conclusions as to the A- (or N or Z) dependence of DCX reactions.

At 180-MeV incident energy, the data are shown in Figure 3-11. The target nuclei fall into three families, N=Z+2, N=Z, and N=Z+1. Transitions from the N=Z+2 nuclei are to DIAS, and transitions from the others are to non-DIAS. (The ^{26}Mg point is interpolated from the excitation-function data). The dotted curves connect the members of the two non-DIAS families. The solid line through the DIAS data is from Eq. 3-1, normalized to the ^{18}O point.

Over this limited range of A, the $A^{-10/3}$ dependence of DCX reactions to the DIAS appears to be a good description. With such a small range, and N-Z=2, it is not yet possible to extract separate N and Z dependencies. A similar study over an isotopic chain (e.g. ^{40,42,44,48}Ca) would be a significant contribution to explicating this dependence. It is interesting to note that, within the errors of this limited data set, that the non-DIAS curves are roughly parallel to the DIAS curve. We do not yet know whether this is fortuitous or caused by something more fundamental.

Three DIAS points exist at 292 MeV, from DCX on targets of ^{18}O, ^{26}Mg, and ^{209}Bi. The ^{18}O and ^{26}Mg are T=1, and the ^{209}Bi is T=43/2. As shown in Figure 3-12, an $A^{-10/3}$ curve, normalized to ^{18}O, is a fair representation of the trend in the data; the curve fits the available data over four orders of magnitude. Note, however, the current data represent only the extremes of the periodic table, and the entire center span of this bridge between those extremes is unsupported by data. It is highly likely that variations from $A^{-10/3}$ will be seen in this region, creating a need for some type of correction factor (perhaps based on N and Z) in the expression of Eq. 3-1.

E. Exotica

An exotic speculation has been raised in light of the DCX data. The ^{18}O excitation function shows several enhancements, a peak near 120-MeV incident pion energy, and a gradual rise above the resonance region. Are dibaryon resonances (or exotic multi-quark states) contributing to this process [Br-80][Gr-80]?

The two valence neutrons of ^{18}O could be represented as a relative $^1S_0$ (T=1) configuration. The incident p-wave π^+ is absorbed by this pair, creating a relative $^3S_1$ (T=0,1,2) intermediate configuration; which decays to a π^- and two protons in the relative $^1S_0$ (T=1) configuration. Calculations of the three $^3S_1$-state masses indicate that they might possibly be formed at E_π= 154 Mev (T=0), 270 MeV (T=1), and 497 MeV (T=2) [Ro-80]. Because of the nature of quark calculations, and fermi motion and Coulomb interactions in the nucleus, these energies could be expected to shift by some 10's of MeV. Whether this is a dibaryon resonance, a multi-quark state, or a π-NN resonance argument is not clear — hence this line is pursued no further, here.

2. Questions

A general picture of the DCX reaction is beginning to emerge; enough to bring a number of questions to mind, to wit:

1) Is the shape observed in the two DIAS (T=1 target) excitation functions a general feature of all T=1 targets? Is it a general shape for T > 1 targets?

2) Are the features of non-DIAS excitation functions always similar?

3) What is the cause of the anomalous minimum in the ^{18}O 164-MeV angular distribution? Is it a general feature at this energy for the DIAS? What does a non-DIAS angular distribution look like?

4) Are the 292-MeV angular distributions basically diffractive? Are there two, basically diffractive, amplitudes contributing to the DIAS at 164 MeV?

5) Since transitions to the DIAS appear to be reaction-mechanism dominated, can any nuclear-structure information be extracted? Does the same apply to the non-DIAS?

6) Is the A-dependence of the DIAS really (N-Z)(N-Z-1)$A^{-10/3}$? What is the dependence on N-Z? Is the non-DIAS A-dependence similar to that of the DIAS?

7) What are we seeing in excited-state DCX transitions, such as to the 2_1^+ in ^{18}Ne? Does it actually have an ℓ=2 transition shape?

8) Are (π^-,π^+) reactions related to the non-DIAS (π^+,π^-) reactions?

3. Conclusions

Many answers will be found only through additional experimental data and theoretical calculations. The indications from what has been seen are several. The T=1 DIAS excitation functions are similar for ^{18}O and ^{26}Mg. Probably all T=1 DIAS excitation functions exhibit a similar shape. The similarity in the two observed DIAS excitation functions seems to imply that reaction-mechanism effects dominate the DCX reaction to DIAS. This is further reinforced by the similarity of the differences between the two members of the two T=0,1 pairs observed here. If the reaction mechanism does dominate in transitions to the DIAS it may be that excitation functions for DIAS from T>1 nuclei are all similar.

Non-DIAS (g.s.) excitation functions are generally similar in shape, but, in fine detail, seem to show more variation of shape than the corresponding DIAS. This may be an indication of effects attributable to differences in the nuclear structure between the targets. If DIAS transitions are dominated by reaction-mechanism effects, then DCX as a probe of nuclear structure may be limited to the lower cross section non-DIAS transitions.

On the low-energy side of the (3,3) resonance it is not now clear what is to be learned. This is the region where the non-DIAS and DIAS cross sections become similar in magnitude. It is also where the anomalous minimum occurs in the angular distribution of the DIAS from ^{18}O. The cause of this anomaly is currently undetermined. It can certainly not be accounted for within the context of current phenomenological treatment, in turn making it difficult to relate theory to the physical measurements. It is possible that various processes contribute to the DIAS, and are interfering destructively in this energy region. The effect might also be attributed to

Coulomb-nuclear interference and/or the presence of higher-order processes. Analyses in terms of the latter two will be shortly forthcoming [Li-81] [Jo-81].

APPENDIX I

Some DCX Theories

Three different approaches to DCX are pointed out in this section. They are chosen not so much for their accuracy, but rather to demonstrate the wide variety of methods employed, and because they all treat the excitation function for the reaction $^{18}O(\pi^+,\pi^-)^{18}Ne$ (DIAS).

One of the earliest calculations of DCX was performed by Parsons et al., [Pa-65]. Their work was aimed at stimulating experimental studies by showing that:

1) differential cross sections ($d^2\sigma/d\Omega dE$) were of the order 1 - 10 μb/sr near the (3,3) π-N resonance,
2) it should be possible to probe short-range correlations of nucleons in the nucleus.

The reaction is described as

$$\pi^\pm + A(Z) \rightarrow \{\pi^0 + A(Z\pm1)\} \rightarrow \pi^\mp + A(Z\pm2).$$

The Chew-Low theory [Ch-56] is used to describe the propagation of the intermediate (virtual) π^0, extrapolating its scattering amplitude off the mass shell. Specifically, calculations were performed for the reactions:

1) $\pi^- + {}^3He \rightarrow \pi^+ + 3n$,
2) $\pi^+ + {}^{18}O \rightarrow \pi^- + {}^{18}Ne$.

These calculations were of a qualitative nature, as follows from the assumptions and constraints listed below. For simplicity the calculation is limited to the region of the (3,3) π-N resonance, where the (3,3) channel dominates, and all others are ignored. Multiple scattering of order greater than three, as well as distortions of the pion waves, are ignored. An impulse approximation is made for the scattering of plane-wave pions.

The scattering matrix may then be written as:

$$T(\vec{k},\vec{k}_o) = 2\int \frac{d^3\vec{q}\ \omega_q}{(2\pi)^3(q^2-k_o^2-i\epsilon)} \sum_{i\neq j}^{3} [\tilde{t}_i(\vec{k},\vec{q})\tilde{t}_j(\vec{q},\vec{k}_o)], \qquad \text{I-1}$$

where q represents the intermediate pion momentum and $\tilde{t}_i$ is the scattering matrix for the pion with the i-th nucleon. Using the antisymmetry of the initial- and final-state wave functions under the interchange of any two nucleons, the scattering matrices of eqn. I-1 may be written as

$$3[\tilde{t}_3(\vec{k},\vec{q})\tilde{t}_2(\vec{q},\vec{k}_o) + \tilde{t}_2(\vec{k},\vec{q})\tilde{t}_3(\vec{q},\vec{k}_o)]. \qquad \text{I-2}$$

Now, the operator $\tilde{t}(\vec{p},\vec{q})$ is actually the product of a displacement operator times the operator $t(\vec{p},\vec{q})$ of Chew and Low. Using the following coordinate definitions:

$$\vec{r} = \vec{r}_3-\vec{r}_2 \ , \quad \vec{\rho} = \vec{r}_1-\frac{1}{2}(\vec{r}_2+\vec{r}_3) \ , \quad \text{and } \vec{R} = \frac{1}{3}(\vec{r}_1+\vec{r}_2+\vec{r}_3);$$

the product of the t matrices may be written as

$$\tilde{t}_2(\vec{k},\vec{q})\tilde{t}_3(\vec{q},\vec{k}_o) = \exp[i(\vec{k}_o-\vec{k})\cdot(\vec{R}-\vec{\rho}/3)]\exp[i(\vec{k}_o+\vec{k})\cdot(\vec{r}/2)]$$
$$\times \exp[(-i\vec{q}\cdot\vec{r})t_2(\vec{k},\vec{q})t_3(\vec{q},\vec{k}_o)]. \qquad \text{I-3}$$

For the (3,3) channel the Chew-Low t matrices are given by:

$$t(\vec{p},\vec{q}) = -2\pi(\omega_q\omega_p)^{-1/2}\ P_{33}(\vec{p},\vec{q})p^{-3}e^{i\delta(p)}\sin\delta(p). \qquad \text{I-4}$$

The individual π-N phase shifts are evaluated through the parameterization:

$$q^{-3}e^{i\delta(q)}\sin\delta(q) = q^{-3}[\cot\delta(q)-i]^{-1} = (a+bq^2+cq^4-iq^3)^{-1}. \qquad \text{I-5}$$

Integration over the intermediate momentum is then accomplished by expanding the projection and displacement operators in spherical harmonics to yield:

$$\int dq \frac{2q^4 j_n(qr)}{(q^2-k_o^2-ie)(a+bq^2+cq^4-iq^3)}\ ,\quad n=0,2. \qquad \text{I-6}$$

The phase-shift term in the denominator peaks sharply about $q=q_r$, for a given set of the coefficients, and so $j_n(qr)$ was replaced at that point by $j_n(q_r r)$. Defining the width of the resonance as Γ, the remainder of the integral is evaluated for $\mathrm{abs}(k-q_r)$ both much greater and much less than Γ, while for intermediate values of q a graphical interpolation is made.

The above calculations were repeated for triple scattering, the results being expressed as a correction to the double-scattering calculation. Over the momentum range of interest, ($1.1 < k_o < 2.0\ m_\pi c$) this correction added from ~1 to ~8 percent to the double-scattering cross section.

Of particular interest with respect to the present work is the calculation of the DCX reaction $^{18}O(\pi^+,\pi^-)^{18}Ne$ resulting in the transition to the DIAS. A simple shell-model potential with a nuclear wave function separable into relative coordinates is used to describe the initial and final nuclear states. Using an harmonic-oscillator potential, a nuclear wave function of the form

$$|n_1l_1,n_2l_2,\lambda\mu\rangle$$

may be expressed in relative coordinates of the two valence nucleons as:

$$\sum_{nlNL} |nl,NL,\lambda\mu\rangle\langle nl,NL,\lambda|n_1l_1,n_2l_2,\lambda\rangle . \qquad \text{I-7}$$

Here the quantum numbers n and l are associated with the coordinate

$$\vec{r} = \frac{(\vec{r}_1-\vec{r}_2)}{\sqrt{2}} = (r,\theta,\phi) ,$$

and the quantum numbers N and L are associated with the coordinate

$$\vec{R} = \frac{(\vec{r}_1+\vec{r}_2)}{\sqrt{2}} = (R,\Theta,\Phi) .$$

The initial- and final-state nuclear wave functions are then written in terms of single-particle harmonic-oscillator wave functions:

$$|n_1 l_1, n_2 l_2, \lambda\mu\rangle = \sum_{m_1 m_2} \langle l_1 l_2, m_1 m_2 | \lambda\mu\rangle \; Y_{l_1 m_1}(\theta_1,\phi_1) Y_{l_2 m_2}(\theta_2,\phi_2) \times R_{n_1 l_1}(r_1) R_{n_2 l_2}(r_2) \; , \qquad \text{I-8}$$

and

$$|nl, NL, \lambda\mu\rangle = \sum_{mM} \langle lL, mM | \lambda\mu\rangle \times Y_{LM}(\Theta,\Phi) Y_{lm}(\theta,\phi) R_{NL}(R) R_{nl}(r) \; . \qquad \text{I-9}$$

The $R_{nl}(r)$ are normalized harmonic-oscillator wave functions given by

$$R_{nl}(\rho) = \left(\frac{2n}{\Gamma(n+l+3/2)}\right)^{1/2} \rho^l e^{-\rho^2/2} L_n^{l+1/2}(\rho^2) \; . \qquad \text{I-10}$$

The harmonic-oscillator parameter was assumed the same for both ^{18}O and ^{18}Ne ground states.

These wave functions are then used to generate the zero-degree differential cross section ($d\sigma/d\Omega$) over a range of incident-pion momenta ($0.5 < m_\pi c < 2.0$). The results are displayed in Figure 1-3 (see p.13).

A fixed-scatterer approximation was used by Kaufmann et al., [Ka-74] in calculations of single and double charge exchange on light nuclei ($A < 20$) for incident-pion energies near 200 MeV. Multiple scattering to all orders is treated through Gibbs' formulation [Gi-71] of Watson's multiple-scattering equations. Target nuclei included in this study were ^{9}Be, ^{11}B, ^{13}C, and ^{18}O.

The pion-nucleus scattering amplitude is described using a simple, analytic form, the assumption of which eliminates off-shell effects. The elastic scattering of pions off a set of i nucleons at fixed $\vec{r}_i$ is then given by

$$G_i(\vec{k},\vec{k}') = f_i(\vec{k},\vec{k}')e^{i\vec{r}_i\cdot\vec{k}} + \frac{ik}{2\pi}\sum_{j\neq i}\int d\Omega_p f_i(\vec{p},\vec{k}')e^{i\vec{p}\cdot(\vec{r}_i-\vec{r}_j)}$$

$$\times\ \Theta[\vec{p}\cdot(\vec{r}_i-\vec{r}_j)]G_j(\vec{k},\vec{p}) \ . \qquad \text{I-11}$$

The f_i are free pion-nucleon scattering amplitudes. The pion-nucleus scattering amplitude is then

$$F(\vec{k},\vec{k}') = \sum_{i=1}^{A} e^{-i\vec{r}_i\cdot\vec{k}'} G_i(\vec{k},\vec{k}') \ . \qquad \text{I-12}$$

It is assumed here that the initial- and final-state nuclear wave functions are identical, the reactions are elastic or lead only to analog states.

Charge exchange is introduced in the following manner. For an incident π^+ beam, define G_i^+ as the elastic amplitude, and G_i^o, G_i^- as the production amplitudes for π^0 and π^- respectively. Also define the elastic free pion-nucleon amplitudes as f_i^{++} ; f_i^{--}, and f_i^{oo}, with free pion-nucleon single-charge-exchange amplitudes as f_i^{+o}, f_i^{o+}, f_i^{-o}, and f_i^{o-}. The coupled integral equations describing pion-nucleus scattering can then be written as

$$G_\iota^{+} = f_\iota^{++} + f_\iota^{++}\sum_{j\neq\iota} G_j^{+} + f_\iota^{+o}\sum_{j\neq\iota} G_j^{o} \,,$$

$$G_\iota^{o} = f_\iota^{o+} + f_\iota^{oo}\sum_{j\neq\iota} G_j^{o} + f_\iota^{o+}\sum_{j\neq\iota} G_j^{+} + f_\iota^{o-}\sum_{j\neq\iota} G_j^{-} \,, \qquad \text{I-13}$$

$$G_\iota^{-} = 0 + f_\iota^{--}\sum_{j\neq\iota} G_j^{-} + f_\iota^{-o}\sum_{j\neq\iota} g_j^{o} \,.$$

Here, terms like $f_\iota^{++}\Sigma G_j^{+}$ represent a π^+ being scattered out of the nucleus from the ι-th nucleon. Terms like $f_\iota^{-o}\Sigma G_j^{o}$ represent a π^- scattering out of the nucleus, having been charge exchanged from a π^0 at the ι-th (last) scatter. Appropriate combinations of these amplitudes may then be formed to yield single and double charge exchange. The calculations were performed assuming that only the valence nucleon(s) outside the core were charge exchanged upon. The effect of spin-flip in the elementary π-N amplitude was explicitly included for single charge exchange, but not for DCX.

Of particular interest to the current work is the calculation of the DIAS transition from ^{18}O. The 0° cross section (dσ/dΩ) as a function of energy is shown in Figure 1-3. The angular distribution of the DIAS was calculated and reported as 6 μb/sr at 0° and 180 MeV, falling to ~0.3 μb/sr at 30°.

The authors pointed out the following weaknesses in their approach. An inadequate transformation of the π-N amplitudes to the lab frame, the use of unsophisticated wave functions with either Wood-Saxon or harmonic-oscillator densities, and the neglect of Coulomb corrections for small-angle scattering. They conclude with the observation that "charge-exchange data rigidly constrain calculational models and will be sure to provide stimulation and embarrassment for theorists for some time to come."

Over a period of years, a detailed optical-model approach has been developed by G. A. Miller and J. E. Spencer [Mi-74] [Mi-75] [Mi-76][Sp-77]. Their efforts included many of the effects being considered for pion elastic scattering, among them:

1) varying the π-N off-shell t-matrix,
2) including two-nucleon, short-range correlations,
3) different density distributions for neutrons and protons,
4) considerations of the angle transformation.

Two potential forms were used, Kisslinger and local Laplacian. The t matrices used in each case were;

$$\text{Kisslinger:}\quad t_K(\vec{k},\vec{k}') = a + c\vec{k}\cdot\vec{k}' + (b + d\vec{k}\cdot\vec{k}')(\vec{\tau}\cdot\vec{t}) \qquad \text{I-14}$$

and

$$\text{local Laplacian:}\quad t_L(\vec{k},\vec{k}') = a + c(k^2-q^2/2)$$

$$+ (b + d(k^2-q^2/2))(\vec{\tau}\cdot\vec{t}). \qquad \text{I-15}$$

Here, $\vec{\tau}$ and $\vec{t}$ are isospin operators for the pion and nucleon respectively, $\vec{q}=\vec{k}-\vec{k}'$, and a, b, c, and d are energy-dependent s-, and p-wave coefficients depending on the π-N phase shifts.

First-order potentials are then constructed with the following considerations. An impulse approximation is made, which consists of the use of a first-order π-N t matrix and neglect of the momentum distribution of the struck nucleon. This means that the energy at which the π-N T-matrix is evaluated ignores the kinetic energy of the nucleon, and also ignores the momentum of the nucleon in the expression of the relative π-N momentum. This leads to an optical potential, in coordinate space, of the form:

$$2\omega V^K_{\alpha\beta}(r) = \delta_{\alpha\beta}(N+Z)(2\pi)^3[(k/k_c)A\rho_0(r) - (k_c/k)C\vec{\nabla}\rho_0(\vec{r})\vec{\nabla}]$$
$$+ (2\pi)^3(\alpha|\vec{t}_\pi\cdot\vec{T}_N|\beta)[(k/k_c)B\rho_1(r) - (k_c/k)D\vec{\nabla}\rho_1(\vec{r})\nabla] \qquad \text{I-16}$$

for the Kisslinger form, and

$$2\omega V^L_{\alpha\beta}(r) = \delta_{\alpha\beta}(N+Z)(2\pi)^3[((k/k_c)A + kk_cC)\rho_0(r) + (k_c/k)C\nabla^2\rho_0(r)]$$
$$+ (2\pi)^3(\alpha|\vec{t}_\pi\cdot\vec{T}_N|\beta)[((k/k_c)B + kk_cD)\rho_1(r)$$
$$+ (k_c/k)D\nabla^2\rho_1(r)] \qquad \text{I-17}$$

for the Laplacian form.

These potentials are then used in a coupled-channels Klein-Gordon equation:

$$(-\nabla^2 + 2\omega V^\alpha_c - k^2_\alpha)\psi_\alpha = 2\omega\sum_\beta V_{\alpha\beta}\psi_\beta. \qquad \text{I-18}$$

The neutron and proton form factors for the nuclei are explicitly included through the ρ's from the following definitions:

$$F_0(\vec{q}) \equiv \frac{NF^N(\vec{q}) + ZF^Z(\vec{q})}{N + Z} = \int e^{-i\vec{q}\cdot\vec{r}} \rho_0(\vec{r}) d^3r \qquad \text{I-19}$$

and

$$F_1(\vec{q}) \equiv \frac{NF^N(\vec{q}) - ZF^Z(\vec{q})}{N - Z} = \int e^{-i\vec{q}\cdot\vec{r}} \rho_1(\vec{r}) d^3r. \qquad \text{I-20}$$

Here the $\vec{t}_\pi$ and $\vec{T}_N$ are pion and nucleus isospin operators respectively, k_c is the pion momentum, V_c^α is the nuclear-Coulomb potential in the channel α, and α and β represent elastic and charge-exchange channels.

The t matrices for the various processes may be written:

$$\begin{aligned} T_{\text{elastic}} &= \langle \phi_{\pi+} | V_0 | \psi_{\pi-}^{(+)} \rangle \\ T_{SCX} &= \langle \psi_{\pi+}^{(-)} | V_1 | \psi_{\pi-}^{(+)} \rangle \\ T_{DCX} &= \langle \psi_{\pi+}^{(-)} | V_1 G V_1 | \Psi_{\pi-}^{(+)} \rangle . \end{aligned} \qquad \text{I-21}$$

Here V_0 and V_1 are the potentials which produce the elastic- and charge-exchange reactions. Since double-charge-exchange reactions involve at least two nucleons, a second-order potential is developed. The t matrix is redefined in terms of the multiple-scattering series

$$T = \sum_i t_i + \sum_{i \neq j} t_i g t_j + \cdots \quad . \qquad \text{I-22}$$

where the sums are over the individual target nucleons, and the second term on the right is the lowest-order contribution to the DCX reactions.

The basic, second-order coupled-channel optical potential is then written:

$$V_{\alpha\beta} = V^{(1)}_{\alpha\beta} + \sum_n{}' V^{(1)}_{\alpha n} \frac{1}{\varepsilon-\varepsilon_n-k-V_{nn}} V^{(1)}_{n\beta} \quad , \qquad \text{I-23}$$

where $V^{(1)}_{\alpha\beta}$ is the first-order potential, and the sum is over all intermediate states in the transition to the DIAS. Several simplifying assumptions are made; the differences between the neutron and proton densities in both the first-order and excited-state potentials are neglected, the excited-state energy (ε_n) and elastic-scattering potential for the excited state (V_{nn}) are replaced by the average quantities $\overline{\varepsilon}$ and $\overline{V}$. this allows the sum over n to be performed:

$$\begin{aligned}\sum_n{}' V_{\alpha n}(\vec{k},\vec{k}'')V_{n\beta}(\vec{k}'',\vec{k}') = \Big[&(N+Z)^2 t_o(\vec{k},\vec{k}'')t_o(\vec{k}'',\vec{k}')\delta_{\alpha\beta} + \langle\alpha|(\vec{t}_\pi\cdot\vec{T}_N)^2|\beta\rangle \\ &\times t_1(\vec{k},\vec{k}'')t_1(\vec{k}'',\vec{k}') + \langle\alpha|\vec{t}_\pi\cdot\vec{T}_N|\beta\rangle \\ &\times \{t_o(\vec{k},\vec{k}'')t_1(\vec{k}'',\vec{k}') + t_1(\vec{k},\vec{k}'')t_o(\vec{k}'',\vec{k}')\}\Big] \\ &\times \big[\tilde{\rho}^{(2)}(\vec{q}_1,\vec{q}_2) - F(\vec{q}_1)F(\vec{q}_2)\big] \quad . \qquad \text{I-24}\end{aligned}$$

Here, $\vec{q}_1=\vec{k}''-\vec{k}'$ and $\vec{q}_2=\vec{k}'-\vec{k}''$. The quantity $\tilde{\rho}^{(2)}$ is the nuclear-structure part of the wave function $|\Psi\rangle$, and is given by:

$$\tilde{\rho}^{(2)}(\vec{q}_1,\vec{q}_2) = \frac{1}{(N+Z)^2} \sum_{\ell m} \langle \Psi | e^{-iq_1 r_\ell} e^{-iq_2 r_m} | \Psi \rangle , \tag{I-25}$$

which can be rewritten [Fe-71]:

$$\rho^{(2)}(\vec{q}_1,\vec{q}_2) = \frac{1}{(N+Z)(N+Z-1)} \sum_{\ell \neq m} \langle \Psi | e^{-iq_1 r_\ell} e^{-iq_2 r_m} | \Psi \rangle \quad . \tag{I-26}$$

The second-order, coupled-channel optical potential may then be written as

$$\begin{aligned} V_{\alpha\beta}^{(2)}(\vec{k},\vec{k}') = \int d\vec{k}'' \{ & (N+Z)^2 t_o(\vec{k},\vec{k}'') t_o(\vec{k}'',\vec{k}') + (\alpha | (\vec{t}_\pi \cdot \vec{T}_N)^2 | \beta) \\ & \times t_1(\vec{k},\vec{k}'') t_1(\vec{k}'',\vec{k}') + (\alpha | \vec{t}_\pi \cdot \vec{T}_N | \beta) \\ & \times \left(t_o(\vec{k},\vec{k}'') t_1(\vec{k}'',\vec{k}') + t_1(\vec{k},\vec{k}'') t_o(\vec{k}'',\vec{k}') \right) \} \\ & \times C(\vec{q}_1,\vec{q}_2) \langle k'' | (E-\bar{\varepsilon}-k-\bar{V})^{-1} | k'' \rangle \ . \end{aligned} \tag{I-27}$$

This is the same as Eq. I-7, and $C(\vec{q}_1,\vec{q}_2) = \rho^{(2)}(\vec{q}_1,\vec{q}_2) - F(\vec{q}_1)F(\vec{q}_2)$. The C term allows the specification of spatial correlations between nucleons. Approximations are used to solve the integral over the intermediate momentum k".

As before, this has been used for the treatment of $^{18}O(\pi^+,\pi^-)^{18}Ne$, results for which appear in Figure 1-3, and in Appendix IV Figure 1, with different sets of assumptions.

APPENDIX II

Brief History of DCX Experiments

Experimental studies of pion double charge exchange were first undertaken in the mid-1960's. Synchrocyclotron (SC) proton beams were used to generate secondary pion beams with fluxes in the region 10^4-10^5 π/s. Various experiments employing emulsions and electronic counters were reported from the Soviet Union, United States, France, and Switzerland. The accelerators were operating in the realm of High Energy, and the useful pion beams were typically several hundred MeV in energy with a spread on the order of 10 MeV.

The initial (π^+,π^-) experiments involved the observation of "star" formation from π^- capture by nuclei in emulsions exposed to a π^+ beam at the JINR (USSR) SC [Ba-66]. The ionization traces were backtracked to the origin layers (DCX converter), separately composed of ^{12}C, ^{14}N, ^{16}O, Br, and Ag. Total reaction cross sections were examined as a function of pion energy over the range of ~40 to 140 MeV. While showing that DCX occurred, these experiments could provide no information on the relationship of DCX to nuclear structure because no observation of final states were possible. No reaction routes could be determined, leaving open the question of the nature of the reaction mechanism.

The second experiment was the first to employ electronic counter techniques. The CERN SC was used for the measurement of 0° cross sections for (π^+,π^-) from ^7Li, ^9Be, and ^{23}Na [Gi-64]. The incident pion beam energy was T_π=195 MeV, with a width of 30 MeV and a flux of ~5×10^5 π/s. A double mass spectrometer identified outgoing particles with the aid of several DISC Cerenkov counters. Because of poor energy resolution it was not possible to observe discrete final states, but since the energy spread of the π^- beam was similar to that of the incident π^+ beam, shifted by the Q value of the reaction, it was assumed that a two-body final state was involved. The resultant cross sections were:

$$^{7}\mathrm{Li}(\pi^+,\pi^-)^{7}\mathrm{B} \simeq 90 \pm 10\ \mu\mathrm{b/sr}$$
$$^{9}\mathrm{Be}(\pi^+,\pi^-)^{9}\mathrm{C} \simeq 10 \pm 3\ \mu\mathrm{b/sr}$$
$$^{23}\mathrm{Na}(\pi^+,\pi^-)^{23}\mathrm{Al} \simeq 1.4\ (+1.0,\ -0.7)\ \mu\mathrm{b/sr}\ .$$

Also in 1964, a measurement of $d\sigma/d\Omega$ for (π^-,π^+) on copper at 90° was reported [Da-64]. All the data was yet too sparse to explicate the reaction mechanism or the reaction dependence on nuclear properties, save that the cross section decreased with increasing A. It is now known that the CERN cross sections are at least an order of magnitude high for any discrete state.

In 1968 several attempts were made to observe transitions leading to a discrete DIAS. Targets of ^{51}V, ^{90}Zr, and ^{7}Li were bombarded with a π^+ beam at the University of California LRL 184-in SC [Bo-68]. The incident pion energy was varied from 110 to 210 MeV, with a width of 10 MeV and a flux of ~6×10^4 π/s. A C-magnet spectrometer was constructed and instrumented with entrance and exit spark chambers and scintillators. A propane (gas) Cherenkov counter was positioned before the spectrometer to discriminate against electrons. No DIAS transitions were observed at the experimental level of sensitivity.

Another experiment, involving (π^+,π^-) from ^{51}V and ^{7}Li, was reported in the same journal volume [Co-68]. The University of Rochester 140-in SC was used to produce a 31-MeV π^+ beam, with a width of 3.5 MeV and a flux of ~1.5×10^4 π/s. A magnet instrumented with spark chambers, to ray trace particles, identified scattered particles at a laboratory angle of 29°. Two π^- events were identified from each target, though at Q values different than those predicted. Again, no DIAS was observed, and the differential cross sections were lower than predicted [Ko-65] by a factor of ~100.

Most of the electronic detection experiments (except at Rochester) suffered from the inability to unambiguously identify outgoing DCX pions. Particle trajectories (as measured at Rochester) were needed for these very low-count-rate experiments. A later reexamination of the Rochester results [Bu-80] indicates that the several events actually did occur with about the correct Q value, and that a DIAS transition was probably seen in ^{51}V.

The decade of the 60's closed with little reliable information on DCX. The possibilities mentioned by Ericson in 1963 [Er-63] remained only possibilities. One of the great obstacles to all the experiments was the very low incident pion flux. That, combined with low cross sections, conspired to make experimental running time very long with the return of only statistically marginal data (at Rochester they saw ~1 DCX event/week). Any significant studies would require beam intensities several orders of magnitude greater than those produced so far. Further work awaited the development of the dedicated meson facilities of LAMPF and SIN. These new accelerators would provide secondary meson beams with fluxes ~10^8 π/s.

In 1977, the first reports on DCX at LAMPF and SIN appeared. The LAMPF experiment consisted of a survey of 0° cross sections for (π^+,π^-) from various nuclei [Ma-77] [Ho-77] [Bu-78] [Co-79]. The Low Energy Pion channel (LEP) at LAMPF was tuned for pion beams in the range of 95-145 MeV, with a 1% (momentum dispersed) width and flux of ~2×10^7 π/s. Since LEP consists of four bending dipoles for momentum analysis, targets were placed in the middle so that the first two bends could be used to focus a beam on target and the second two bends could act as a 0° spectrometer. The final-state resolving ability was ~0.5 MeV. Discrete two-body final states were observed, both DIAS and non-DIAS. Among the targets were $^{16,18}O$ and $^{24,26}Mg$. A three-point energy excitation function was acquired from ^{18}O, and is in good agreement with the latest results, though too incomplete to indicate the nature of the function as currently observed.

At about the same time as the LEP experiment, the ground-state DIAS in the reaction $^{18}O(\pi^+,\pi^-)^{18}Ne$ was observed at SIN [Pe-77]. The SUSI spectrometer was used to identify scattered particles at 18°. Two incident pion energies were used, 148 and

187 MeV, with fluxes on the order of ~3×10^6 π/s. The cross sections determined were:

147 MeV: $\leq$ 70 nb/sr,

and

187 MeV: ≈120 nb/sr.

The LEP 0°, 139-MeV point was ~2.0 μb/sr, indicating a strong angular dependence for the reaction. The final state resolution, however, was not sufficient to resolve possible contributions from the 2_1^+, first excited state.

The last experiments before those reported here were performed with the EPICS facility at LAMPF [Se-79]. Angular distributions from 13° to ~45° were examined for (π^+,π^-) from ^{18}O and ^{9}Be at 164 MeV. The DIAS and 2_1^+ states were seen in ^{18}Ne. Both the ^{18}Ne (g.s.) and ^{9}Be distributions appear to be non-simply diffractive, though the 2_1^+ in ^{18}Ne was believed to match well an ℓ=2 shape.

By this time, we knew the magnitude of problems to be faced. The sometimes conflicting results could be attributed to known experimental difficulties, and the high-resolution data indicated that the explanations would not be simply arrived at. Careful, systematic investigation was called for.

APPENDIX III

Isospin Quintets in the 1p and s-d Shells

PHYSICAL REVIEW C VOLUME 22, NUMBER 3 SEPTEMBER 1980

Isospin quintets in the 1p and s-d shells

O. R. Burleson, G. S. Blanpied, G. H. Daw, and A. J. Viescas*
New Mexico State University, Las Cruces, New Mexico 88003

C. L. Morris and H. A. Thiessen
Los Alamos Scientific Laboratory, Los Alamos, New Mexico 87545

S. J. Greene, W. J. Braithwaite, W. B. Cottingame, D. B. Holtkamp, I. B. Moore, and C. F. Moore
University of Texas, Austin, Texas 78712

(Received 19 February 1980)

The pion double-charge exchange reaction (π^+,π^-) has been used to measure the ground-state masses of ^{12}O, ^{16}Ne, ^{24}Si, and ^{32}Ar. The mass excesses were found to be 32.059(48), 24.051(45), 10.682(52), and −2.181(50) MeV, respectively. These are the first reported measurements of the masses of ^{24}Si and ^{32}Ar and the values for ^{12}O and ^{16}Ne are improved over previous results. Good agreement with the isobaric multiplet mass equation $M = a + bT_z + cT_z^2$ is obtained for the known members of all four quintets.

[NUCLEAR REACTIONS Pion double-charge exchange, $^9Be(\pi^+,\pi^-)^9C$, $^{12}C(\pi^+,\pi^-)^{12}O$, $^{13}C(\pi^+,\pi^-)^{13}O$, $^{16}O(\pi^+,\pi^-)^{16}Ne$, $^{24}Mg(\pi^+,\pi^-)^{24}Si$, $^{32}S(\pi^+,\pi^-)^{32}Ar$, $E = 180$ MeV, measured Q and $d\sigma/d\Omega$ (5°).]

To first order the masses of isobaric multiplets of nuclear states can be described by the isobaric multiplet mass equation (IMME)[1]:

$$M(A,T,T_z) = a(A,T) + b(A,T)T_z + c(A,T)T_z^2 \ . \tag{1}$$

This form results from assuming only two-body charge-dependent forces. The coefficients of M are related to the diagonal reduced matrix elements of the charge-dependent part of the nuclear Hamiltonian. Deviations from this simple quadratic form are expected if there are significant three-body charge-dependent forces involved in the Hamiltonian.[2] Second-order effects such as isospin mixing of the lower T_z members of the multiplet may also result in higher-order terms in the IMME. These additional terms, $dT_z^3 + eT_z^4$, are related to the off-diagonal matrix elements. Accurate measurements of the masses of $T = \frac{3}{2}$ quartets have shown that the quadratic form of the IMME works very well for 21 of 22 complete quartets, the only exception being the ground-state $A = 9$ quartet.[3]

For $T = 2$ quintets, only two[4-6] ($A = 8, 20$) have had all members measured with sufficient accuracy to test the IMME. For $A = 8$, significant terms of $dT_z^3 + eT_z^4$ are required to fit the data. These terms probably arise from shifts in the energy levels of two quintet members due to isospin-allowed particle-decay widths. Measured values for the $A = 20$ quintet, which is bound to isospin-allowed particle decay, show agreement with the quadratic IMME. The present measurements of the ground-state masses of ^{24}Si and ^{32}Ar complete the $A = 24$, 32 quintets allowing further tests of the IMME for cases of no isospin-allowed particle decay channels open.

The pion double-charge exchange reaction (π^+,π^-) recently studied by Seth[7] using the EPICS spectrometer facility at LAMPF,[8] provides an excellent method for measuring the masses of $T_z = -2$ nuclei. The spectrometer uses a set of multiwire proportional drift chambers at a focus before the dipole magnets to allow software momentum matching of the spectrometer to the momentum-dispersed beam. We have modified the EPICS system by placing an additional dipole bending magnet after the pion scattering target on the rotating arm of the spectrometer and before the spectrometer entrance (Fig. 1). This allowed a twenty degree separation angle between the outgoing π^+ beam and the scattered π^- beam from 0° double charge exchange (DCX), which led to a considerable count rate reduction in the chambers ($F_1 - F_4$) and enabled the first systematic measurements of angular distributions for DCX at forward angles.

Energy excitation functions of $d\sigma/d\Omega$ (5°) and

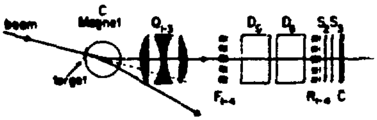

FIG. 1. Schematic view of the EPICS system as modified for DCX.

TABLE I. Targets, target thicknesses, and differential cross sections for (π^+,π^-) at 180 MeV and 5° lab angle.

	Thickness (mg/cm^2)	Cross section (μb/sr)	Chemical composition	Isotope purity (%)	Q value (MeV)
^{9}Be	204	0.15 ± 0.0[illegible]	Be	100	−17.564 ± 0.042
^{12}C	227	0.40 ± 0.0[illegible]	C	99	−32.066 ± 0.048
^{13}C	366	0.10 ± 0.0[illegible]	C	90	−19.966 ± 0.060
^{16}O	187	0.34 ± 0.04	MgO	100	−28.786 ± 0.045
^{24}Mg	235	0.11 ± 0.0[illegible]	MgO	100	−24.810 ± 0.062
^{32}S	250	0.064 ± 0.025	S	95	−23.837 ± 0.060

TABLE II. Properties of $T=2$ levels of isospin quintets in this study.

A	J^π	T_z	Nucleus	E_x (keV)	Mass excess (keV)	Ref.
12	0$^+$	2	^{12}Be	g.s.	25 076(15)	11
		1	^{12}B	12 710(20)	26 000(20)	12
		0	^{12}C	27 595.0(24)	27 595.0(24)	13
		−1	^{12}N	unknown	unknown	
		−2	^{12}O	g.s.	32 050(40)	this
16	0$^+$	2	^{16}C	g.s.	13 694(7)	10
		1	^{16}N	9 928(7)	15 610(7)	14
		0	^{16}O	22 721(3)	17 984(3)	14
		−1	^{16}F	unknown	unknown	
		−2	^{16}Ne	g.s.	24 051(45)	this
24	0$^+$	2	^{24}Ne	g.s.	−5 948(10)	10
		1	^{24}Na	5 969.8(18)	−2 448.5(18)	15
		0	^{24}Mg	15 436.4(6)	1 505.8(6)	15
		−1	^{24}Al	5 596(10)	5 903(8)	16
		−2	^{24}Si	g.s.	10 682(52)	this
32	0$^+$	2	^{32}Si	g.s.	−24 092(7)	15
		1	^{32}P	5 073.1(8)	−19 231.6(12)	15
		0	^{32}S	12 050(4)	−13 965(5)	15
		−1	^{32}Cl	5 033(10)	−8 295.6(52)	17
		−2	^{32}Ar	g.s.	−2 181(50)	this

TABLE III. Coefficients of the IMME and reduced χ^2 from least-squares fit.

A	a (MeV)	b (MeV)	c (MeV)	d (MeV)	e (MeV)	χ^2
12	27.5940([illegible]	−1.7478(118)	0.2441(82)			0.367
	27.5950(24)	−1.7626(273)	0.2434(83)	0.0044(72)		
16	17.9836(29)	−2.5949(89)	0.2233(57)			0.462
	17.9840(30)	−2.5896(112)	0.2226(60)	0.0008(37)		
24	1.5057(9)	−4.1757(36)	0.2222(31)			1.150
	1.5050(9)	−4.1767(37)	0.2194(38)	0.0020(21)		0.003
	1.5058(9)	−4.1818(75)	0.2235(66)	0.0000(47)	−0.0021(27)	
32	−13.9657(25)	−5.4006(25)	0.2027(33)			0.207
	−13.9663(37)	−5.4002(31)	0.2034(41)	−0.0006(22)		0.571
	−13.9651(40)	−5.4040(55)	0.1994(66)	−0.0003(43)	0.0019(36)	

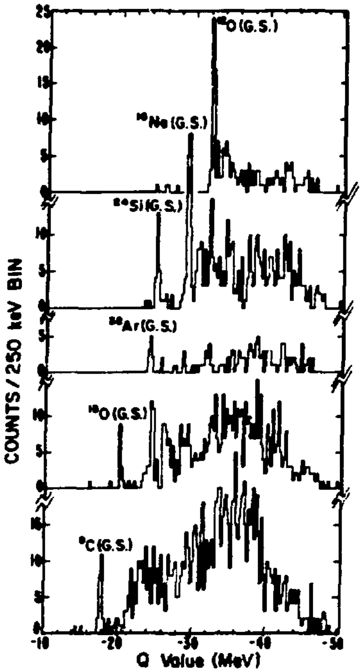

FIG. 2. Q-value spectra from targets of ^{9}Be, ^{12}C, ^{32}S, ^{24}MgO, and ^{12}C, for DCX leading to the final states as labeled.

angular distributions for the nonanalog, analog transitions ^{16,18}O$(\pi^+,\pi^-)^{16,18}$Ne and ^{24,26}Mg$(\pi^+,\pi^-)^{24,26}$Si have been measured.[9] For the nonanalog transitions the largest count rates (a product of pion flux, cross section, and survival fraction) were seen at 180 MeV and 5°, the most forward angle measured. By measuring missing masses (Q values) for the DCX reaction (π^+,π^-), at this energy and angle, on targets of ^{12}C, ^{24}MgO, and ^{32}S to the ground states of ^{12}O, ^{16}Ne, ^{24}Si, and ^{32}Ar, we have determined the mass excesses of these residual nuclei relative to those of the target nuclei.

The linearity of the missing mass calculations was determined by using pion scattering to the ground state, 4.439 and 7.654 MeV states of ^{12}C. Two settings of the spectrometer were used in order to cover the entire focal plane region used in the mass measurements. The missing mass calculation (the spectra obtained are shown in Fig. 2) was linear to 10 keV over the focal plane region used in these measurements. Absolute calibration was done by measuring the ground-state masses of ^{9}C and ^{12}O,[10] using ^{9}Be and ^{12}C targets. The systematic error introduced because of uncertainties in the calibration was ±10 keV. Since the magnets were not changed for any of the mass measurements, there were no systematic errors introduced due to magnet setting reproducibility.

Target thickness corrections to measured Q values were made by using measurements of the energy loss in each target for pion elastic and inelastic scattering at 35°, again using the same magnet settings for all targets. Relative energy losses between the targets were determined to better than ±10 keV for all targets. Both the channel and spectrometer magnetic fields were monitored periodically throughout the run. Fluctuations in the spectrometer fields contributed the largest systematic errors of ±30 keV.

The targets used were 10×20 cm with thicknesses from 157 to 356 mg/cm^2. These thicknesses with the intrinsic spectrometer resolution of ~200 keV combined for an overall resolution of ~300 keV (full width at half maximum). With 10 to 30 counts in the ground-state peaks the statistical errors obtained for all the Q values were less than 40 keV (σ). Although not important to the mass measurements the differential cross sections for these reactions are presented in Table I because of their general interest.

The resulting mass excesses and errors, including all systematic contributions discussed in the text for ^{12}O, ^{16}Ne, ^{24}Si, and ^{32}Ar, are 32 059(48) 24 051(45), 10 682(52), and −2181 (50 keV, respectively. The values of ^{12}O and ^{16}Ne may be compared with those of Kekelis et al.[11] of 32 100(120) and 23 920(80) keV, respectively. Our results plus those for the other known quintet members are summarized in Table II.

These masses were used to determine the coefficients of the IMME. The values were fitted to all orders in T_z with a least-squares program and the fitted coefficients are listed in Table III. The reduced χ^2 values show that there is no evidence for higher-order terms; i.e., when such terms are extracted they are consistent with zero. This constitutes further evidence for a nuclear force which gives a quadratic IMME.

The authors gratefully acknowledge the excellent technical support of the LAMPF MP-10 staff and, in particular, Noby Tanaka. This work was supported by the Medium Energy Division of the U.S.D.O.E. and the Robert A. Welch Foundation.

---

[*] Present address: Stanford University, Stanford, California 94305.

[1] E. P. Wigner, in *Proceedings of the Robert A. Welch Foundation Conference on Chemical Research, Houston, Texas*, edited by W. O. Milligan (Robert A. Welch Foundation, Houston, Texas, 1957), p. 67.

[2] D. H. Wilkinson, *Isobaric Spin in Nuclear Physics*, edited by J. D. Fox and D. Robson (Academic, New York, 1966).

[3] W. Benenson and E. Kashy, Rev. Mod. Phys. 51, 527 (1979).

[4] R. E. Tribble, R. A. Kenefick, and R. L. Spross, Phys. Rev. C 13, 50 (1976).

[5] R. G. H. Robertson, W. Benenson, E. Kashy, and D. Mueller, Phys. Rev. C 13, 1018 (1976).

[6] D. Moltz *et al.*, Phys. Rev. Lett. 42, 43 (1979).

[7] K. K. Seth *et al.*, Phys. Rev. Lett. 43, 1574 (1979); 41, 1589 (1978).

[8] H. A. Thiessen *et al.*, Los Alamos Scientific Laboratory Report No. LA-4534-MS (unpublished).

[9] S. J. Greene *et al.*, Phys. Lett. 88B, 62 (1979).

[10] A. H. Wapstra and K. Bos, At. Data Nucl. Data Tables 19, 175 (1977).

[11] D. Alburger *et al.*, Phys. Rev. C 18, 2727 (1978).

[12] F. Ajzenberg-Selove, Nucl. Phys. A248, 1 (1975).

[13] R. G. H. Robertson *et al.*, Phys. Rev. C 17, 1535 (1978).

[14] F. Ajzenberg-Selove, Nucl. Phys. A281, 1 (1977).

[15] P. M. Endt and C. van der Leun, Nucl. Phys. A310, 1 (1978).

[16] J. Äystö *et al.*, Phys. Lett. 82B, 43 (1979).

[17] E. Hagberg *et al.*, Phys. Rev. Lett. 39, 792 (1977).

[18] G. J. Kekelis *et al.*, Phys. Rev. C 17, 1929 (1978).

APPENDIX IV

Interference Effects in Pion Double Charge Exchange

(submitted to Physical Review C)

Interference Effects in Pion Double Charge Exchange

S. J. Greene,[a] D. B. Holtkamp,[b]
W. B. Cottingame,[a] and C. Fred Moore
University of Texas at Austin, Austin, TX 78712

G. R. Burleson
New Mexico State University, Las Cruces, NM 88003

C. L. Morris and H. A. Thiessen
Los Alamos National Laboratory, Los Alamos, NM 87545

H. T. Fortune[c]
Los Alamos National Laboratory, Los Alamos, NM 87545
and
University of Pennsylvania, Philadelphia, PA 19104

ABSTRACT

Pion double charge exchange (π^+,π^-) has been measured using targets of ^{16}O and ^{18}O from 80 to 292 MeV at a laboratory angle of 5°. The cross section for the double-analog transition is explained in terms of a direct double-analog amplitude and a two-step non-analog amplitude.

PACS numbers: 21.10.Hw, 25.80.+

[NUCLEAR REACTIONS: $^{16}O(\pi^+,\pi^-)^{16}Ne(gs)$ and $^{18}O(\pi^+,\pi^-)^{18}Ne(gs)$; $\theta = 5^{\circ}$, $E_{\pi} = 80$ to 292 MeV, deduced two amplitude explanation for cross-section variation]

Perhaps the most perplexing result to emerge from double-charge-exchange (DCX) measurements with the (π^+,π^-) reaction is the observation[1,2] near the (3,3) pion-nucleon resonance that cross sections for the T = 0 targets (^{16}O and ^{24}Mg) are almost as large as those for T = 1 targets (^{18}O and ^{26}Mg). Of course, only the latter can proceed by the usual DCX mechanism[3,4] connecting the double isobaric analog state (DIAS) to the ground state (i. e., parent state) in the target. It would thus appear that some additional process is contributing to DCX and that it is not negligible compared with the DIAS transition.

An additional puzzling feature of the data is the structure in the excitation function[5] for $^{18}O(\pi^+,\pi^-)^{18}Ne(gs)$, which has been measured for pion kinetic energies from 80 to 292 MeV. At a laboratory angle of 5°, this cross section possesses a peak near 130 MeV, a dip near 170 MeV, and then a slow monotonic increase above that energy. This contrasts with calculations[4,6,7] for the DIAS transition alone, which predict a monotonic increase over the (3,3) resonance and beyond.

We report here on a measurement of an excitation function for $^{16}O(\pi^+,\pi^-)^{16}Ne(gs)$ and a very simple model that appears to account for the data. The $^{18}O(\pi^+,\pi^-)^{18}Ne(gs)$ data have been published previously.[5]

Data were collected on the Energetic Pion Channel and Spectrometer (EPICS) facility. A system for investigating DCX reactions, from 5° to 35° in the laboratory, has been incorporated[5] into the EPICS system. A circular bending magnet (in the horizontal plane) was positioned after the pion scattering target. This allowed the charge-exchanged pions of one polarity to be separated from the outgoing beam of the opposite polarity. Eliminating the unwanted pions significantly reduced the counting rate of the spectrometer entrance drift chambers. Targets chosen for the study were the isotopic pair ^{16}O and ^{18}O in the form of isotopically enriched ice of ≈ 1.0 gm/cm^2 thick. The $^{16,18}O$ pair was chosen because of the many calculations performed for DCX on ^{18}O. Further experimental details are contained in Ref. 8.

The experimental excitation functions for $^{16,18}O(\pi^+,\pi^-)^{16,18}Ne(gs)$ are displayed in Fig. 1, along with the calculation of Miller and Spencer[7] for the $^{18}O(\pi^+,\pi^-)^{18}Ne(gs)$ DIAS transition. A number of observations are in order:

1) The calculated curve appears to agree with the ^{18}O data, in both shape and magnitude, at the higher energies.
2) The ^{16}O cross section is small at those higher energies.
3) The ^{16}O cross section has a resonance-like structure with a peak near 160 MeV.
4) The peak in the ^{16}O data roughly coincides with the dip in the ^{18}O data.

We believe the $^{18}O(\pi^+,\pi^-)^{18}Ne(gs)$ amplitude is a sum of two terms: One is the usual double-isobaric-analog-transition (DIAT) amplitude, which leaves unchanged all quantum numbers (except t_z) of all nucleons, and has been referred to in the literature as a quasi-elastic amplitude[9]; the other, which we call non-DIAT, is the sum of all processes that can (without violating the Pauli principle) change any two neutrons into any two protons, e. g. $\nu(1d_{5/2})^2_{0^+} \rightarrow \pi(2s_{1/2})^2_{0^+}$, or $\nu(1p_{1/2})^2_{0^+} \rightarrow \pi(1d_{5/2})^2_{0^+}$, etc. For the present, we need only the forward-angle amplitudes as a function of energy. Let B(E) represent DIAT and A(E) non-DIAT. Then for B(E) we can use the calculation of Miller and Spencer.[7] We propose to take A(E) from experiment for $^{16}O(\pi^+,\pi^-)^{16}Ne(gs)$. Because the pertinent non-DIAT routes for ^{16}O and ^{18}O are so similar, A(E) for $^{18}O(\pi^+,\pi^-)^{18}Ne(gs)$ is approximately equal to A(E) for $^{16}O(\pi^+,\pi^-)^{16}Ne(gs)$. Rough estimates give a ratio between 0.7 and 1.5, with reasonable assumptions about the relevant wave functions. In the simple model presented herein, we merely use a ratio of unity. If a specific model for non-DIAT ever becomes available, more detailed calculations can then be done. For the present we have

$$\sigma_{^{16}O}(E) = |A(E)|^2$$

and

$$\sigma_{^{18}O}(E) = |A(E) + B(E)|^2 ,$$

where $|B(E)|^2$ is the Miller-Spencer calculation.[7]

The amplitudes A, B are complex:

$$A = a\, e^{i\phi_a} \quad \text{and} \quad B = b\, e^{i\phi_b} ,$$

so that

$$\sigma(^{16}O) = a^2$$

and

$$\sigma(^{18}O) = |a\ e^{i\phi_a} + b\ e^{i\phi_b}|^2$$

$$= a^2 + b^2 + 2\ a\ b \cos|\phi_a - \phi_b| ,$$

where b^2 is the Miller-Spencer[7] cross section. We have obtained a rough fit to the data with only one parameter, $|\phi_a - \phi_b|$, which, however, is energy dependent. The solid curve in Fig. 1 is the result, and the phase differences are listed in Table I. In general, the interference of the two amplitudes is constructive below the peak in the $^{16}O(\pi^+,\pi^-)^{16}Ne(gs)$ data and destructive above that energy. However, for all points above the peak, the phase difference is only slightly larger than 90°, whereas below the peak the phase difference drops smoothly towards zero as the energy decreases. As simple as the present model is, it gives a good account of the data throughout the energy range.

Another puzzling feature of the $^{18}O(\pi^+,\pi^-)^{18}Ne(gs)$ DCX data[5] is that at 164 MeV, the $^{18}Ne(gs)$ angular distribution has a minimum at a much smaller angle than would be expected from a diffractive model, whereas at 292 MeV, the minimum is at the correct angle. Within the present model, this effect is easily explained. At the higher energies, the non-DIAT amplitude makes a negligible contribution, but near 160 MeV it interferes strongly. Thus, even if the two angular distributions represented by A and B both have minima near the diffractive position, it is still possible for the strong interference to put the $^{18}O(\pi^+,\pi^-)^{18}Ne(gs)$ minimum at a very different angle. Of course, a variety of interference effects can shift the angular-distribution minimum at 164 MeV. We offer a specific choice for the interfering amplitude: it is roughly the same amplitude as that giving rise to the $^{16}O(\pi^+,\pi^-)^{16}Ne(gs)$ cross section. The smallness of the latter at 292 MeV leaves the position of the $^{18}Ne(\pi^+,\pi^-)^{18}Ne(gs)$ minimum unchanged at that energy. It would be instructive to measure the ground-state angular distribution for $^{16}O(\pi^+,\pi^-)^{16}Ne(gs)$, for which we expect a diffractive minimum. Knowledge of that data should help immensely in calibrating the nature of the non-DIAT contribution to DCX.

This work was supported in part by the United States Department of Energy, the Robert A. Welch Foundation, and the National Science Foundation.

REFERENCES

[a] present address: New Mexico State University, Las Cruces, NM 88003

[b] present address: University of Minnesota, Minneapolis, MN 55455

[c] permanent address: University of Pennsylvania, Philadelphis, PA 19104

[1] R. J. Holt, B. Zeidman, D. J. Malbrough, T. Marks, B. M. Preedom, M. P. Baker, R. L. Burman, M. D. Cooper, R. H. Heffner, D. M. Lee, R. P. Redwine, and J. E. Spencer, Phys. Letters 69B, 55 (1977); R. L. Burman, M. P. Baker, M. D. Cooper, R. H. Heffner, D. M. Lee, R. P. Redwine, J. E. Spencer, T. Marks, D. J. Malbrough, B. M. Preedom, R. J. Holt, and B. Zeidman, Phys. Rev. C 17, 1774 (1978).

[2] Martin D. Cooper, in Common Problems in Low- and Medium-Energy Nuclear Physics, Ed. by B. Castel, B. Goulard, and F. C. Khanna (Plenum Publishing Corporation, New York, 1979), 667.

[3] R. G. Parsons, J. S. Trefil, and S. D. Drell, Phvs. Rev. 138, B347 (1965); S. Barshay and G. E. Brown, Phys. Letters 16, 165 (1965).

[4] William J. Gerace, M. M. Sternheim, K.-B. Yoo, and David A. Sparrow, Phys. Rev. C 22, 2497 (1980).

[5] S. J. Greene, W. J. Braithwaite, D. B. Holtkamp, W. B. Cottingame, C. Fred Moore, C. L. Morris, H. A. Thiessen, G. R. Burleson, and G. S. Blanpied, Phys. Letters 88B, 62 (1979).

[6] L. C. Liu and V. Franco, Phys. Rev. C 11, 760 (1975).

[7] G. A. Miller, Bull. Am. Phys. Soc. 25, 731 (1980).

[8] S. J. Greene, W. J. Braithwaite, D. B. Holtkamp, W. B. Cottingame, C. Fred Moore, G. R. Burleson, G. S. Blanpied, A. J. Viescas, G. H. Daw, C. L. Morris, and H. A. Thiessen, "(π^+,π^-) Double-Charge-Exchange Reactions on ^{16,18}O and ^{24,26}Mg," in preparation.

[9] J. D. Anderson, C. Wong, and J. W. McClure, Phys. Rev. 129, 2718 (1963); D. Robson, Annual Review of Nuclear Science, Ed. E. Segre, Annual Reviews, Inc., Palo Alto, CA, 119 (1966).

Table I. Results of phase differences from present fit.

Kinetic Energy (MeV)	$\lvert \phi_a - \phi_b \rvert$ (degrees)
101	20
141	40
182	95
211	99
231	100
292	105

FIGURE CAPTION

Fig. 1. Experimental points for $^{18}O(\pi^+,\pi^-)^{18}Ne(gs)$ [closed circles] and $^{16}O(\pi^+,\pi^-)^{16}Ne(gs)$ [open circles], measured at a laboratory angle of 5°, as a function of π^+ laboratory kinetic energy. Dot-dash curve is a calculation for the ^{18}O DIAS transition from Ref. 7. Solid curve is obtained from this curve and smooth dashed curve through the $^{16}O(\pi^+,\pi^-)^{16}Ne(gs)$ data as outlined in the text.

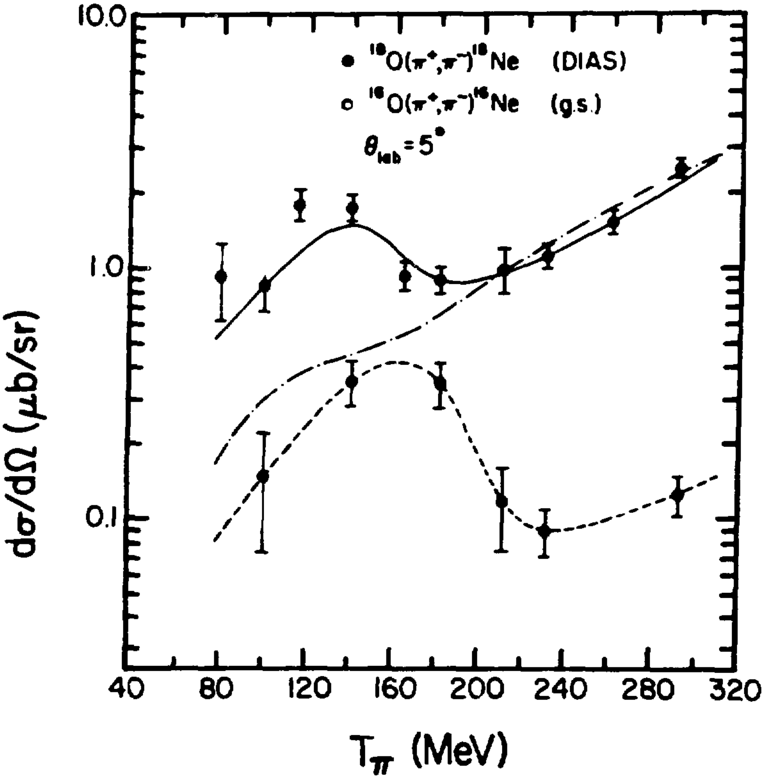
10.0
1.0
0.1
dσ/dΩ (μb/sr)
● ¹⁸O(π⁺,π⁻)¹⁸Ne (DIAS)
○ ¹⁶O(π⁺,π⁻)¹⁶Ne (g.s.)
θlab = 5°
40
80
120
160
200
240
280
320
Tπ (MeV)

APPENDIX V

Observation of a Double Isobaric Analog State in the Reaction $^{209}\mathrm{Bi}(\pi^+,\pi^-)^{209}\mathrm{At}$

Volume 45, Number 15 PHYSICAL REVIEW LETTERS 13 October 1980

Observation of a Double Isobaric Analog State in the Reaction $^{209}Bi(\pi^+,\pi^-)^{209}At$

C. L. Morris and H. A. Thiessen
Los Alamos Scientific Laboratory, Los Alamos, New Mexico 87545

and

W. J. Braithwaite, W. B. Cottingame, S. J. Greene, D. B. Holtkamp, I. B. Moore, and C. Fred Moore
University of Texas, Austin, Texas 78712

and

G. R. Burleson, G. S. Blanpied, G. H. Daw, and A. J. Viescas
New Mexico State University, Las Cruces, New Mexico 88003

(Received 16 June 1980)

Pion double charge exchange has been used to populate the double isobaric analog state in ^{209}At with use of the neutron-rich target ^{209}Bi. The data were obtained at an energy of 292 MeV and at an angle of 5°, as the double-charge-exchange reaction mechanism has been shown to be dominated by analog transitions under these conditions in previous work on light nuclei. The measured cross section is found to be in good agreement with semiclassical predictions by Johnson.

PACS numbers: 24.30.Eb, 25.80.+f, 27.80.+w

Double isobaric analog states (DIAS), i.e., states with $T = T_z + 2$, are known to exist in light nuclei. Because of their high excitation energies, observing such states requires either a probe which will selectively excite them or some unique signature of the DIAS so that they can be separated from the background of lower-T states. The first observation of DIAS was made by Garvey, Cerny, and Pehl[1] using the reaction (p,t) on targets of ^{26}Mg, ^{54}Fe, and ^{46}Ti. Such a reaction is unsuitable for observing DIAS in the large-A region of the periodic table because the ratio of cross sections for populating $T = T_z + 2$ states to $T = T_z$, in a given nucleus, is approximately $1/T^2$.[2]

The only reported observation of a DIAS in heavy nuclei by Hoffmann *et al.*[3] used the isospin forbidden reaction

$$p + {}^{209}\mathrm{Bi} \to {}^{210}\mathrm{Po(DIAS)} \to {}^{209}\mathrm{Bi(IAS)} + p$$
$$\to {}^{208}\mathrm{Pb(g.s.)} + 2p,$$

where the two deexcitation protons where detected in coincidence to provide a unique signature of the reaction. More recent attempts to reproduce the results of this experiment have failed.[4]

Although the possibility of exciting DIAS with use of pion double charge exchange (DCX) at energies near the (3,3) resonance has been recognized for some time,[5] beams with sufficient pion flux and spectrometer systems with adequate energy resolution to study this reaction have not been available until recently.[6] Initial studies of DCX were quite disappointing with regard to observing DIAS in high-A nuclei since, in the low-A region at energies below the (3,3) resonance, both analog and nonanalog transitions were observed to be equally likely. Also DCX cross sections appeared to drop sharply as a function of A.[6]

More recent results,[7,8] which have extended forward-angle DCX measurements to energies well above the (3,3) resonance on isotopic pairs of targets: ^{16,18}O and ^{24,26}Mg, have led to several important observations: (1) The analog to nonanalog cross-section ratios at 5° increase from a minimum of 3:1 and 1.2:1 at energies near the (3,3) resonance to 20:1 and 70:1 at 292 MeV for the oxygen and magnesium isotopes, respectively; (2) although cross-section angular distributions have nonsimple diffraction shapes at 164 MeV,[9] angular distributions at 292 MeV on both ^{18}O and ^{26}Mg are consistent with simple diffraction shapes with use of appropriate strong-absorption radii; and (3) analog DCX cross sections on both ^{18}O and ^{26}Mg peak at 292 MeV and are about a factor of 3 larger than at energies near the (3,3) resonance. Thus it appears that DCX at energies above the resonance may show the needed analog dominance to study DIAS in heavy nuclei.

Consequently, we have undertaken a study of the reaction $^{209}Bi(\pi^+,\pi^-)^{209}At$(DIAS). The data were obtained at an incident pion energy of 292 MeV (lab) and at 5° (lab), using the EPICS facility at the Clinton P. Anderson Meson Physics Facility.[10] The addition of a dipole magnet at the front

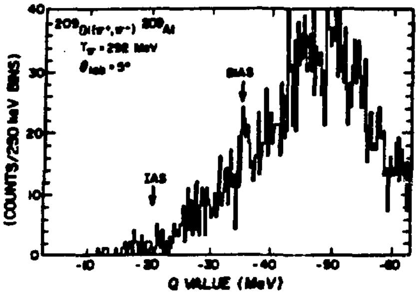

FIG. 1. Double-charge-exchange spectrum on ^{209}Bi. The arrows indicate the expected locations of the isobaric analog state (IAS) and of the double isobaric analog state (DIAS).

of the spectrometer to permit small-angle DCX measurements has been described previously.[7]

The result consists of one DCX Q-value spectrum (Fig. 1). The energy where the DIAS is expected to occur can be calculated by

$$Q = -2E_C + 2(M_n - M_p) = -35.2 \text{ MeV}, \qquad (1)$$

where E_C is the Coulomb displacement energy[11] and $M_n - M_p$ is the neutron-proton mass difference. A peak can be seen to occur near this energy, which is marked by a vertical arrow in the figure. An analysis of this peak, located at 35 ±1 MeV (most of the error in the location comes from systematic errors), indicates it is about standard deviations above the background. The width of the state is about 1 MeV and the cross section to this state is 0.46 ± 0.15 μb/sr.

Assuming analog dominance and using a semiclassical theory, Johnson[12] has derived a simple expression for the A dependence of pion DCX cross sections to DIAS given by

$$d\sigma(\theta = 0°)/d\Omega = \sigma_0 A^{-10/3}(N - Z)(N - Z - 1). \qquad (2)$$

In Fig. 2 we show the present datum along with the two previously reported[7,8] cross sections for DCX to DIAS at 292 MeV and 5°. Fitting the data with the above form gives σ_0 = 20 mb/sr and accounts for the A dependence of these cross sections remarkably well.

In conclusion, we have observed the DIAS of the ground state of ^{209}Bi in ^{209}At using the pion DCX reactions. The Q value for this reaction agrees with predictions based on Coulomb displacement energies measured in earlier studies of IAS. The cross sections for exciting the DIAS in pion DCX are remarkably well described by a single semiclassical theory of such transitions.

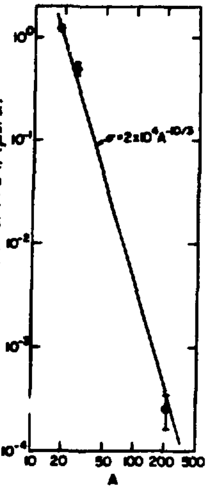

FIG. 2. A dependence of all of the measured 5° cross sections for DCX transitions to DIAS at 292 MeV. The solid curve is a prediction based on the semiclassical approximation of Johnson (Ref. 12) as given in Eq. (2).

This work was supported by the Medium Energy Division of the U. S. Department of Energy and by the Robert A. Welch Foundation.

---

[1] G. T. Garvey, J. Cerny, and R. H. Pehl, Phys. Rev. Lett. 12, 726 (1964).

[2] J. P. Schiffer, in *Isospin in Nuclear Physics*, edited by D. H. Wilkinson (North-Holland, Amsterdam, 1969), p. 667.

[3] G. W. Hoffmann *et al.*, Phys. Rev. Lett. 28, 41 (1972).

[4] W. E. [illegible], private communication.

[5] P. E. Boynton, Phys. Rev. 174, 1083 (1968).

[6] M. D. Cooper, in Proceedings of the LAMPF Workshop on Pion Single Charge Exchange, 1979, edited by H. Baer, D. Bowman, and M. Johnson, LASL Report No. LA-7892, 1979 (unpublished), p. 184; K. K. Seth, *ibid*, p. 201.

[7] S. J. Greene *et al.*, Phys. Lett. 88B, 62 (1979).

[8] G. R. Burleson, in Proceedings of the Workshop on Nuclear Structure with Intermediate Energy Probes, 1980, edited by H. A. Thiessen, LASL Report No. LA-8303-C, 1980 (unpublished); S. J. Greene, *ibid*.

[9] K. K. Seth *et al*., Phys. Rev. Lett. 42, 1574 (1979).

[10] "A Proposal for EPICS," LASL Report No. LA-4534-MS, 1970, edited by H. A. Thiessen (unpublished).

[11] G. M. Crawley *et al*., Phys. Rev. C 2, 1071 (1970).

[12] M. B. Johnson, Phys. Rev. C 22, 192 (1980).

APPENDIX VI

Tabulated (π^+,π^-) Cross Sections

Energy Excitation Functions -- dσ/dΩ at 5°

T_π (MeV)	dσ/dΩ (μb/sr)
$^{18}O(\pi^+,\pi^-)^{18}Ne$ (g.s.,DIAS)	
310	1.992 ± 0.252
292	2.405 ± 0.187
261	1.469 ± 0.160
231	1.079 ± 0.120
211	0.960 ± 0.129
182	0.876 ± 0.102
164	1.011 ± 0.116
141	1.714 ± 0.203
117	1.765 ± 0.256
101	0.839 ± 0.168
81	0.925 ± 0.308
$^{18}O(\pi^+,\pi^-)^{18}Ne$ (2_1^+, 1.89 MeV)	
292	0.342 ± 0.086
261	0.238 ± 0.079
231	0.336 ± 0.069
211	0.316 ± 0.127
182	0.022 ± 0.034
165	0.033 ± 0.049
117	0.197 ± 0.112
101	0.469 ± 0.138
81	0.243 ± 0.365
$^{12}C(\pi^+,\pi^-)^{12}O$ (g.s.)	
180	0.400 ± 0.050
$^{32}S(\pi^+,\pi^-)^{32}P$ (g.s.)	
180	0.084 ± 0.025

T_π (MeV)	dσ/dΩ (μb/sr)
$^{26}Mg(\pi^+,\pi^-)^{26}Si$ (g.s.,DIAS)	
310	0.922 ± 0.192
292	1.000 ± 0.143
260	0.450 ± 0.098
211	0.277 ± 0.060
141	0.338 ± 0.074
120	0.385 ± 0.010
$^{24}Mg(\pi^+,\pi^-)^{24}Si$ (g.s.)	
292	0.014 ± 0.006
250	0.013 ± 0.007
180	0.078 ± 0.018
141	0.290 ± 0.062
$^{16}O(\pi^+,\pi^-)^{16}Ne$ (g.s.)	
292	0.119 ± 0.022
231	0.087 ± 0.018
211	0.113 ± 0.041
182	0.339 ± 0.068
141	0.348 ± 0.070
101	0.146 ± 0.073
$^{9}Be(\pi^+,\pi^-)^{9}C$ (g.s.)	
180	0.150 ± 0.030
$^{13}C(\pi^+,\pi^-)^{13}O$ (g.s.)	
180	0.100 ± 0.030
$^{209}Bi(\pi^+,\pi^-)^{209}At$ (~35 MeV,DIAS)	
292	0.460 ± 0.150

Angular Distributions -- dσ/dΩ at 164 MeV

Θ_{lab} (Deg)	dσ/dΩ (μb/sr)
$^{18}O(\pi^+,\pi^-)^{18}Ne$ (g.s.,DIAS)	
5	1.011 ± 0.116
8	0.720 ± 0.089
13	0.323 ± 0.049
18	0.068 ± 0.014
23	0.046 ± 0.014
28	0.178 ± 0.030
33	0.247 ± 0.049

Θ_{lab} (Deg)	dσ/dΩ (μb/sr)
$^{18}O(\pi^+,\pi^-)^{18}Ne$ (2^+_1, 1.89 MeV)	
5	0.033 ± 0.049
8	0.070 ± 0.035
13	0.083 ± 0.035
18	0.094 ± 0.022
23	0.168 ± 0.028
28	0.158 ± 0.035
33	0.128 ± 0.043

Angular Distributions -- dσ/dΩ at 292 MeV

Θ_{lab} (Deg)	dσ/dΩ (μb/sr)
$^{18}O(\pi^+,\pi^-)^{18}Ne$ (g.s.,DIAS)	
5	2.405 ± 0.187
8	1.952 ± 0.378
13	0.593 ± 0.160
18	0.177 ± 0.089
23	0.064 ± 0.012
28	0.065 ± 0.014
33	0.103 ± 0.018

Θ_{lab} (Deg)	dσ/dΩ (μb/sr)
$^{26}Mg(\pi^+,\pi^-)^{26}Si$ (g.s.,DIAS)	
5	1.000 ± 0.143
8	0.684 ± 0.127
13	0.291 ± 0.065
18	0.056 ± 0.019
23	0.035 ± 0.013
28	0.023 ± 0.015
33	0.100 ± 0.036

Acknowledgments

First and foremost, I wish to thank my advisor, C. Fred Moore, for allowing me (and helping me take advantage of) this opportunity.

Also, the staff of LAMPF have been of tremendous assistance in this work. The MP-10 group has devoted much time and effort (and money) to my assistance, particularly Henry A. Thiessen, Christopher L. Morris, Richard L. Boudrie, James F. Amann, and Nobyuki Tanaka. The technical support and advice of Joseph Kosty, Leroy Atencio, and Kenneth Chellis have benefited me greatly. The MP Division Office has been very kind. Louis Rosen, Division Leader, has always been very supportive of student and young scientist research and learning activities at LAMPF. His staff, the people who are LAMPF, have continually been of the utmost aid in all facets of my research at Los Alamos. The LAMPF Users Group liason staff, Maggie Eustler, Linda Tyra, Judy Powers, and Billie Miller, have always been wonderfully helpful and I deeply appreciate their efforts.

I am especially thankful to Mikkel B. Johnson and Edward R. Siciliano for their many discussions with me, and long hours of thoughtful work, on the meaning, analysis, and implications of pion double-charge-exchange and pion-nuclear physics in general. Also, I thank George R. Burleson for his careful considerations and advice over the course of this research. H. Terry Fortune has brought new insights to this work and helped provide new directions for research in this area; I am indebted to him.

Last, but not least, I wish to thank David Holtkamp, John McGill, Richard Joseph, Ronald Ransome, Martin Barlett, and William Cottingame for their encouragement and support.

Also, I am grateful to Donald Walker and Associated Western Universities for financial assistance during the course of my studies, provided at a time when it was most needed.

REFERENCES

Ag-79 L. Agnew, T. S. Baldwin, D. L. Grisham, R. C. Holmberg, J. E. Lambert, L. O. Lindquist, R. D. Reiswig, and L. L. Thorn, in "Proceedings of the 1979 Particle Accelerator Conference, Accelerator Engineering and Technology," San Francisco, California, USA; also, Los Alamos National Laboratory, Report no. LA-UR-79-688, (1979) unpublished.

Am-79 J. F. Amann, R. L. Boudrie, H. A. Thiessen, C. L. Morris, and L. E. Smith, IEEE Trans. Nucl. Sci., NS-26, 4389 (1979).

An-62 J. D. Anderson, C. Wong, J. W. McClure, Physical Review 126, 2170 (1962).

Ba-66 Yu. A. Batusov, S. A. Bunyatov, V. M. Sidorov, V. A. Yarba, Yadernaya Fizica (Soviet Journal of Nuclear Physics) 3, 223 (1966).

Bo-79 R. L. Boudrie, J. F. Amann, C. L. Morris, H. A. Thiessen, and L. E. Smith, IEEE Trans. Nucl. Sci., NS-26, (1979).

Bo-68 P. E. Boynton, T. J. Devlin, J. Solomon, V. Perez-Mendez, Physical Review 174, 1083 (1968).

Br-65 G. E. Brown and S. Barshay, Physics Letters 16, 165 (1965).

Br-77 K. L. Brown, F. Rothacker, D. C. Carey, and Ch. Iselin, Stanford Linear Accelerator Center, Report No. SLAC-91, Rev. 2, UC-28, (1977) unpublished.

Br-80 W. J. Braithwaite, C. F. Moore, S. J. Greene, C. L. Morris. and W. B. Cottingame, in "Proceedings of the Workshop on Nuclear Structure with Intermediate-Energy Probes," Los Alamos National Laboratory, Report no. LA-8303-C, 457 (1980).

Bu-78 R. L. Burman, M. P. Baker, M. D. Cooper, R. H. Heffner, D. M. Lee, R. P. Redwine, J. E. Spencer, T. Marks, D. J. Malbrough, B. M. Preedom, R. J. Holt, and B. Zeidman, Physical Review C 17, 1774 (1978).

Bu-80 R. L. Burman, (private communication).

Ch-56 G. F. Chew and F. E. Low, Physical Review 101, 1570 (1956).

Co-68 C. J. Cook, M. E. Nordberg, R. L. Burman, Physical Review 174, 1374 (1968).

Co-79 M. D. Cooper, in Common Problems in Low- and Medium-Energy Nuclear Physics, Ed. by B. Castel, B. Goulard, and F. C. Khanna (Plenum Publishing Corporation, N.Y., 1979) 667.

Co-80 W. B. Cottingame and D. B. Holtkamp, Physical Review Letters 45, 1828 (1980).

Da-64 R. Davis et al., Bull. Am. Phys. Soc. 9, 627 (1964).

Do-79 D. Dodder, Los Alamos National Laboratory, (private communication).

Ei-80 J. Eisenberg and D. Koltun, Theory of Meson Interactions with Nuclei, (John Wiley and Sons, New York, 1980).

Er-63 T. E. O. Ericson, in "Proceedings of the 1963 International Conference on High Energy Physics and Nuclear Structure," CERN, CERN Report No. 63-28, (1963).

Eu-69 Euratom Report, EUR-4100e, (1969).

Gi-64 L. Gilly, M. Jean, R. Meunier, M. Spighel, J. P. Stroot, P. Duteil, A. Rode, Physics Letters 11, 244 (1964).

Gi-71 W. R. Gibbs, Physical Review C 3, 1127 (1971).

Gr-79 S. J. Greene, W. J. Braithwaite, D. B. Holtkamp, W. B. Cottingame, C. F. Moore, C. L. Morris, H. A. Thiessen, G. R. Burleson, G. S. Blanpied, Physics Letters 88B, 62 (1979).

Gr-81 S. J. Greene, E. R. Siciliano, and M. B. Johnson, in preparation.

Ho-77 R. J. Holt, B. Zeidman, D. J. Malbrough, T. Marks, B. M. Preedom, M. P. Baker, R. L. Burman, M. D. Cooper, R. H.

Heffner, D. M. Lee, R. P. Redwine, and J. E. Spencer, Physics Letters 69B, 55 (1977).

Jo-78 M. B. Johnson and H. A. Bethe, Comm. Nucl. Part. Phys. 8, 75 (1978).

Jo-79 M. B. Johnson, in "Proceedings of the LAMPF Workshop on Pion Single Charge Exchange," Los Alamos National Laboratory, Report no. LA-7892-C, 342 (1979) unpublished.

Jo-80 M. B. Johnson, Physical Review C 22, 192 (1980).

Jo-81 M. B. Johnson and E. R. Siciliano, in preparation.

Ka-74 W. B. Kaufmann, J. C. Jackson, W. R. Gibbs, Physical Review C 9, 1340 (1974).

Ke-38 N. Kemmer, Proceedings of the Royal Society A166, 127 (1938); also, Proceedings of the Cambridge Philosophical Society 34, 354 (1938).

Ke-59 A. K. Kerman, H. McManus, R. M. Thaler, Annals of Physics (N.Y.) 8, 551 (1959).

Ke-78 G. J. Kekelis, M. S. Zisman, D. K. Scott, R. Jahn, D. J. Vieira, J. Cerny, and F. Ajzenberg-Selove, Physical Review C 17, 1929 (1978).

Ki-55 L. S. Kisslinger, Physical Review 98, 761 (1955).

Ko-65 D. S. Koltun and A. Reitan, Physical Review 139, B1372 (1965).

Ko-69 D. S. Koltun, Advances in Nuclear Physics 3, 71 (1969).

Li-75 L. C. Liu and V. Franco, Physical Review C 11, 760 (1975).

Li-80 S.-H. Liu, C.-E. Wu, C.-H. Hwang, and Y.-G. Li, "π^+-^{16,18}O Double Charge Exchange Reaction," Institute of High Energy Physics, Academia Sinica, Preprint (1980).

Li-81 L. C. Liu, (private communication).

Ma-77 T. Marks, M. P. Baker, R. L. Burman, M. D. Cooper, R. H. Heffner, R. J. Holt, D. M. Lee, D. J. Malbrough, B. M. Preedom, R. P. Redwine, J. E. Spencer, and B. Zeidman, Physical Review Letters 38, 149 (1977).

Mi-74 G. A. Miller and J. E. Spencer, Physics Letters 53B, 329 (1974).

Mi-75 G. A. Miller and J. E. Spencer, Los Alamos Scientific Laboratory, LASL Report No. LA-5948-MS, (1975) unpublished.

Mi-76 G. A. Miller and J. E. Spencer, Annals of Physics (N.Y.) 100, 562 (1976).

Os-78 E. Oset, D. Strottman, G. E. Brown, Physics Letters 73B, 393 (1978).

Pa-65 R. G. Parsons, J. S. Trefil, S. D. Drell, Physical Review 138, B847 (1965).

Pa-79 C. Pacheco, C. Stark, N. Tanaka, D. Hodgkins, J. Barnhart, and J. Kosty, Los Alamos National Laboratory, Report no. LA-8109-MS, (1979) unpublished.

Pe-77 C. Perrin, J.-P. Albanese, R. Corfu, J.-P. Egger, P. Gretillat, C. Lunke, J. Piffaretti, E. Schwarz, J. Jansen, and B. M. Preedom, Physics Letters 69B, 301 (1977).

Ro-78 G. Rowe, M. Salomon, and R. H. Landau, Phys. Rev. C18, 584 (1978).

Ro-80 D. Robson, (private communication).

Se-79 K. K. Seth, in "proceedings of the LAMPF Workshop on Pion Single Charge Exchange," Los Alamos National Laboratory, Report no. LA-7892-C, 201 (1979) unpublished.

Si-70 R. P. Singhal, J. P. Moreira, and H. S. Caplan, Physical Review Letters 24, 73 (1970).

Si-75 B. Sinha, Physics Reports 20, 1 (1975).

Sl-76 D. C. Slater, Los Alamos National Laboratory, unpublished.

Sm-79 L. E. Smith, University of Texas, unpublished.

Sp-77 J. E. Spencer, in "Proceedings of the VIIth International Conference on High Energy Physics and Nuclear Structure, Zurich, 153 (1977).

Th-70 H. A. Thiessen _et al._, "A Proposal for Epics," Los Alamos National Laboratory, Report No: LA-4534-MS, (1971) unpublished.

Th-77 H. A. Thiessen, J. C. Kallne, J. F. Amann, R. J. Peterson, S. J. Greene, S. L. Verbeck, G. R. Burleson, S. G. Iverson, A. W. Obst, K. K. Seth, C. F. Moore, J. E. Bolger, W. J. Braithwaite, D. C. Slater, and C. L. Morris, Los Alamos National Laboratory, Report no. LA-6663-MS, (1977) unpublished.

US-78 _Standard Nuclear Instrumentation Modules_, TID-20893(Rev.4), United States Department of Energy, Washington, D.C. (1978).

Wi-57 E. P. Wigner, in "Proceedings of the Robert A. Welch Foundation Conference on Chemical Research," Houston, Texas, edited by W. O. Milligan (Robert A. Welch Foundation, Houston, Texas, 1957) p67.

Yu-35 H. Yukawa, Proc. Phys. Math. Soc. Japan _17_, 48 (1935).

☆U.S. GOVERNMENT PRINTING OFFICE: 1981-0-777-022/102